# X-ray Study of the Cygnus Loop Supernova Remnant

Hiroyuki Uchida

Department of Earth and Space Science, Graduate School of Science,
Osaka University, Japan

# Abstract

The Cygnus Loop supernova remnant (SNR) is one of the brightest and largest SNRs in X-ray sky. While the previous studies suggest that the Cygnus Loop was created by a core-collapse cavity explosion of a massive star, its origin is still unclear. Between 2002 and 2008, we have observed the Cygnus Loop in X-ray with two observatories, *XMM-Newton* (9 pointings) and *Suzaku* (32 pointings). The spectral analyses clearly distinguished between the two components with different origins; the emission from the swept-up interstellar medium (ISM) which originates from the interaction of the blast wave with an ambient medium and the one from the ejecta which provides a clue to obtaining the information about the progenitor star.

We observed the southwest region of the Cygnus Loop, namely "blowout region" whose origin has remained incompletely understood. The spatial resolved spectral analysis showed that the X-ray spectra obtained from the blowout region consist of two components with different temperatures; the low-temperature ($\sim 0.2\,\mathrm{keV}$) ISM component and the high-temperature ($\sim 0.5\,\mathrm{keV}$) ejecta component. Both of them are the Cygnus Loop origin. We found that the emission from the ISM component is relatively weak and concluded that the X-ray shell is thin in the blowout region, which suggests the origin of the blowout can be explained as a breakout into a lower density cavity wall.

We also found the evidence of such cavity-wall break at the northern limb. The abundances at this region (namely "abundance-enhanced region") are consistent with those of the surrounding ISM whereas the other limb spectra commonly show the lower abundances. From a morphological point of view, we concluded that the blast waves in the abundance-enhanced regions are now proceeding into the outside of the cavity wall and begin to interact with the surrounding ISM.

By using all available data, we also conducted a comprehensive study on the shell structure of the Cygnus Loop. The results indicate that the density of the surrounding cavity wall is lacking in uniformity and that there exists a line-of-sight cavity wall's break at the west of the center in addition to the south blowout. Furthermore, from the standpoint of the X-ray spectral analysis, we support the origin of the Cygnus Loop is a cavity explosion.

The results mentioned above are based on the spectral analysis of the low-temperature component. On the other hand, we confirmed that the high-temperature component originates from the ejecta of the Cygnus Loop. Our analyses show that the ejecta distributions of the heavy elements reflect the elemental distribution, so-called "onion-like structure" inside the presupernova star; Si and Fe concentrate on the center while Mg is distributed outside of the center. We also found that the center of the Si and Fe distributions is

separated from the geometric center by $25'$ toward the south, which may suggest an asymmetric explosion.

We also found the Ar-K line emission from the combined spectrum of all available data, which is the first detection of Ar emission from the Cygnus Loop. We concluded that the observed Ar originates from the ejecta and it is distributed more near the center. By comparing the abundances of the heavy elements including Ar with some theoretical models, we also speculated the progenitor of the Cygnus Loop. The results strongly suggest the Cygnus Loop's origin as a core-collapse SN rather than a Type-Ia SN and that its progenitor mass is less than $20M_{\odot}$, most likely to be $\sim 12M_{\odot}$.

# Contents

# List of Tables

# List of Figures

# Chapter 1

# Introduction

More than 200 supernova remnants (SNRs) have been found in our galaxy (274 SNRs as of 2009) and a few hundreds of extragalactic supernova (SN) events have been reported every year (256 SNe in 2008 alone). While there is a consensus about the basic picture of the mechanism for both the SN explosions and the evolution of the SNRs today, we have some unsolved issues as represented below;

(i) *What are the conditions that make particle acceleration?*
There are many evidences that the electrons are accelerated at the shock waves of young SNRs, whereas some recent observations suggest that the protons are accelerated in some old SNRs. While it is not yet understood what conditions are needed for the particle accelerations, the shock-cloud interaction is important for this problem in connection with the origin of the galactic cosmic-ray.

(ii) *What mechanism causes a supernova explosion?*
Recent theoretical studies suggest that any scenario considering a simple spherically-symmetric simulation does not cause a SN. In contrast, some recent observations show the evidences for the asymmetric SN explosion. It is still unclear what asymmetric effects are needed for the explosion.

In general terms, problems (i) and (ii) are correlated with the shell and the ejecta of the SNRs, respectively. While many theoretical interpretations are proposed for these problems, the only thing that can decide which theoretical models are reasonable is to accumulate the observational evidences.

For the following reasons, the Cygnus Loop, one of the largest and the brightest SNRs in X-ray sky, is an ideal object to study these problems.

(a) The Cygnus Loop is a typical shell-type SNR. Its shell structures indicate various

interactions between the shock waves and the interstellar medium (ISM). The X-ray morphology will provide information about the surrounding environment.

(b) The Cygnus Loop is a middle-aged SNR. Due to its age, the ejecta inside the shell also emits X-ray because it has already been heated by the reverse shocks. The metal abundance pattern of the ejecta will provide a clue to obtaining the information about the type and the condition of the progenitor star.

The properties (a) and (b) are associated with the problems (i) and (ii), respectively. In any case, the X-ray observations are predictably-effective for this SNR.

We employed two X-ray observatories, *XMM-Newton* and *Suzaku* to observe the Cygnus Loop. Their large fields of view are suitable for covering the broad areas of the Cygnus Loop and their good energy resolutions provide information about various emission lines of heavy elements in this SNR. Furthermore, their wide bandpasses will enable us to distinguish between the low-temperature shell component and the high-temperature ejecta component. With these two great observatories, we covered more than half of this fairly-large remnant which enables us to draw a general picture of the plasma structure of the Cygnus Loop for the first time.

In the following chapters, the overviews of the SNe, the SNRs, and the Cygnus Loop are summarized in Chapter 2. The overviews of two observatories are summarized in Chapter 3. After explaining about the observations and data reductions in Chapter 4, the study results about the shell structure and those about the ejecta are shown in Chapter 5 and Chapter 6, respectively. The discussions including the references of the problems mentioned above are presented in Chapter 7. The origin of the Cygnus Loop is also discussed in this chapter. The final conclusions of this study and some future prospects are summarized in Chapter 8.

# Chapter 2

# Review of the Cygnus Loop

## 2.1 Overview of Supernova

Historically, the novae events have been recognized as "gust stars", because they appeared suddenly in the sky (Table 2.1).

Table 2.1: Summary of the historical SNe, and the source of their records (based on Green & Stephenson 2003)

| | | | Historical Records | | | | |
|---|---|---|---|---|---|---|---|
| Year | Duration | SNR name | Chinese | Japanese | Korean | Arabic | European |
| A.D. 1604 | 12 months | Kepler | few | – | many | – | many |
| A.D. 1572 | 18 months | Tycho | few | – | two | – | many |
| A.D. 1181 | 6 months | 3C58 | few | few | – | – | – |
| A.D. 1054 | 21 months | Crab Nebula | many | few | – | one | – |
| A.D. 1006 | 3 years | SN1006 | many | many | – | few | two |
| A.D. 393 | 8 months | RX J1713.7-3946 ? | one | – | – | – | – |
| A.D. 386? | 3 months | G11.2-0.3 ? | one | – | – | – | – |
| A.D. 185 | 8 or 20 months | RCW 86 ? | one | – | – | – | – |

Baade & Zwicky (1934) pointed out that some novae are extremely brighter than other ones and called this kind of novae supernovae (SNe). The SNe are now explained as explosions at the deaths of stars. The remnants formed after the SN explosions are called supernova remnants (SNRs). The SN has a specific light curve whose maximum luminosity is quite high as much as that of its host galaxy. Therefore if a SN event occurs in our galaxy, it may be easily visible to the naked eye, in some cases, even during the daytime. Ancient people have observed and recorded a lot of SN events: besides the pronounced examples shown in Table 2.1, a B.C. 134 guest star (today, it is known as RCW 103) observed by the ancient Chinese in the Han dynasty and by the Greek

Hipparchus (Lundmark 1921), a B.C. 48 guest star (G21.5-0.9) observed by Chinese in the Han dynasty (Seward & Wang 1988), B.C. 523, A. D. 1408, and A.D. 1532 guest stars which are now called CTB 87, Kes 75, and CTB 80, respectively (Seward & Wang 1988).

The frequency of SNe is important because it is intimately related the structure, kinematics, and elemental composition of the interstellar medium (ISM). Furthermore, the SNe rate determines the cosmic-ray flux of galactic origin. Tammann et al. (1994) estimated the galactic SN rate to be $2.5^{+0.8}_{-0.5}$ SNe per century based on the observed extragalactic SNe and the recorded historical SNe in our galaxy. Contrary to the expected SN rate, SN events seem not to be occurred in our galaxy since A.D. 1604. However, this fact may be simply because the visible light from the unrecorded SNe were obscured by the line-of-sight dense ISM. For example, the origin of the Cassiopeia A (Cas A) is considered to be a recent SN (A.D. 1681±19; Krause et al. 2008) which is younger than the Kepler SNR. Another example is G1.9+0.3 whose age is estimated to be $\sim$ 100 yr judging from the expansion rate (Reynolds et al 2008). The light from these young SNe should have been heavily obscured by ISM at the time of explosion.

### 2.1.1 Classification

The SNe have been classified observationally from their optical spectra and light curves. There are two major categories of SNe: Type I SNe show no hydrogen emission in the maximum light spectra, while Type II SNe have the hydrogen Balmer lines. Such difference of the SN spectra was historically clarified by Zwicky, Baade, and Minkowski in the late 1930s, then Minkowski (1941) first introduced the classification of SNe. Each type is now divided into a few subclasses (Table 2.2).

Table 2.2: Classification of SNe

| Supernova | | | | |
|---|---|---|---|---|
| No H Balmer Lines | | | H Balmer Lines | |
| Type I | | | Type II | |
| Si II 635.5 nm | No Si | | Light Curve Shape: | |
| Type Ia | Type Ib/c | | Plateau | Linear |
| | He I 587.6 nm | Weak He | Type II-P | Type II-L |
| | Type Ib | Type Ic | | |

The spectra of the common Type I SNe have a Si II absorption line at 635.5 nm,

while some Type I SNe do not have it and show a neutral He absorption line at 587.6 nm (Wheeler & Levreault 1985; Uomoto & Kirshner 1985). The former and the latter are called Type Ia and Type Ib, respectively. Moreover, it turned out that some Type I SNe have neither Si nor He feature, and such kind of SNe are called Type Ic (Filippenko et al. 1990). Type II SNe are classified into two subclasses according to their shapes of the light curves (Figure 2.1). In many cases, the Type II light curves reach maximum brightness, dim slightly, and then stay at almost the same brightness "plateau" for about 100 days before fading. They are classified as Type II-P (II-Plateau). Other Type II SNe quickly reach maximum brightness and then dim linearly and are classified as Type II-L (II-Linear).

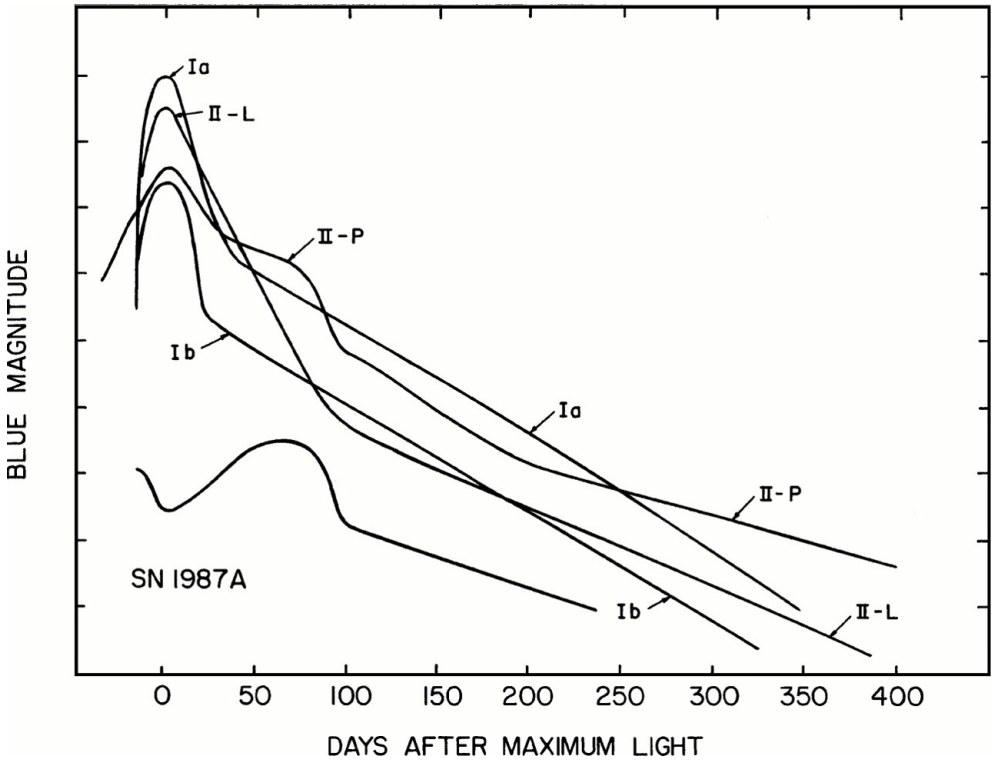


Figure 2.1: Schematic light curves for SNe of Types Ia, Ib, II-L, II-P, and SN 1987A. The curve for SNe Ib includes SNe Ic as well, and represents an average (Filippenko 1997).

### 2.1.2 Explosion Mechanism

The SNe are also classified according to their explosion mechanism. This classification is not necessarily correspond to the foregoing one since the latter is a purely observational one. For example, while Type Ia SNe appear in all types of galaxies, Type Ib/Ic SNe only appear in the galaxies which are in the process of an exceptionally high rate of star

formation. Type II SNe also appear only in the starburst galaxies, which suggests Types Ib/Ic and II have the same origin. According to the consensus picture of the day, there are two different explosion mechanisms as follows. Types Ib/Ic and II belong in the same category. These SNe results by the collapse of a stellar core at the deaths of the massive stars. Thus, they fall into "core-collapse" SNe and are distinguished from the Type Ia SNe.

**Type Ia SN**

The explosion mechanism for Type Ia SN is different from the "core-collapse" of the massive stars. Hoyle & Fowler (1960) first proclaimed the thermonuclear-fusion mechanism for Type Ia SN. As a result, Arnett (1969) proposed a Type Ia model that the stars of intermediate mass ($4M_\odot < M < 9M_\odot$) ignite the $^{12}$C+$^{12}$C reaction explosively and that the star is totally disrupted by the explosive instability due to the detonation of the carbon burning. However, this model could not be suited to the observations such as the absence of hydrogen emission and the Type I rate, for example. It is now considered that such star of low or medium mass becomes a white dwarf after shedding its outer layers.

One alternative mechanism for Type Ia SN is the merger of two C-O white dwarfs (Webbink 1984; Iben & Tutukov 1984). However, a simulation of this model shows that an accretion ignites an off-center carbon flash and that the carbon burning propagates inward through the central region (Saio & Nomoto 1985). As a result, a white dwarf does not explode but changes into an O-Ne-Mg white dwarf. Thus, this model is not considered to be an appropriate model for Type Ia SN.

Another possible mechanism is a mass accretion from a giant star to a C-O white dwarf in their binary system. If a white dwarf gradually accretes mass from a binary giant star, its core is strongly compressed and thus, temperature and pressure become higher. When the mass comes to the Chandrasekhar limit of $\sim 1.38M_\odot$, the core reaches ignition temperature for the carbon fusion,

$$^{12}\mathrm{C} \ + \ ^{12}\mathrm{C} \longrightarrow \begin{cases} ^{20}\mathrm{Ne} \ + \ ^{4}\mathrm{He} \\ ^{23}\mathrm{Na} \ + \ \mathrm{p} \\ ^{24}\mathrm{Mg} \ + \ \gamma \end{cases} \tag{2.1}$$

This reaction causes a thermonuclear runway under high-pressure condition and releases enough energy to collapse a white dwarf.

Two major models are proposed today according to the way of the propagation of carbon burning; detonation wave or deflagration one. The idea of the former model is that the carbon burning produces the shock wave which expands outward at supersonic

speed. However, in theory detonation does not provide enough energy to generate a strong shock wave (Nomoto 1982). Alternative model is called the delayed detonation model, or deflagration detonation transition (DDT) model which assume the shock speed reaches supersonic by transition from deflagration to detonation (Khokhlov 1991). Another model only assumes the deflagration wave for the propagation of the shock wave. In this model, carbon burning propagates by the convective heat transport and its shock speed is about subsonic. Nomoto et al. (1984) calculated the nucleosynthesis in a C+O white dwarf based on the deflagration model and succeeded to explain the observed light curve and the spectrum of Type Ia SN. This model is known as W7 model ("W" means "White dwarf" and "7" is derived from a parameter $\alpha = l/H_p = 0.7$, where $l$ and $H_p$ are a mixing length and a pressure scale height, respectively). In the deflagration model, released nuclear energy ($1.8 \times 10^{51}$ erg) considerably exceeds the gravitational binding energy of the white dwarf ($5 \times 10^{50}$ erg). Therefore the progenitor white dwarf is completely blown off by the explosive energy and no compact object remains after the explosion.

### Core-Collapse SN

Type Ia SN is a death of low-mass ($< 8M_\odot$) star in a binary system. In contrast, the other Types of SNe results by the collapse of a stellar core of the massive star ($> 8M_\odot$) at the end of its evolution. The nucleosynthesis and the evolutionary process of the massive star is summarized as follows.

**Hydrogen burning (CNO cycle)** At the beginning of the stellar evolution, hydrogen nuclei fuse to form $^4$He according to the CNO cycle. This reaction occurs in the main-sequence star whose mass is above the solar mass.

**Helium burning (Triple-alpha process)** When the temperature reaches $\sim 10^8$ K, three $^4$He are transformed into one carbon nucleus (triple-alpha process),

$$\begin{aligned} {}^4\mathrm{He} + {}^4\mathrm{He} &\rightleftharpoons {}^8\mathrm{Be} \\ {}^8\mathrm{Be} + {}^4\mathrm{He} &\rightarrow {}^{12}\mathrm{C} + \gamma \end{aligned} \tag{2.2}$$

Also, some $^{12}$C fuse with additional $^4$He to produce an oxygen,

$${}^{12}\mathrm{C} + {}^4\mathrm{He} \longrightarrow {}^{16}\mathrm{O} + \gamma \tag{2.3}$$

Finally, carbon and oxygen are produced by helium burning.

**Carbon burning** In the next stage, the carbon burning occurs as described in equation 2.1. The ignition temperature for the carbon burning is $\sim 6 \times 10^8$ K and neon, sodium, and magnesium are produced.

**Neon burning** The main nuclear reactions are as follows:

$$\begin{aligned} {}^{20}\mathrm{Ne} + \gamma &\longrightarrow {}^{16}\mathrm{O} + {}^{4}\mathrm{He} \\ {}^{20}\mathrm{Ne} + {}^{4}\mathrm{He} &\longrightarrow {}^{24}\mathrm{Mg} + \gamma \\ {}^{24}\mathrm{Mg} + {}^{4}\mathrm{He} &\longrightarrow {}^{28}\mathrm{Si} + \gamma \end{aligned} \tag{2.4}$$

The ignition temperature is $\sim 1.3 \times 10^9$ K.

**Oxygen burning** The main nuclear reactions are as follows:

$${}^{16}\mathrm{O} + {}^{16}\mathrm{O} \longrightarrow \begin{cases} {}^{28}\mathrm{Si} + {}^{4}\mathrm{He} \\ {}^{31}\mathrm{P} + \mathrm{p} \\ {}^{32}\mathrm{S} + \gamma \end{cases} \tag{2.5}$$

The ignition temperature is $\sim 3 \times 10^9$ K. $^{32}$S, $^{36}$Ar, and $^{40}$Ca are also produced by $^{28}$Si capturing $^{4}$He.

**Silicon burning** The temperature requires more than $4 \times 10^9$ K for the silicon burning. In this process, the iron group elements, such as $^{44}$Ti, $^{48}$Cr, $^{52}$Fe, and $^{56}$Ni are produced from $^{28}$Si with some $^{4}$He. The most part of the products is $^{56}$Ni

**Core-collapse** In the end of the gradual burning processes explained above, $^{56}$Fe are produced at the core of the star. The temperature exceeds $5 \times 10^9$ K. At this stage, a star has a layered structure, so-called "onion structure". Since $^{56}$Fe has one of the lowest binding energy per nucleon (8.8 MeV), any more exothermic reaction does not occur. The star begins to contract and the temperature of the iron core becomes higher. Eventually, following photodegradation reaction occurs at the stellar core:

$$\begin{aligned} {}^{56}\mathrm{Fe} + \gamma &\longrightarrow 13\,{}^{4}\mathrm{He} + 4\mathrm{n} - 124.4\,\mathrm{MeV} \\ {}^{4}\mathrm{He} &\longrightarrow 2\mathrm{p} + 2\mathrm{n} - 28.3\,\mathrm{MeV} \end{aligned} \tag{2.6}$$

Since this is an endothermic reaction, the temperature and the pressure at the stellar core decreases rapidly. The inner core contracts until the density reaches the nuclear matter density of $\sim 2 \times 10^{14}$ g cm$^{-3}$. Then the shock wave produced by released gravitational potential energy bounces the outer material, which is called a "core-collapse" SN. The

difference between the gravitational energy of the inner core before and after the core-collapse is $\sim 3 \times 10^{53}$ erg (assuming the remaining neutron star is 10 km in radius and has $1.4M_{\odot}$). The most part of this energy ($\sim 10^{53}$ erg) is consumed by diffusion of the produced neutrinos and the kinetic energy imparted to the bounce of the outer material is $\sim 5 \times 10^{51}$ erg. As is obvious from the core-collapse mechanism, a neutron star (or a black hole) always remains after the explosion unlike the Type Ia SN.

### 2.1.3 Explosive Nucleosynthesis

In either Type Ia SN or core-collapse SN, the shock wave produced at the center of the star propagates outward and heats the stellar material. In this process, various heavy elements are created by different nucleosyntheses depending on the temperature. The temperature $T$ obeys the following equation,

$$E \sim \frac{4\pi}{3} r^3 a T^4 \tag{2.7}$$

where $E$ and $r$ mean an explosion energy and a radius, respectively. Equation 2.7 shows that the produced elements vary from stratum to stratum in the star. The nucleosyntheses are summarize in Table 2.3 (e.g., Thielemann et al. 1996). The model of the mass fractions after the nucleosynthesis process of $15M_{\odot}$ star is shown in Figure 2.2.

Table 2.3: Explosive nucleosynthesis

| Burning Site | Main Products | Temperature [$10^9$ K] |
|---|---|---|
| C/Ne burning | O, Ne, Mg, Si | $\sim 2.1$ |
| O burning | O, Si, S, Ar, Ca | $\sim 3.3$ |
| Incomplete Si burning | Si, S, Ar, Ca, $^{56}$Ni, Fe, Mn, Cr | $\sim 4$ |
| Complete Si burning | $^{56}$Ni, Ti, $^{64}$Zn, Co | $> 5$ |

In the explosive nucleosynthesis, a large amount of the $^{56}$Ni is created. As a result, $^{56}$Ni undergoes $\beta^+$ decay by means of the following nuclear equation and stable $^{56}$Fe is observed after the explosion

$$^{56}\mathrm{Ni} \xrightarrow[\tau=6.077\mathrm{d}]{} {}^{56}\mathrm{Co} \xrightarrow[\tau=77.23\mathrm{d}]{} {}^{56}\mathrm{Fe\ (stable)} \tag{2.8}$$

where $\tau$ is a half-life of the nuclide.

The mass of the produced $^{56}$Fe is $0.07M_{\odot}$ for the core-collapse SN while Type Ia SN produces about ten times as many $^{56}$Fe as the core-collapse SN (theoretically 0.6-0.8$M_{\odot}$).

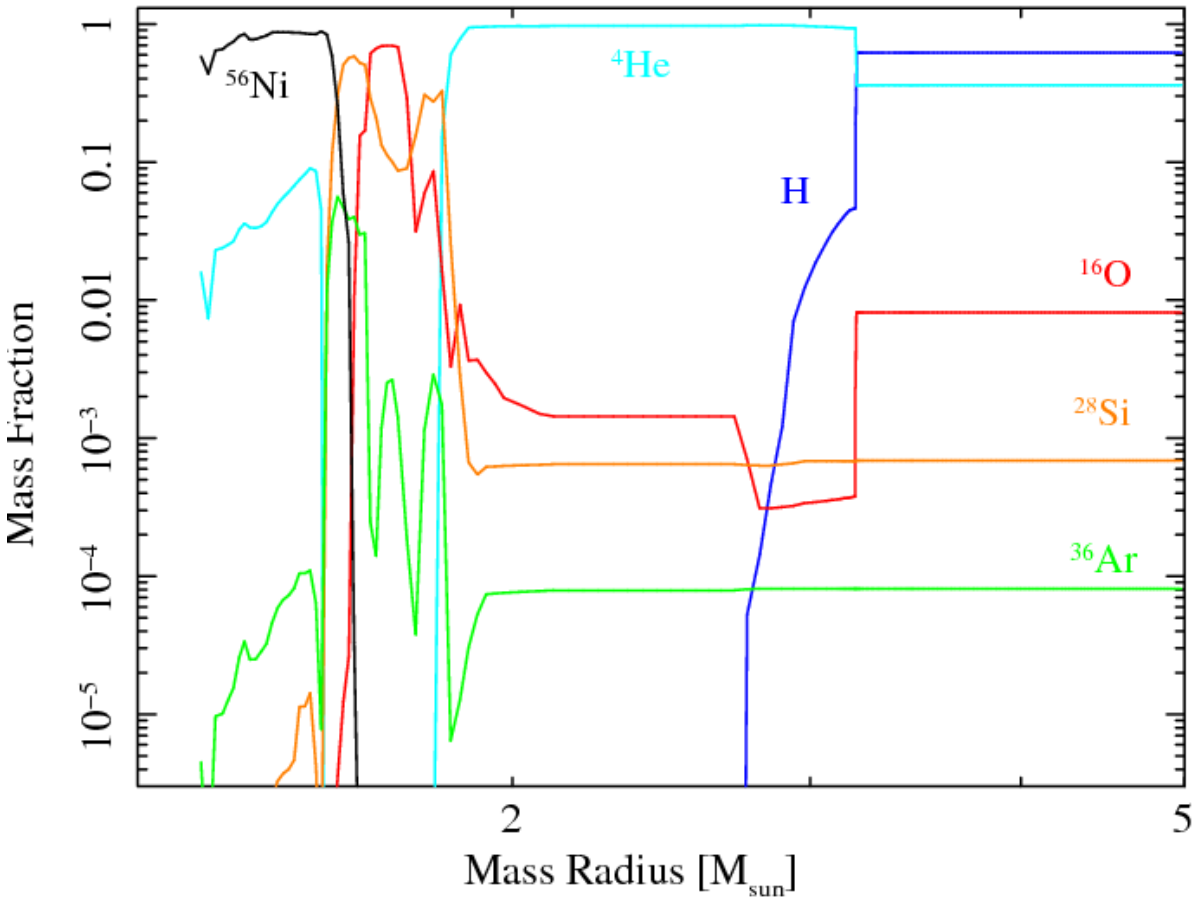


Figure 2.2: Mass fractions of various prominent elements in a $15M_{\odot}$ star (based on the results of Umeda & Nomoto 2005; Nomoto et al. 2006; Tominaga et al. 2007).

This is because the Type Ia explosion completely blows off the Fe-rich stellar core. The amount of the produced $^{56}$Fe makes a crucial difference of the SNRs between observed Type Ia SNe (or SNRs) and core-collapse ones.

## 2.2 Overview of Supernova Remnants

The shock wave formed by SN explosion heats up both the surrounding ISM and the ejecta blown from the progenitor star. In this way, the SNRs which have a variety of morphologies are formed after the SNe and observed at various wavelength. Green (2009) identified and listed 274 SNRs in our galaxy based on the radio observation[1]. Figure 2.3 shows a galactic distribution of all SNRs catalogued by Green (2009). Galactic SNRs are concentrated on the galactic plane. Of the catalogued SNRs, $\sim 40\%$ are detected in X-ray and $\sim 20\%$ are in the optical

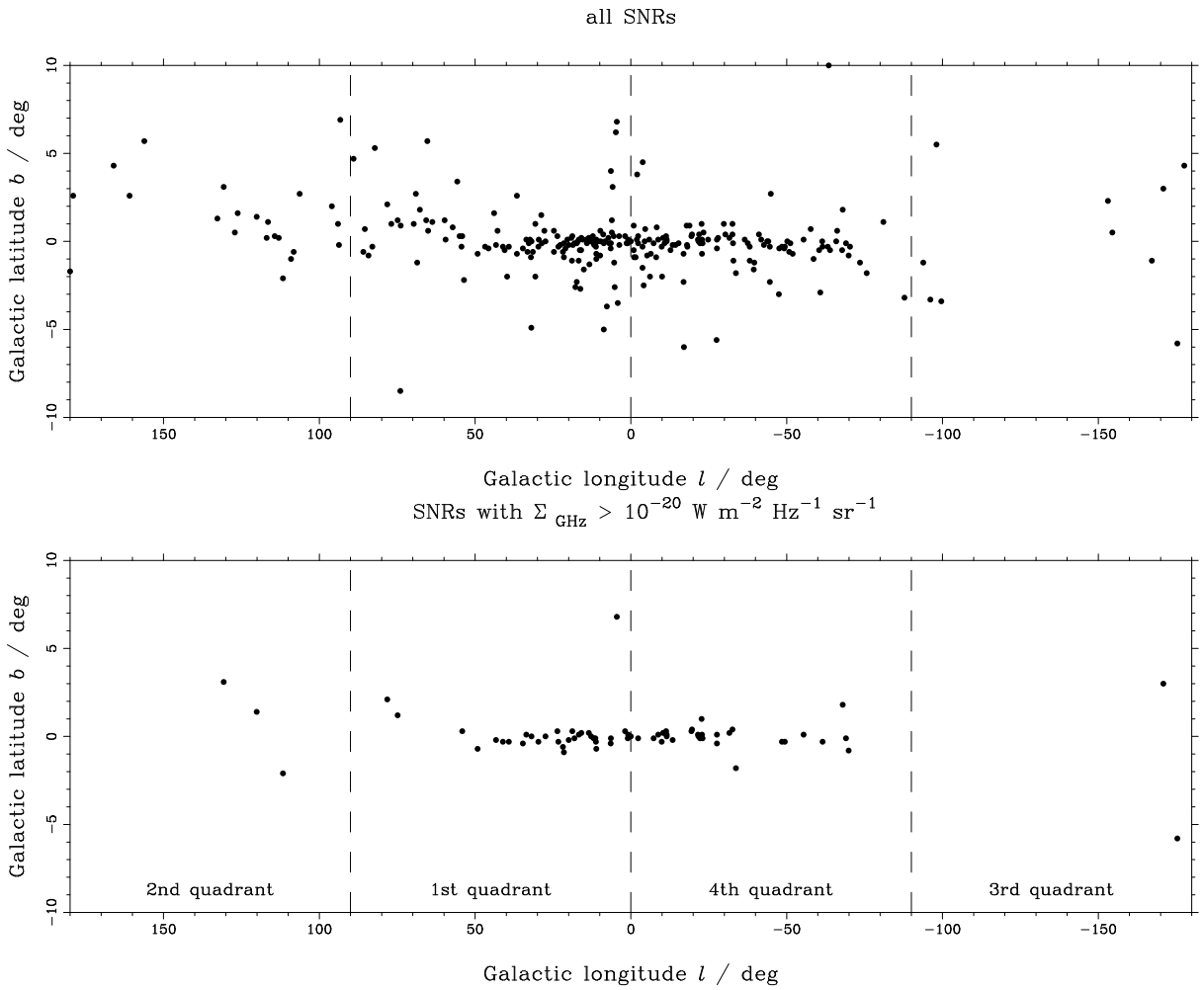


Figure 2.3: Galactic distribution of (top) all Galactic SNR and (bottom) those SNRs with a surface brightness at 1 GHz greater than $10^{-20}\,\mathrm{W\,m^{-2}\,Hz^{-1}\,sr^{-1}}$. Note that the latitude and longitude axes are not on the same scale (Green 2009).

[1]Green's Catalogue: http://www.mrao.cam.ac.uk/surveys/snrs/

### 2.2.1 Basic Physics

An isotropically-expanding SNR is approximately interpreted as a simple point explosion in an uniform ambient density. Under such condition, the behavior of the shock wave is expressed in a few equations:

$$\rho_1 v_1 = \rho_1 v_2 \tag{2.9}$$

$$p_1 + \rho_1 v_1^2 = p_2 + \rho_2 v_2^2 \tag{2.10}$$

$$\frac{1}{2}v_1^2 + w_1 = \frac{1}{2}v_2^2 + w_2 \tag{2.11}$$

where $\rho$, $v$, $p$, and $w$ are the density, velocity, pressure, and enthalpy per mass unit ($w = \gamma p/p(\gamma-1)$, where $\gamma$ means the specific-heat ratio). The subscripts 0 and 1 correspond to the upstream and downstream, respectively. Here the specific volumes (volume per mass unit) are defined as $V_1 = 1/\rho_1$, $V_2 = 1/\rho_2$. These equations represents the conservations of mass flux (2.9), momentum flux (2.10), and energy flux (2.11), respectively. From them, Rankin & Hugoniot relations are obtained below,

$$\frac{\rho_1}{\rho_2} = \frac{v_2}{v_1} = \frac{(\gamma+1)p_1 + (\gamma-1)p_2}{(\gamma-1)p_1 + (\gamma+1)p_2} \tag{2.12}$$

$$\frac{T_1}{T_2} = \frac{p_2}{p_1}\frac{(\gamma+1)p_1 + (\gamma-1)p_2}{(\gamma-1)p_1 + (\gamma+1)p_2} \tag{2.13}$$

where $T_1$ and $T_2$ are the temperatures in upstream and downstream, respectively.

Equations (2.12) and (2.13) are rewritten by using the Mach number, $M_1 = v_1/C_1$ where $C_1 = \gamma p/\rho$ is the sound velocity:

$$\frac{\rho_1}{\rho_2} = \frac{(\gamma+1)M_1^2}{(\gamma-1)M_1^2 + 2} \tag{2.14}$$

$$\frac{T_1}{T_2} = \frac{(2\gamma M_2^2 - (\gamma-1))((\gamma-1)M_2^2 + 2)}{(\gamma+1)^2 M_2^2} \tag{2.15}$$

Assuming the strong shocks (defined by $p_2 \gg p_1$ or $M_1 \ll 1$), they are approximately described as follows:

$$\frac{\rho_1}{\rho_2} \sim \frac{\gamma+1}{\gamma-1} \tag{2.16}$$

$$\frac{T_1}{T_2} \sim \frac{(\gamma+1)p2}{(\gamma-1)p1} \tag{2.17}$$

which derives $\rho_2/\rho_1 \simeq 4$ and $T_1/T_2 \simeq 5/16M_1^2$ in a mono-atomic gas ($\gamma = 5/3$).

The velocities are written as follows:

$$v_1^2 = \frac{\rho_1}{\rho_2}(\gamma+1)p_2 V_1 \tag{2.18}$$

$$v_2^2 = \frac{\rho_1}{\rho_2}\frac{(\gamma-1)^2 p_2 V_1}{\gamma+1} \tag{2.19}$$

$$\tag{2.20}$$

At the same time, from equations 2.9 and 2.11,

$$v_1 - v_2 \;=\; \sqrt{(p_2 - p_1)(V_1 - V_2)} \tag{2.21}$$

Therefore, the pressure behind the shock $p_2$ is expressed by

$$p_2 \;\sim\; \frac{\gamma+1}{2}\rho_1(v_1 - v_2)^2 \qquad (p_2 \gg p_1) \tag{2.22}$$

Assuming that $v_p \equiv v_s - v_2$ is a post-shock velocity and that $v_s \equiv v_1$ is a shock velocity at the rest frame of upstream, $v_p$ and the post-shock pressure $p_p \equiv p_2$ are obtained from equations 2.18, 2.19, and 2.22,

$$v_p \;=\; \frac{2v_s}{\gamma+1} \tag{2.23}$$

$$p_p \;=\; \frac{2\rho_1 v_s^2}{\gamma+1} \tag{2.24}$$

Using the equation of state, the post-shock temperature $T_s$ is obtained as follows:

$$kT_s \;=\; p_p\mu/\rho_2 \;=\; \frac{2(\gamma-1)}{(\gamma+1)^2}\mu m_{\rm H} v_s^2 \tag{2.25}$$

where $k$, $\mu$, and $m_{\rm H}$ are the Boltzmann constant, the mean atomic weight, and the hydrogen mass, respectively. Thus, the post-shock temperature in a mono-atomic gas ($\gamma = 5/3$) are derived

$$kT_s \;=\; \frac{3}{16}\mu m_{\rm H} v_s^2 \tag{2.26}$$

In a solar-metallicity plasma ($n_{\rm He} = 0.1 n_{\rm H}$; e.g., Anders & Grevesse 1989) , the mass density is $\rho = (n_{\rm H} + 4n_{\rm He})m_{\rm H} = 1.4 m_{\rm H} n_{\rm H}$. Meanwhile the total density is $n = (n_{\rm H} + n_{\rm He} + n_{\rm e}) = 2.3 n_{\rm H}$, where $n_{\rm e} = (n_{\rm H} + 2n_{\rm He}) = 1.2 n_{\rm H}$. Hence $\mu = 1.4/2.3 \simeq 0.61$ in a fully ionized plasma.

From equation 2.26, the temperature of the SNR whose shock velocity is $v_s = 1000\,{\rm km\ s^{-1}}$ gives $T_s \simeq 1.2$ keV, for example.

### 2.2.2 Evolution

A SNR formed by a SN expands into the interstellar space and emits its energy for about a few thousand years until its shell slows down and merge into the ISM. The evolution of SNRs is basically classified into four phases as follows: free expansion phase, adiabatic phase, radiative cooling phase and disappearance phase.

**Free Expansion Phase**

The initial phase of the SNR evolution is called free expansion phase. After the SN explosion, the ejected stellar materials expand outward, sweeping up the surrounding ISM. Since the ejected mass is considerably larger than the swept ISM immediately after the SN explosion, the shell formed by expanding ejecta propagates at constant momentum. At this phase, the shock radius $R_0$ and the velocity $v_0$ after the time $t$ from the explosion are indicated by

$$R_s = v_0 t \tag{2.27}$$

$$E_0 = \frac{1}{2} M_0 v_0^2 \tag{2.28}$$

where $E_0$ and $M_0$ are the initial explosion kinetic energy and the total ejected mass, respectively. Assuming $M_0 \simeq 10 M_\odot$ and $E_0 \simeq 10^{51}\,\mathrm{erg}$, the $v_0$ reaches $\sim 10^8\,\mathrm{cm\ s^{-1}}$. Since it is much larger than the sound velocity of the ISM ($\sim 10^6\,\mathrm{cm\ s^{-1}}$), a strong shock wave, namely the blast wave (forward shock) propagates into the ISM. This phase lasts until the mass of the swept-up ISM, $M = 4/3\ \pi R_s^3 n_0$ becomes equal to the ejected mass $M_0$, where $n_0$ is the ISM density. It is estimated to be $t \simeq 1,000\,\mathrm{yr}$ in a typical ISM density of $n_0 \simeq 1\,\mathrm{cm^{-3}}$.

The decelerated blast wave forms another shock wave which propagate toward the center of the SNR. This wave is called a reverse shock which heats up the ejecta inside the shell (McKee 1974). The boundary between the ISM and the ejecta is called a contact discontinuity. The growths of the reverse shock and the contact discontinuity are calculated theoretically as shown in Figure 2.4 (Wang & Chevalier 2002). Their result is based on the one-dimensional hydrodynamic simulation. The parameters in Figure 2.4 is described as follows (they are adapted to the observation of the Vela SNR):

$$t' = \left(\frac{t}{1271\mathrm{yr}}\right)\left(\frac{M_0}{10M_\odot}\right)^{-5/6}\left(\frac{E_0}{10^{51}\mathrm{erg}}\right)^{1/2}\left(\frac{n_0}{1\mathrm{cm^{-3}}}\right)^{1/3} \tag{2.29}$$

$$r' = \left(\frac{r}{4.1\mathrm{pc}}\right)\left(\frac{M_0}{10M_\odot}\right)^{-1/3}\left(\frac{n_0}{1\mathrm{cm^{-3}}}\right)^{1/3} \tag{2.30}$$

The free expansion phase lasts a few hundred years after explosion.

**Adiabatic Phase (Sedov Phase)**

When the blast wave is decelerated by swept-up ISM substantially, the evolution transits to the next phase, namely the adiabatic phase (Sedov phase). At this phase, the blast wave adiabatically expands since the time scale of the expansion is much smaller than the cooling time scale of the heated gas. Therefore, the behavior of the blast wave

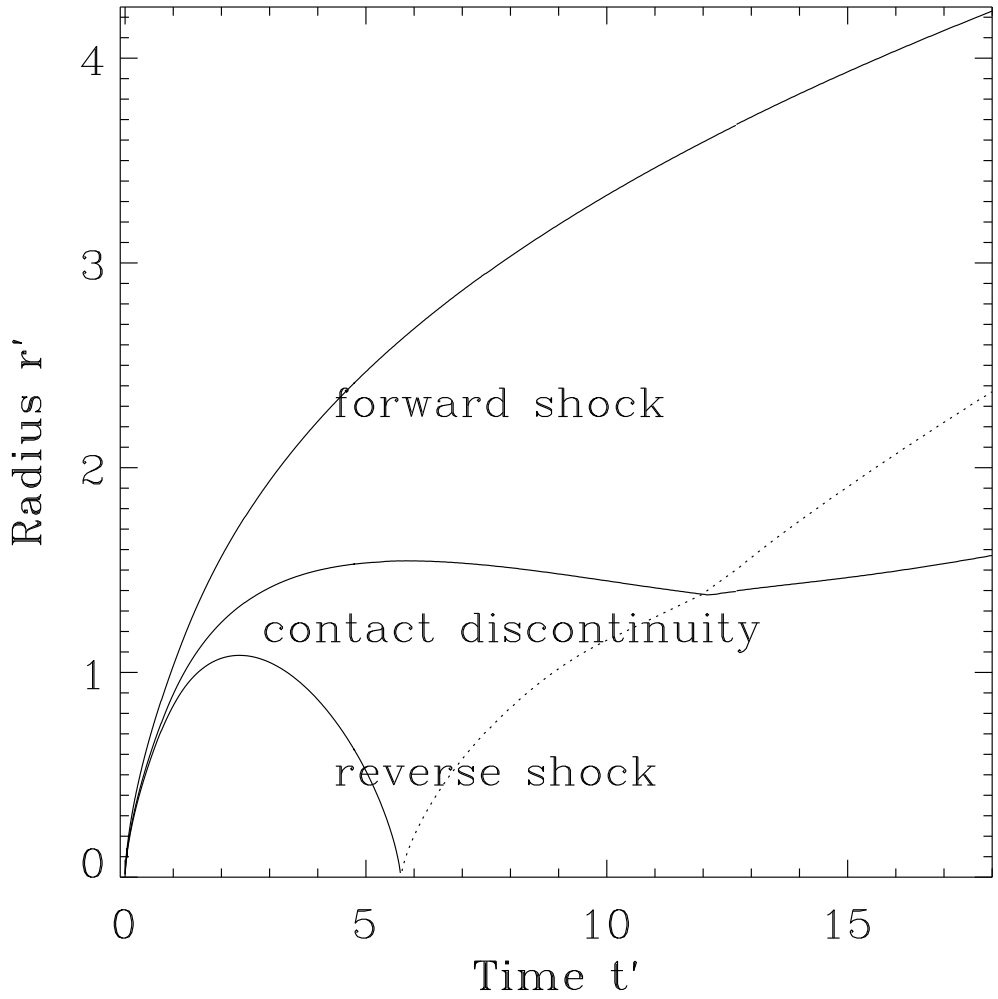


Figure 2.4: Evolution of the forward shock, the contact discontinuity, and the reverse shock radius with time. The dashed line shows the outgoing weak shock wave caused by the reflection of the reverse shock wave at the center (Wang & Chevalier 2002).

can be described approximately by assuming a point explosion in an uniform ambient density. Sedov (1959) derived the self-similar solution (namely Sedov solution or Sedov-Taylor solution) for the blast wave in such system and Shklovskii (1962) showed that the adiabatic phase of the SNR evolution is in which the Sedov solution applies exactly.

When the pre-shock pressure is negligibly small compared to that of the post-shock pressure, the gas flow is determined by two parameters, pre-shock density $n_0$ and explosion energy $E_0$. Derived from these parameters with the space and time variable, $r$ and $t$, the only dimensionless parameter is combined,

$$\xi \;=\; \left(\frac{\rho_1}{E_0}\right)^{1/5} \frac{r}{t^{2/5}} \tag{2.31}$$

Thus, the radius of the blast wave $R_s$, mean temperature just behind the shock front $T_s$,

and the velocity of the blast wave $v_s$ are described as

$$R_s = 5.0 \left(\frac{E_0}{10^{51}\mathrm{erg}}\right)^{1/5} \left(\frac{n_0}{1\mathrm{cm}^{-3}}\right)^{-1/5} \left(\frac{t}{1000\mathrm{yr}}\right)^{2/5} \mathrm{pc} \tag{2.32}$$

$$T_s = 4.5 \left(\frac{E_0}{10^{51}\mathrm{erg}}\right)^{2/5} \left(\frac{n_0}{1\mathrm{cm}^{-3}}\right)^{-2/5} \left(\frac{t}{1000\mathrm{yr}}\right)^{-6/5} \mathrm{keV} \tag{2.33}$$

$$v_s = \frac{2}{5}\frac{R_s}{t} \propto t^{-3/5} \tag{2.34}$$

Applying the parameter $\xi$ to the gas flow model expressed by equation of motion, continuity equation, and the law of the conservation of energy, the structure inside the blast wave is also determined uniquely (Figure 2.5).

Adiabatic phase continues until the adiabatic approximation becomes invalid for the radiative cooling. This phase lasts 10,000-20,000 yr.

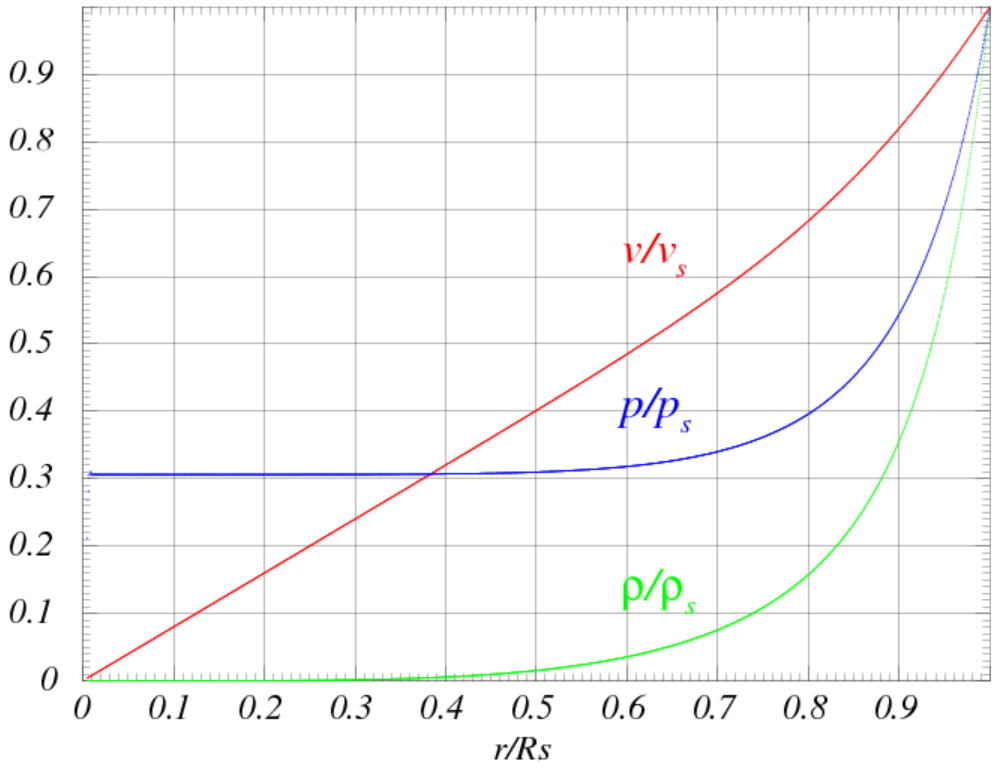


Figure 2.5: Structure inside the blast wave calculated from the Sedov model. Red, blue, and green represent the velocity, pressure, and density, respectively. These parameters are normalized at the values behind the shock front.

### Radiative Cooling Phase (Snowplow Phase)

As the radiative energy loss becomes considerably large compared with the internal energy of the SNR, its evolution moves into the third phase, radiative cooling phase. At this

phase, the shell of the SNR has cooled down to $\sim 10^6$ K. Thus, the density just behind the blast wave becomes higher and the shell radiates the energy more efficiently. As a result, the electrons recombine with the heavy elements and the shell becomes cooler and denser by a snowball effect.

During the early stage of this phase, the density and the temperature are still higher than those of the surrounding ISM. Therefore the shell expands by the internal pressure, sweeping up the surrounding ISM like a snow plowing. This stage is commonly termed pressure-driven snowplow (PDS) stage. The time-dependent radius and the time-dependent velocity of the shell are respectively described below (McKee & Ostriker 1977),

$$R_s \propto t^{2/7} \tag{2.35}$$

$$v_s \propto t^{-5/7}. \tag{2.36}$$

Even when the internal material becomes comparable in pressure to the surrounding ISM, the shell expansion is still driven by the remaining momentum. This stage called momentum-conserving snowplow (MCS) stage (Cioffi et al. 1988). The relations between the radius, temperature, and the time are

$$R_s \propto t^{1/4} \tag{2.37}$$

$$v_s \propto t^{-3/4}. \tag{2.38}$$

The radiative cooling phase lasts a few thousands of years.

#### Disappearance Phase

About millions of years after the SN explosion, the expansion velocity drops to the velocity of sound in the ISM. Outward expansion stops and the SNR becomes indistinguishable from the ISM due to Rayleigh-Taylor instabilities breaking the internal material away from the SNR's shell.

### 2.2.3 Classification

The radio observations show the SNRs have various structures (for example, see The MOST Supernova Remnant Catalogue[2]). Therefore, they are also classified according to their morphology in radio. The reasonable classification is as follows.

[2]http://www.physics.usyd.edu.au/sifa/Main/MSC

### Shell-type SNRs

Shell-type SNRs show limb brightened morphology both in radio and X-ray. The radio emission mainly comes through synchrotron radiation of relativistic electrons interacting with the interstellar galactic magnetic field (e.g., Jun & Norman 1996a,b). The X-ray emission mainly comes from the thermal plasma of the ISM and the ejecta heated by the blast wave and reverse shock, respectively (e.g., Chevalier 1982). Representative shell-type SNRs indicate the Cas A SNR, Tycho's SNR, and the Cygnus Loop. On the other hand, some SNRs show a synchrotron radiation in X-ray, such as SN 1006 (Koyama et al. 1995) and RX J1713.7-3946 (Koyama et al. 1997). The recent studies show that the young SNR such as Cas A, Tycho's SNR and Kepler's SNR are generally associated with non-thermal emission (Bamba et al. 2005a).

### Plerion (Crab-like/Center-filled-type) SNRs

Some SNRs have filled-center morphologies in radio. The most typical example is the well-known Crab SNR. The other examples are CTB87 and 3C58. For classification of this type of the SNRs, Weiler & Panagia (1978) first proposed the name, *plerion* derived from the ancient Greek word *pleres* which means "fullness". Plerion SNRs are also known as Crab-like SNRs (or simply center-filled-type SNRs).

The most of the Crab-like SNRs are believed to be energized by rapidly rotating pulsars, although not all the SNRs in this type have an observable pulsar. There are mainly two interpretations for the filled-center morphology: either that the surrounding ISM is very tenuous enough not to form a shell, or that the SN explosion did not produce enough amount of fast expanding ejecta due to the lack of the explosive energy (Green 1986).

### Composite-type SNRs

Composite-type SNRs have both the central (Crab-like) component and the shell component. The shell component is a thermal origin as those of the shell-type SNRs, while the central component has two different origins: non-thermal or thermal origin. The former SNRs are called non-thermal composite SNRs which are the traditional composite-type SNRs. The latter SNRs are called thermal composite SNRs or mixed-morphology (MM) SNRs (Rho & Petre 1998).

The example of the non-thermal composite SNRs are the Vela SNR, Puppis A, and CTB109, whereas W28, W44, and 3C391 are included in the MM SNRs.

## 2.3 Cygnus Loop Supernova Remnant

### 2.3.1 Brief Historical Overview

The Cygnus Loop SNR (G74.0-8.5) is also known as *Veil Nebula* (*Veil Remnant*) in optical, H II region Sharpless 103 or radio source W78. Parts of the Cygnus Loop are also listed in the New General Catalog as NGC 6960 (*Witch's Broom Nebula*), 6979, 6992, and 6995, respectively.

From a historical point of view, the Cygnus Loop was discovered and recorded on 5, September, 1774 by William Herschel. The region he observed was the brightest one in the Cygnus Loop: the northeast and the southwest optical filaments. Hubble (1937) reported the proper motions of these filaments ($0.03''$/yr) and Oort (1946) first suggested that the Cygnus Loop is an expanding SNR shell. Minkowski (1958) measured the radial velocities of the optical filaments and estimated its distance to be 770 pc.

The Cygnus Loop has also been detected at various other wavelength bands such as synchrotron radio emission (e.g., Keen et al. 1973; Green 1990), infrared (IR) emission (Braun & Strom 1986), ultraviolet (UV) radiation (Blair et al. 1991), and X-ray (Gorenstein et al. 1971, first report in X-ray).

### 2.3.2 Previous Studies in X-ray

The Cygnus Loop is one of the brightest and the largest SNR in the X-ray sky. Blair et al. (2005) measured its distance more accurately than before to be $540^{+100}_{-80}$ pc and estimated its age to be $\sim$ 10,000 yr, hence the middle-aged (evolved) SNR. Since the distance is comparatively close to us, the apparent size is quite large ($2.5^\circ \times 3.5^\circ$; Levenson et al. 1997), which enables us to study the plasma structure in detail.

#### Cavity Explosion

As reported by many previous studies, the origin of the Cygnus Loop is thought to be a cavity explosion; McCray & Snow (1979) proposed that the SN explosion had occurred in a preexisting cavity and some other studies also supported this result (e.g., Hester & Cox 1986; Hester et al. 1994; Levenson et al. 1997). Hester et al. (1994) observed the Balmer-dominated northeast limb of the Loop and showed the blast wave was decelerated from $\sim$ 400 km s$^{-1}$ to less than 200 km s$^{-1}$ in the last 1,000 yr, which suggests that the blast wave is now propagating into a cavity wall. Since the Cygnus Loop is an evolved shell-like SNR, the spectra from the limb regions should mainly consist of the shock-heated cavity material.

### Shell Structure and Surrounding Environment

From the morphological point of view, the Cygnus Loop is a typical shell-like SNR. In general, many SNRs have asymmetric morphologies depending on its nonuniform surrounding ISM. However, despite the evolved SNR, the Cygnus Loop is almost circular in shape. This structure is thought to be generated by a cavity explosion (Levenson et al. 1997); If the stellar wind of the progenitor star blew off the surrounding ISM before the SN explosion, the blast waves have expanded inside the cavity of almost uniform density after the SN explosion, hence nearly circular morphology.

An irregular structure is seen at the South shell of the Loop. This region is known as "blowout" region (Aschenbach & Leahy 1999). Aschenbach & Leahy (1999) explained this extended structure as a breakout into a lower density ISM. On the other hand, based on a radio observation, Uyaniker et al. (2002) suggested the existence of a secondary SNR in the south. Some other radio observations support this conclusion (Uyaniker et al. 2004; Sun et al. 2006). In any case, the origin of the "blowout" remains incompletely understood.

The ISM (or cavity-material) component is dominant in the spectra obtained from limb regions. Therefore, the spectral analysis for a limb region provides a clue to obtaining the information about the surrounding environment of the Cygnus Loop. Miyata et al. (2007) observed the northeast limb (namely NE2) of the Cygnus Loop with the *Suzaku* observatory and showed the abundances of C to Fe to be depleted (typically $\sim 0.1$ times solar). Katsuda et al. (2008b) expanded their observation northward (NE1-NE4; including the FOV of Miyata et al. 2007) with *Suzaku* and found that a portion of their FOV, the outer edge of the limb in NE3-NE4, only shows the relatively high abundances while the other regions are uniformly depleted. Katsuda et al. (2008c) also confirmed it by *Chandra* . Tsunemi et al. (2009) also found the abundance-enhanced region at the southeastern limb with the *Suzaku* observatory. Although Katsuda et al. (2008c) and Tsunemi et al. (2009) discussed a few possibilities for the origin of the abundance inhomogeneities, the origin of these inhomogeneities remains in question.

### Ejecta Distribution and Progenitor Star

Although the Cygnus Loop is an evolved SNR, a hot plasma is still confined inside the Loop (Tsunemi et al. 1988; Hatsukade & Tsunemi 1990). Miyata et al. (1998) observed the Loop with *ASCA*, and detected strong highly-ionized Si-K, S-K, and Fe-L lines near the center of the Cygnus Loop. They concluded that a hot plasma, a "fossil" of the supernova explosion, is left in the core of the Loop. Tsunemi et al. (2007) observed

the Cygnus Loop along the diameter from the northeast to the southwest with *XMM-Newton* and studied the radial plasma structure. From the spectral analysis, they showed that the Cygnus Loop consists of two components with different temperatures and metal abundances. They concluded that the low-$kT_e$ component originating from the cavity-wall component surrounds the high-$kT_e$ ejecta component. In addition, they measured the metal abundances of the high-$kT_e$ component and showed the metal distribution of the ejecta. The results indicate that the abundances are relatively high ($\sim$ 5 times solar) and each element is non-uniformly distributed: Si, S and Fe are concentrated in the inner region while the other elements such as O, Ne and Mg are abundant in the outer region. Katsuda et al. (2008a) and Kimura et al. (2009) expanded the observations southward and northward respectively with the *Suzaku* observatory in 7 and 10 pointings, and examined the plasma structure in their FOV. Katsuda et al. (2008a) divided their FOV into 119 cells and, performed the spectral analysis. They showed that Si and Fe are more concentrated in the south part than that in the north part. This indicates a clear asymmetric structure of the metal abundances. Kimura et al. (2009) divided their FOV into 45 rectangular regions from northeast to southwest and also showed the asymmetric distribution of each heavy element; the ejecta of O, Ne, Mg are distributed more in the NE, while those of Si, Fe are distributed more in the southwest. It is striking that an asymmetric explosion is suggested as the origin of the Cygnus Loop from the metal distributions.

Tsunemi et al. (2007) and Kimura et al. (2009) also calculated the progenitor mass of the Cygnus Loop and concluded that the Cygnus Loop is originated from the 12-15$M_\odot$ explosion. Levenson et al. (1998) also estimated the progenitor mass to be 15$M_\odot$ judging from the size of the cavity. These results strongly suggest that the progenitor star of the Cygnus Loop was a massive star and caused a core-collapse explosion rather than a Type Ia SN explosion. However, the results of Tsunemi et al. (2007) and Kimura et al. (2009) show the tendancy that the observed Fe is several times higher than that of the model. Futhermore, a compact source such as a neutron star has not been detected ever from the Cygnus Loop. These two points still remain open questions.

# Chapter 3

# Instruments

We mainly used the data obtained from the *XMM-Newton* EPIC and the *Suzaku* XIS for the analysis of the Cygnus Loop. This section gives the overviews of these satellites and instruments.

## 3.1 XMM-Newton

### 3.1.1 Overview

X-ray Multi-Mirror Mission (XMM) - Newton (hereafter *XMM-Newton* [1]; Jansen et al. 2001) is the second X-ray astronomy mission of European Space Agency (ESA). It was launched on December 10, 1999, by ESA with an Ariane 504 from the Guiana Space Centre, Europe's space port (French Guiana) and put into a highly elliptical orbit with an apogee of about 115,000 km and a perigee of 6,000 km with an inclination angle of 54.3° . The orbital period is 47.9 hours. Figure 3.1 shows the sketch of the *XMM-Newton*.

*XMM-Newton* includes three types of scientific instruments: European Photon Imaging Camera (EPIC; Turner et al. 2001; Strüder et al. 2001), Reflection Grating Spectrometer (RGS; den Herder et al. 2001), and Optical/UV Monitor (OM; Mason et al. 2001).

EPIC is equipped for X-ray imaging, moderate resolution spectroscopy, and X-ray photometry. It consists of two different types of charge-coupled device (CCD) camera, MOS (Metal Oxide Semi-conductor; Turner et al. 2001) and pn (Strüder et al. 2001). RGS consists of two essentially identical spectrometers for high-resolution X-ray spectroscopy and spectro-photometry Both EPIC and RGS are on the focal plane of the X-ray telescopes, while the OM has its own telescope. OM is a optical/UV detector for

[1] http://xmm.vilspa.esa.es/external/xmm_user_support/documentation/uhb_2.5/index.html

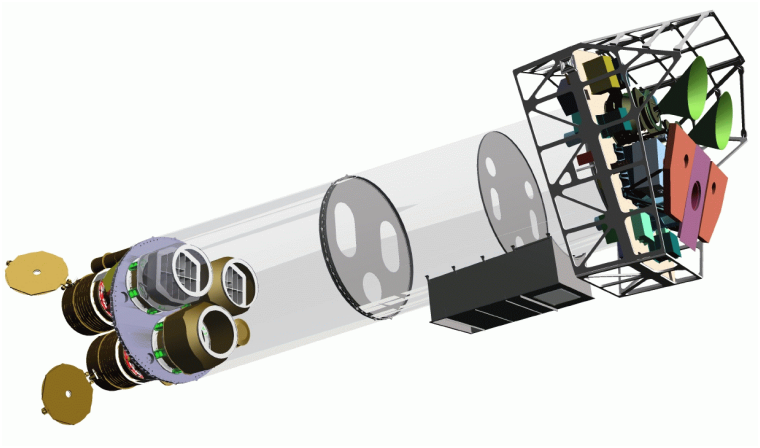

Figure 3.1: Sketch of the *XMM-Newton* observatory. To the left the three mirror modules (with the Reflection Gration Arrays units mounted behind two of them) can be seen, while at the right the back-end of the instrument platform with all the radiators is visible; the EPIC-MOS cameras with their radiators in green, the radiator of the EPIC-pn camera in violet, and the RGS detectors in orange (Jansen et al. 2001).

imaging and grism spectroscopy. Among these instruments, we used the data obtained from EPIC. The overview of the EPIC is discussed in the following section.

### 3.1.2 EPIC

EPIC consists of three cameras: two MOS (namely MOS1 and MOS2) and one pn. The detectors of MOS are the front-illuminated (FI) CCDs whereas that of pn is a back-illuminated (BI) CCD. Figure 3.2 shows schematic views of the field of view (FOV) of the two types of EPIC camera; MOS (*left*) and pn (*right*). Generally speaking, the quantum efficiency and the timing resolution are better in pn than those in MOS, whereas MOS has better spectral resolution than pn. Figure 3.3 shows the effective area of each EPIC camera. The basic properties of the EPIC are summarized in Table 3.1.

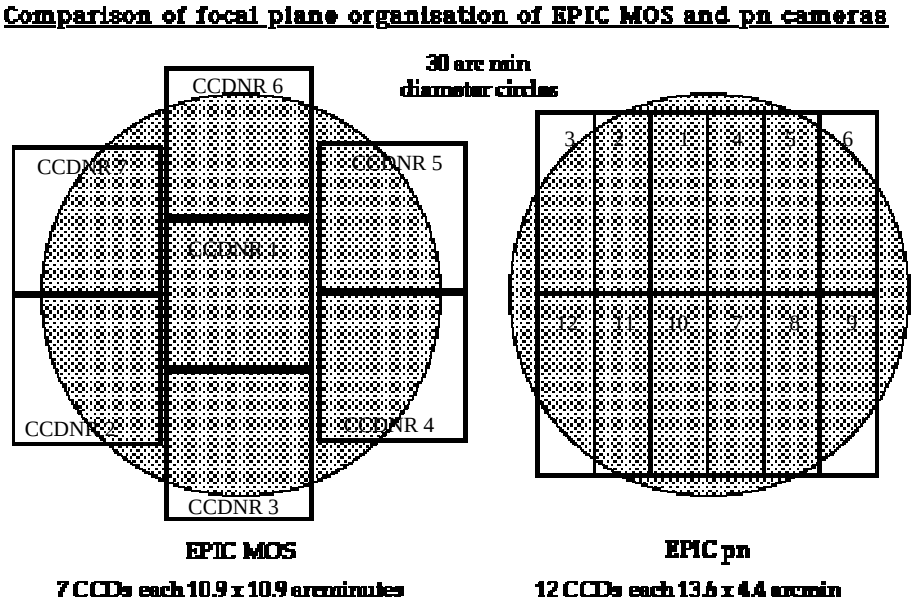


Figure 3.2: Schematic views of the FOV of the EPIC cameras; MOS (*left*) and pn (*right*). The shaded circle depicts a 30′diameter area.

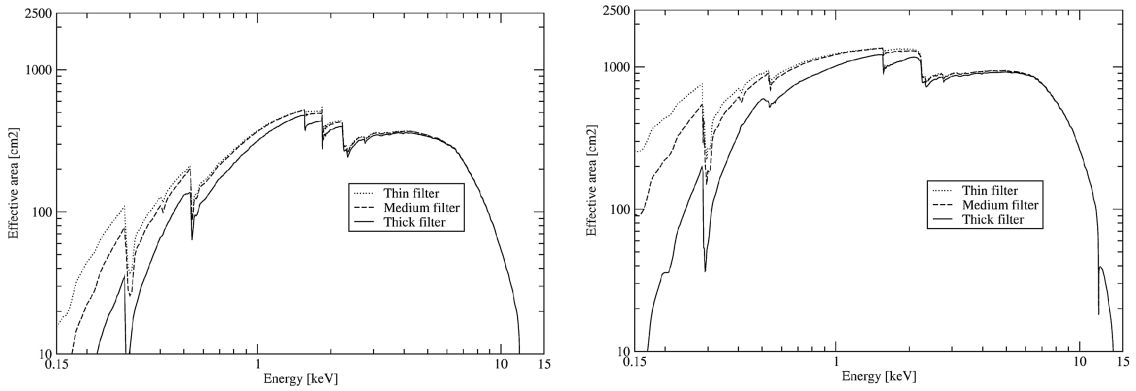


Figure 3.3: The effective area curves of the EPIC MOS (left) and the EPIC pn (right).

Table 3.1: Basic properties of the EPIC

| | EPIC MOS | EPIC pn |
|---|---|---|
| Illumination method | Front Illuminated | Back Illuminated |
| Energy range | 0.15-12 keV | 0.15-15 keV |
| Energy resolution (FWHM) | $\sim$ 140 eV at 5.9 keV | $\sim$ 170 eV at 5.9 keV |
| Field of View | $30'$ diameter | $30'$ diameter |
| Pixel grid | 600×600 | 398×384 |
| PSF (HPD) | $14''$ | $15''$ |
| Timing resolution | 1.75 ms | 0.03 ms |

## 3.2 Suzaku

### 3.2.1 Overview

*Suzaku* [2] (formerly named Astro-E2) (Mitsuda 2007) is Japanese fifth cosmic X-ray astronomy mission. *Suzaku* is developed by the Institute of Space and Astronautical Science (ISAS) of Japan Aerospace Exploration Agency (JAXA) in collaboration with the National Aeronautics and Space Administration's Goddard Space Flight Center (NASA/GSFC) and many other institutions. Figure 3.4 shows the schematic views of *Suzaku*. *Suzaku* was successfully launched on July 10, 2005, by JAXA with the M-V launch vehicle from the Uchinoura Space Center (USC). *Suzaku* first deployed solar paddles and an extensible optical bench (EOB), and was put into a roughly circular orbit at 570 km altitude with an inclination angle of 31° . The orbital period is about 96 minutes.

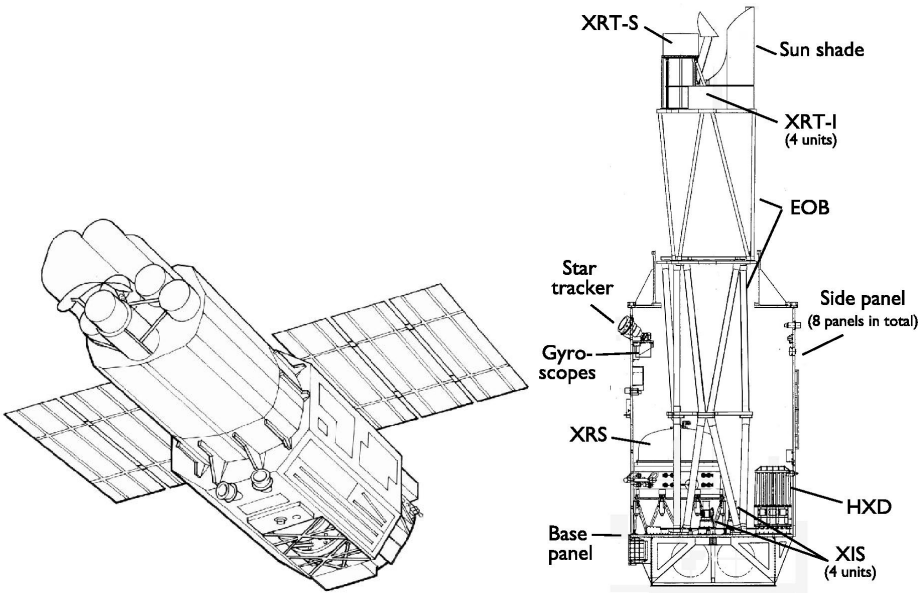


Figure 3.4: Schematic views of *Suzaku* (Mitsuda 2007).

*Suzaku* includes three scientific instruments: four X-ray sensitive silicon CCD cameras (X-ray Imaging Spectrometer, XIS; Koyama et al. 2007), non-imaging, collimated Hard X-ray Detector (HXD; Takahashi et al. 2007), and X-ray Spectrometer (XRS; Kelley 2007).

Each XIS is on the focal plane of an X-ray Telescope (XRT; Serlemitsos 2007) which is installed on the top plate of the EOB. The main targets of the XIS are soft X-ray sources ($< 12$ keV), whereas the HXD extends the bandpass of the observatory to much

[2] http://www.astro.isas.ac.jp/suzaku/doc/suzaku_td/

higher energies (10-600 keV; Kokubun 2007). Although the XRS has a superior energy resolution (7 eV in the energy range 0.3 to 12 keV), the system became inoperable due to a thermal short between the helium and neon tanks which resulted in the liquid helium coolant venting to space.

For the *Suzaku* observations of the Cygnus Loop, we used the data taken by the XIS detectors. The detailed view of the XIS is discussed in the following section.

### 3.2.2 XIS

The XIS consists of four sensors: XIS0, XIS1, XIS2, and XIS3. All sensors were developed through the collaboration of the Center for Space Research at Massachusetts Institute of Technology, ISAS/JAXA, Osaka Univ., Kyoto Univ., Rikkyo Univ., Kogakuin Univ., and Ehime Univ. The XIS employs sensitive silicon CCD, which are operated in a photon-counting mode, similar to that used in the *Advanced Satellite for Cosmology and Astrophysics* (*ASCA*) SIS (Solid-state Imaging spectrometers; Burke et al. 1998; Yamashita 1997), *Chandra* ACIS (Garmire et al. 1992; Bautz et al. 1998), and *XMM-Newton* EPIC.

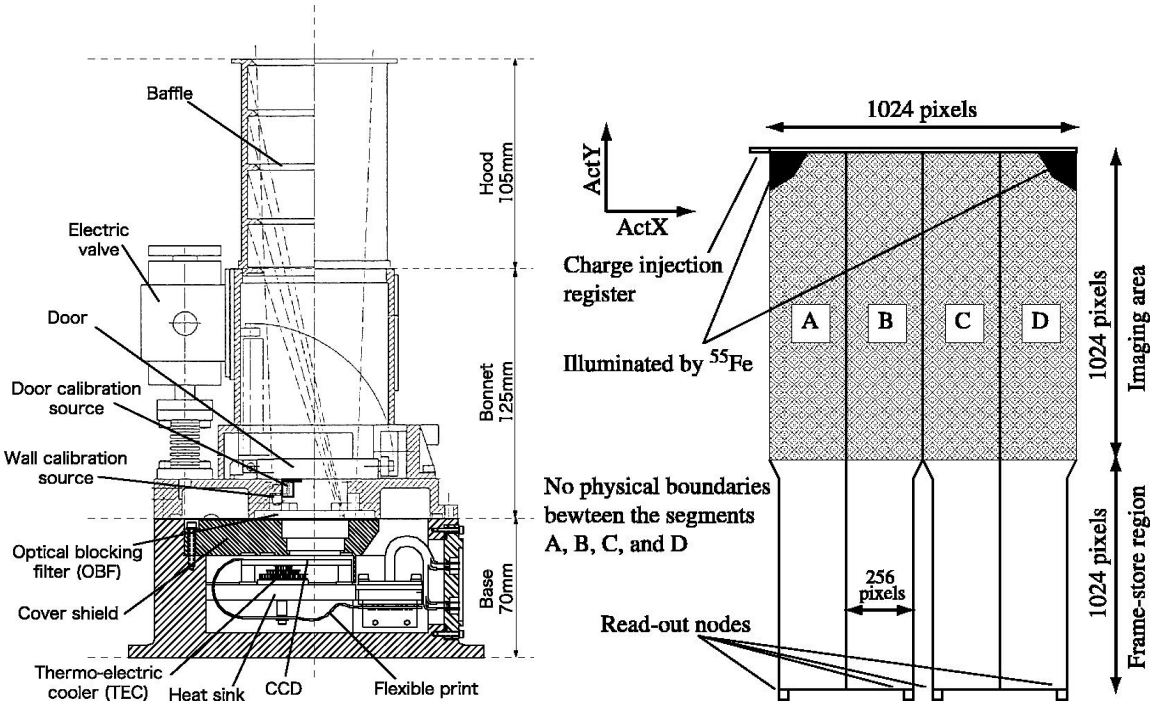


Figure 3.5: Schematic views of *Suzaku* XIS system (left) and XIS CCD (right) (Koyama et al. 2007).

Figure 3.5 shows the schematic views of *Suzaku* XIS system (left) and XIS CCD

(right). Each CCD camera has a single CCD chip with an array of 1024×1024 pixels, and covers an $17'.8 \times 17'.8$ region on the sky. Each pixel is $24\,\mu$m square, and the size of the CCD is 25 mm × 25 mm. A back-illuminated BI CCD is adopted for XIS1, while the other XIS (XIS0, XIS2, and XIS3) are the FI CCDs. Figure 3.6 shows the quantum efficiency (*left*) and the effective area (*right*) of the XIS. They are the MOS-type three-phase CCDs operated in a frame transfer mode. The basic properties of the XIS are summarized in Table 3.2.

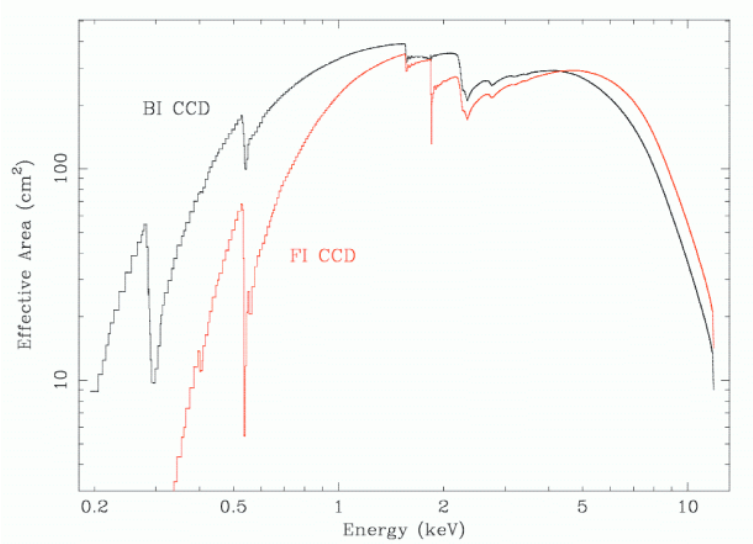


Figure 3.6: The effective area curves of one XRT+XIS system, for both the FI and BI CCDs.

The XIS2 showed anomaly on November 9, 2006, 1:03 UT. About 2/3 of the imaging area became suddenly unusable. The anomalous area was flooded with a large amount of charge, which was leaked somewhere in the imaging region. In spite of efforts by the *Suzaku* team, XIS2 has not yet been recovered. Therefore, we used only XIS0, 1, and 3 data obtained from the observations since November 9, 2006.

Table 3.2: Basic properties of the XIS

| | XIS |
|---|---|
| Energy range | 0.2-12 keV |
| Energy resolution (FWHM) | $\sim 130$ eV at 5.9 keV |
| Field of View | $17'.8 \times 17'.8$ |
| Pixel grid | 1024×1024 |
| PSF (HPD) | $2'$ |
| Timing resolution | 8 s (normal mode), 7.8 ms (P-sum mode) |

# Chapter 4

# Observations and Data Reductions

The X-ray spectra from the Cygnus Loop show various emission lines of heavy elements blown off by the SN explosions. Since these elements are generated by the nucleosynthesis process inside the progenitor stars, the metal abundance pattern provides a clue to obtaining the information about the type of the SN explosion and the condition of the progenitor star of the Cygnus Loop.

We have observed the Cygnus Loop with *XMM-Newton* (9 pointings) and *Suzaku* (32 pointings) between 2002 and 2008. Thanks to their good energy resolution and spatial resolution, these two observatories are suitable for investigating the plasma structure of the Cygnus Loop. Their FOV are shown in figure 4.1. Since the ways of the data reduction are common in most of the following analyses, we summarize them for both the *XMM-Newton* MOS data in Section 4.1 and the *Suzaku* XIS data in Section 4.2, respectively.

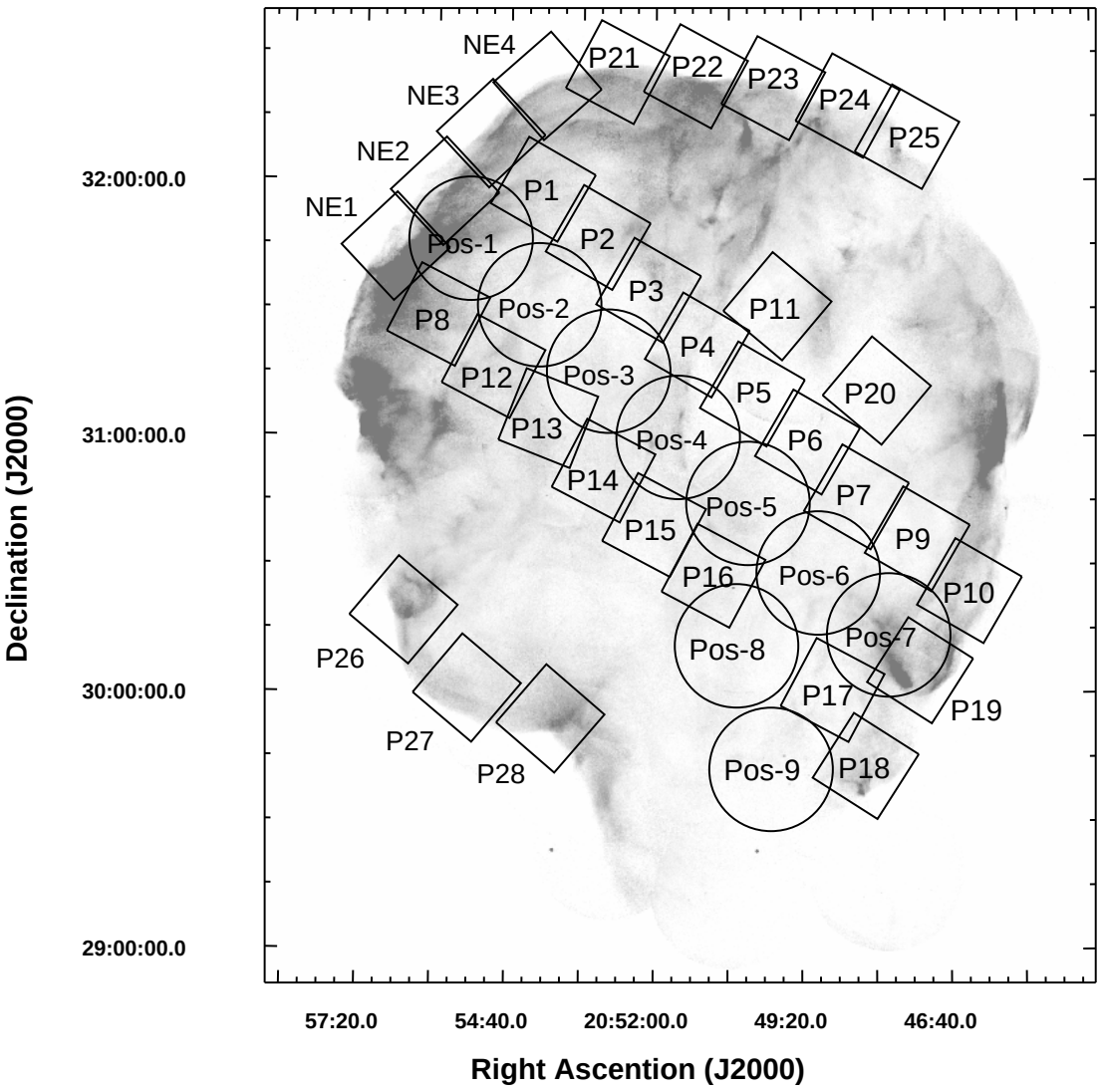


Figure 4.1: *ROSAT* HRI image of the entire Cygnus Loop. The circles and rectangles represent our FOV of the *XMM-Newton* MOS and the *XMM-Newton* XIS, respectively.

## 4.1 XMM-Newton Observations

All *XMM-Newton* observations of the Cygnus Loop are summarized in table 4.1. Pos-1 to Pos-7 were observed in 2002, while other two regions were observed in 2006.

Table 4.1: Summary of the 9 *XMM-Newton* observations

| Obs. ID | Obs. Date | R.A., Decl. (J2000) | Pos. Angle | Effective Exposure |
|---|---|---|---|---|
| *XMM-Newton Observations* | | | | |
| 0082540101 (Pos-1) | 2002-Nov-25 | $20^{h}55^{m}23^{s}.6$, $31°46'17''.0$ | $241°.7$ | 14.7 ksec |
| 0082540201 (Pos-2) | 2002-Dec-03 | $20^{h}54^{m}07^{s}.2$, $31°30'51''.1$ | $241°.7$ | 14.4 ksec |
| 0082540301 (Pos-3) | 2002-Dec-05 | $20^{h}52^{m}51^{s}.1$, $31°15'25''.7$ | $241°.7$ | 11.6 ksec |
| 0082540401 (Pos-4) | 2002-Dec-07 | $20^{h}51^{m}34^{s}.7$, $31°00'00''.0$ | $241°.7$ | 4.9 ksec |
| 0082540501 (Pos-5) | 2002-Dec-09 | $20^{h}50^{m}18^{s}.4$, $30°44'34''.3$ | $231°.4$ | 12.6 ksec |
| 0082540601 (Pos-6) | 2002-Dec-11 | $20^{h}49^{m}02^{s}.0$, $30°29'08''.6$ | $241°.7$ | 11.5 ksec |
| 0082540701 (Pos-7) | 2002-Dec-13 | $20^{h}47^{m}45^{s}.8$, $30°13'42''.9$ | $241°.7$ | 13.7 ksec |
| 0405490101 (Pos-8) | 2006-May-13 | $20^{h}50^{m}32^{s}.2$, $30°11'00''.0$ | $69°.9$ | 6.5 ksec |
| 0405490201 (Pos-9) | 2006-May-13 | $20^{h}49^{m}54^{s}.2$, $29°42'25''.0$ | $69°.8$ | 3.6 ksec |

All the *XMM-Newton* data were processed with version 7.1.0 of the *XMM* Science Analysis System (SAS). The current calibration files (CCFs) used were up-to-date ones at the time of each analysis. We used data obtained with the EPIC MOS and pn cameras. These data were taken by using the medium filters and the prime full-window mode. We selected X-ray events corresponding to patterns 0-12 and flag = 0 for MOS 1 and 2, patterns 0-4 and flag = 0 for pn, respectively. In order to exclude background flare events, we determined the GTIs in the same way as those of the *Suzaku* data as we discuss later. After filtering the data, they were vignetting-corrected by using the SAS task **evigweight**. For background subtraction, we employed blank-sky observations prepared by Read & Ponman (2003) for a similar reason with the *Suzaku* case as we discuss later. After the background subtraction, the energy range of 0.3-3.0 keV was used for each instrument. The point-like sources were excluded using the SAS task *edetect chain* for the spectral analysis.

In order to generate a response matrix file (RMF) and an ancillary response file (ARF), we employed *rmfgen* and *arfgen* for the *XMM-Newton* data.

## 4.2 Suzaku Observations

All *Suzaku* observations of the Cygnus Loop are summarized in table 4.2. They were observed between 2005 and 2008

All the *Suzaku* data were analyzed with version 6.6.2 of the HEAsoft[1] tools. For the reduction of the *Suzaku* data, we used the version 9 of the Suzaku Software. The calibration database (CALDB) used was up-to-date ones at the times of the analyses. We used the revision 2.2 of the cleaned event data and combined the 3×3 and 5×5 event files. The data obtained after the P6 observation (November 2007) were all taken by using the spaced row charge injection (SCI) method (Prigozhin et al. 2008) which reduces the effect of radiation damage of the XIS and recovers the energy resolution, for example, from 205±6 eV to 157±4 eV at the He-like Fe K line. In order to exclude the background flare events, we obtained the good time intervals (GTIs) by including only times at which the count rates are within $\pm 3\sigma$ of the mean count rates.

The Cygnus Loop is a large diffuse source and our FOV are almost filled with the SNR's emission. We also have no background data from the neighborhood of the Cygnus Loop. We therefore applied the Lockman Hole data for the background subtraction of the *Suzaku* data. We reviewed the effect of the Galactic Ridge X-ray Emission (GRXE). The flux of the GRXE at $l = 62°$, $|b| < 0°.4$ is $6 \times 10^{-12}$ erg·cm$^{-2}$s$^{-1}$deg$^{-2}$ (0.7-2.0 keV) (Sugizaki et al. 2001). Although the Cygnus Loop ($l = 74°$, $b = -8°.6$) is located outside of the FOV of Sugizaki et al. (2001), this value gives us an upper limit of the GRXE at the Cygnus Loop. Meanwhile, the flux of the Cygnus Loop is estimated to be $8.21 \times 10^{-10}$ erg cm$^{-2}$s$^{-1}$deg$^{-2}$ (0.7-2.0 keV), assuming that the Cygnus Loop is a circle with a diameter of 3°.0. As a result, we concluded that the effect of the GRXE on the Cygnus Loop is vanishingly small. The solar wind charge exchange (SWCX) is also considered to be one of the correlates of the soft X-ray background below 1 keV (Fujimoto et al. 2007). However, in terms of the Cygnus Loop, we consider that the SWCX is negligible because of the prominent surface brightness of the Loop. Thus, for the background subtraction of *Suzaku* data, the Lockman Hole data obtained in 2006, 2007 and 2008 were applied. These observation dates were close to those of the Cygnus Loop observations and we confirmed that they have no background flares below 1 keV. Since there were no photons above 5.0 keV after the background subtraction, the energy ranges of 0.2-5.0 keV and 0.4-5.0 keV were used for XIS1 (BI CCD) and XIS023 (FI CCD), respectively (Koyama et al. 2007).

In order to generate a RMF and an ARF, we employed *xisrmfgen* (Ishisaki et al.

[1]http://heasarc.gsfc.nasa.gov/lheasoft/

2007) and *xissimarfgen* for the *Suzaku* data.

Table 4.2: Summary of the 32 *Suzaku* observations

| Obs. ID | Obs. Date | R.A., Decl. (J2000) | Pos. Angle | Effective Exposure |
|---|---|---|---|---|
| *Suzaku Observations* | | | | |
| 501012010 (P1) | 2007-Nov-14 | $20^h54^m07^s.6$, $31°57'22''.0$ | $240°.0$ | 9.8 ksec |
| 501013010 (P2) | 2007-Nov-14 | $20^h53^m08^s.5$, $31°45'40''.3$ | $240°.0$ | 16.4 ksec |
| 501014010 (P3) | 2007-Nov-14 | $20^h52^m09^s.9$, $31°36'43''.4$ | $240°.0$ | 16.9 ksec |
| 501015010 (P4) | 2007-Nov-14 | $20^h51^m11^s.8$, $31°22'08''.4$ | $240°.0$ | 18.3 ksec |
| 501016010 (P5) | 2007-Nov-15 | $20^h50^m11^s.3$, $31°10'48''.0$ | $240°.0$ | 19.3 ksec |
| 501017010 (P6) | 2007-Nov-11 | $20^h49^m11^s.3$, $30°59'27''.6$ | $240°.0$ | 28.7 ksec |
| 501018010 (P7) | 2007-Nov-12 | $20^h48^m18^s.7$, $30°46'33''.6$ | $240°.0$ | 21.0 ksec |
| 501028010 (P8) | 2006-May-13 | $20^h55^m56^s.3$, $31°28'56''.2$ | $62°.5$ | 4.9 ksec |
| 501019010 (P9) | 2007-Nov-12 | $20^h47^m14^s.2$, $30°36'10''.8$ | $240°.0$ | 16.2 ksec |
| 501020010 (P10) | 2007-Nov-13 | $20^h46^m20^s.8$, $30°23'22''.6$ | $240°.0$ | 14.7 ksec |
| 503055010 (P11) | 2008-May-09 | $20^h49^m48^s.7$, $31°30'18''.0$ | $50°.0$ | 22.2 ksec |
| 501029010 (P12) | 2006-May-09 | $20^h55^m00^s.0$, $31°15'46''.8$ | $62°.1$ | 13.2 ksec |
| 501030010 (P13) | 2006-May-10 | $20^h53^m59^s.3$, $31°03'39''.6$ | $68°.2$ | 13.9 ksec |
| 501031010 (P14) | 2006-May-12 | $20^h52^m58^s.8$, $30°51'32''.4$ | $62°.4$ | 18.2 ksec |
| 501032010 (P15) | 2006-May-25 | $20^h51^m58^s.6$, $30°39'10''.8$ | $62°.0$ | 17.4 ksec |
| 501033010 (P16) | 2006-May-22 | $20^h50^m58^s.8$, $30°27'00''.0$ | $62°.0$ | 20.0 ksec |
| 501034010 (P17) | 2006-May-22 | $20^h48^m49^s.7$, $30°00'21''.6$ | $62°.0$ | 13.9 ksec |
| 501035010 (P18) | 2006-Dec-18 | $20^h48^m16^s.2$, $29°42'07''.2$ | $237°.5$ | 11.2 ksec |
| 501036010 (P19) | 2006-Dec-18 | $20^h47^m17^s.3$, $30°04'21''.4$ | $237°.5$ | 11.8 ksec |
| 503056010 (P20) | 2008-May-10 | $20^h48^m00^s.0$, $31°10'30''.0$ | $50°.0$ | 22.5 ksec |
| 503057010 (P21) | 2008-Jun-02 | $20^h52^m43^s.8$, $32°26'19''.0$ | $61°.9$ | 16.2 ksec |
| 503058010 (P22) | 2008-Jun-03 | $20^h51^m17^s.2$, $32°25'24''.6$ | $61°.4$ | 19.3 ksec |
| 503059010 (P23) | 2008-Jun-03 | $20^h49^m50^s.6$, $32°21'50''.8$ | $61°.9$ | 19.5 ksec |
| 503060010 (P24) | 2008-Jun-04 | $20^h48^m28^s.2$, $32°17'44''.5$ | $61°.4$ | 18.5 ksec |
| 503061010 (P25) | 2008-Jun-04 | $20^h47^m22^s.7$, $32°10'22''.8$ | $60°.9$ | 26.0 ksec |
| 503062010 (P26) | 2008-May-13 | $20^h56^m26^s.5$, $30°19'55''.2$ | $49°.8$ | 16.9 ksec |
| 503063010 (P27) | 2008-May-13 | $20^h55^m16^s.3$, $30°01'44''.0$ | $49°.6$ | 22.8 ksec |
| 503064010 (P28) | 2008-May-14 | $20^h53^m51^s.6$, $29°54'42''.5$ | $49°.1$ | 18.2 ksec |
| 500020010 (NE1) | 2005-Nov-23 | $20^h56^m48^s.9$, $31°56'54''.8$ | $223°.0$ | 20.4 ksec |
| 500021010 (NE2) | 2005-Nov-24 | $20^h55^m56^s.0$, $31°56'53''.2$ | $223°.0$ | 21.4 ksec |
| 500022010 (NE3) | 2005-Nov-29 | $20^h55^m05^s.6$, $32°10'35''.4$ | $222°.9$ | 21.7 ksec |
| 500023010 (NE4) | 2005-Nov-30 | $20^h54^m03^s.8$, $32°21'47''.9$ | $221°.2$ | 25.3 ksec |

# Chapter 5

# Shell Structure

In this chapter, we discuss about the shell structure of the Cygnus Loop. In Section 5.1 and 5.2, we present the results of the southwest and the northeast obwervations of the Cygnus Loop, respectively. We also show the results of the comprehensive study of the shell structure in Section 5.3.

## 5.1 South Blowout Region

As explained in Chapter 2, the origin of the south blowout is still unclear. In order to investigate the plasma structure of the blowout region in X-ray, we observed it in two pointings with *XMM-Newton*.

Section 5.1 is based on the results of Uchida et al. (2008).

### 5.1.1 Observations

Figure 5.1 right shows a three-color X-ray image of our FOV using *XMM-Newton* EPIC MOS 1 and 2 data after correcting for exposure and vignetting effects. Red, green and blue correspond to the energy ranges of 0.3-0.5 keV, 0.5-0.7 keV and 0.7-3.0 keV, respectively.

We call the north observation for Position-8 (Pos-8) and the south observation for Position-9 (Pos-9) (see Figure 4.1). If there exists a secondary SNR (namely G72.9-9.0) in southwest as Uyaniker et al. (2002) mentioned, our whole FOV overlaps the SNR whose center is roughly located at the south in Pos-9. Figure 5.2 shows the MOS broad-band image for the 0.3-3 keV range. The white X shows the center of the G72.9-9.0 estimated by Uyaniker et al. (2002).

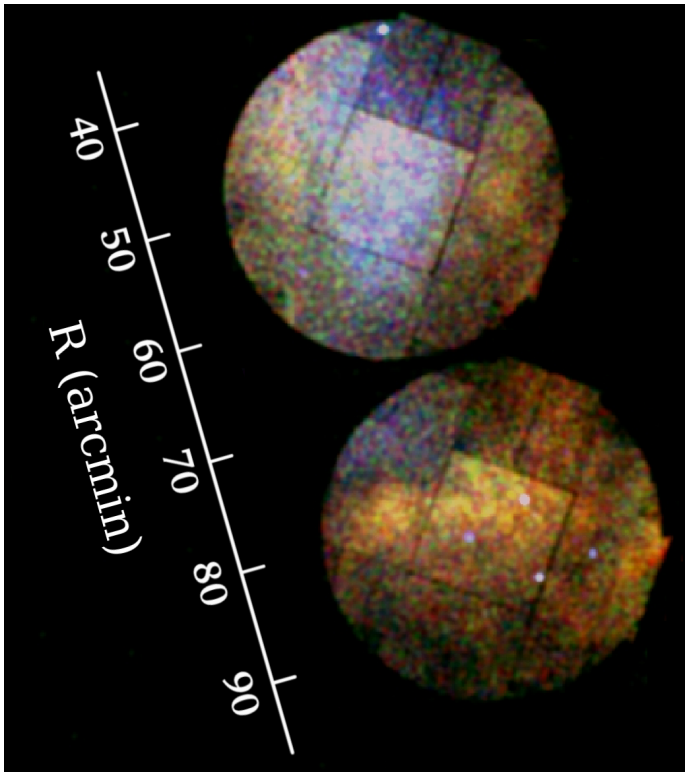


Figure 5.1: Three-color X-ray image for Pos-8 and 9 using EPIC MOS 1 and 2 data.

### 5.1.2 Spectral Analysis

#### Two-component VNEI Model

Figure 5.3 shows the spectra for Pos-8 and Pos-9 summed over the entire FOV. We can see some emission lines such as O He$\alpha$, O Ly$\alpha$, the Fe L complex, Ne He$\alpha$, Mg He$\alpha$, and Si He$\alpha$, while S lines are not seen here.

Firstly, we fitted each spectrum by single-component variable abundance non-equilibrium ionization (VNEI) model. We employed **Wabs** (Morrison & McCammon 1983) and **VNEI** (NEI ver.2.0; Borkowski et al. 2001) in XSPEC version 12.3.1 (Arnaud 1996). In the model, the abundances of O, Ne, Mg, Si, and Fe were free while we set the abundances of C and N equal to O, S equal to Si, Ni equal to Fe, and other elements fixed to their solar values (Anders & Grevesse 1989). Other parameters were all free such as the electron temperature $kT_e$, the ionization timescale $\tau$ (a product of the electron density and the elapsed time after the shock heating), and the emission measure (EM $= \int n_e n_H dl$, where $n_e$ and $n_H$ are the number densities of hydrogen and electrons and $dl$ is the plasma depth). We also set the absorption column density $N_{\rm H}$ to be free. From the best-fit parameters, we found that the value of $kT_e$ ($\sim$0.4 keV) is higher than that of the result at the northest limb obtained from *Suzaku* observations ($\sim$ 0.2 keV; Katsuda

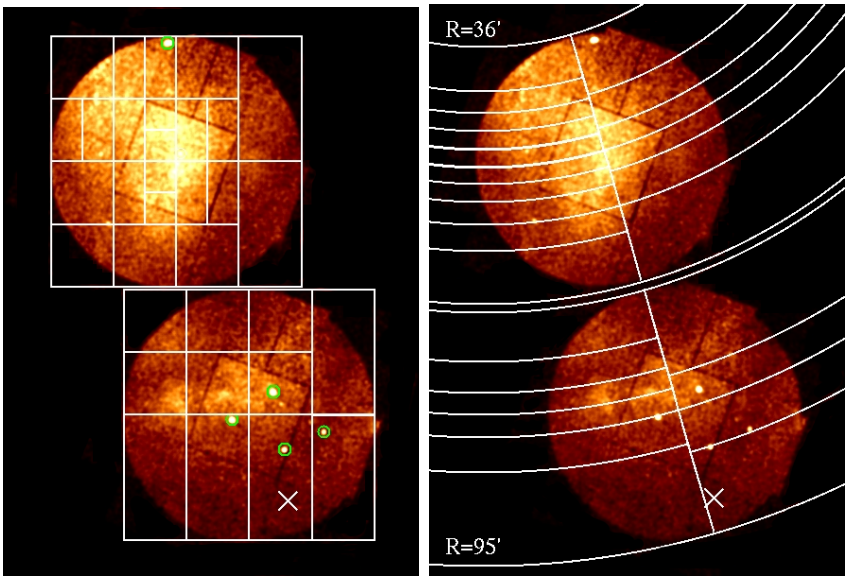


Figure 5.2: *Left*: *XMM-Newton* MOS broad-band image for the 0.3-3 keV range. White lines represents the spectral extraction regions. The green circles show the point-like source regions excluded from our spectral analysis. Two of the point sources in Pos-9 were observed by Miyata et al. (2001) and named AX J2049.6+2939 and AX J2050.0+2914, respectively. The white X shows the center of the G72.9-9.0 estimated by Uyaniker et al. (2002). *Right*: Same as the left panel, but for the different spectral extraction regions.

et al. 2008b). Also the metal abundances such as Si ($\sim 1.0$) and Fe ($\sim 0.4$) show about two times higher values than those of the northeast limb. These facts suggest that the X-ray emission in Pos-8 and Pos-9 mainly consists of the high-$kT_e$ component. However, the values of reduced $\chi^2$ are 6.9 and 3.6 in Pos-8 and Pos-9, respectively. The model is not enough to fit the data due to the simplicity of the model. Therefore, we intended to add the extra component to the VNEI model.

From the standpoint of the SNRs evolution, the X-ray emission from the SNRs have the two different origin. The blast wave from the supernova explosion sweeps the ambient medium, while the reverse shock propagates into the ejecta. Each shock wave heats up the swept-up ISM and the ejecta respectively. The shock-ISM interaction also produces the reflected shock which moves back through previously swept up ISM (Hester et al. 1994). Because of this, the X-ray spectra of the evolved SNR such as the Cygnus Loop should have a complicated structure. From the earlier observation of the northeast to the southwest regions, Tsunemi et al. (2007) proposed the plasma structure of the Cygnus Loop as follows: the high-$kT_e$ ejecta component is surrounded by the low-$kT_e$ ISM component. They found that the spectra from most regions of the Cygnus Loop

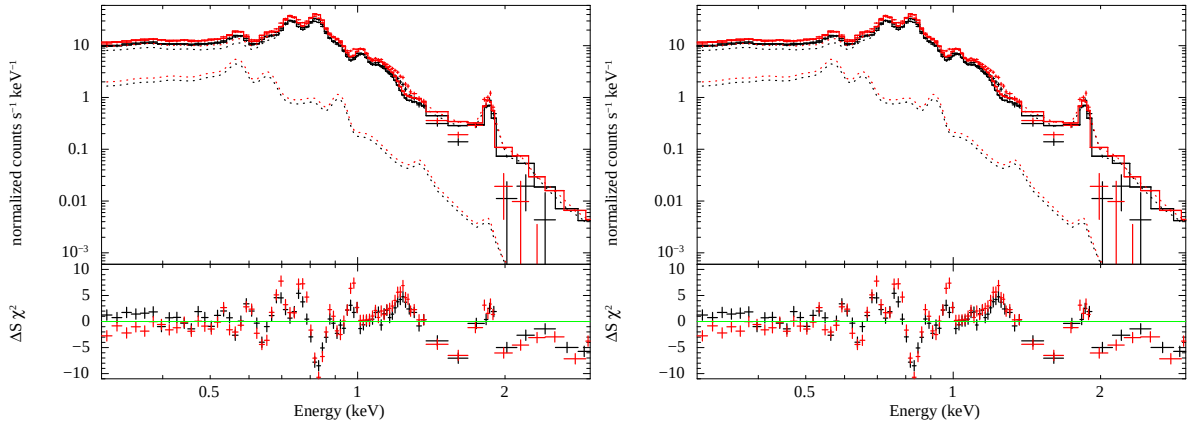


Figure 5.3: *Left*, MOS 1 (black) and MOS 2 (red) spectrum for Pos-8 which are summed over the entire FOV. The best-fit curves are shown as solid lines. The dotted lines show individual component of the model. The lower panel shows the residual. *Right*, same as the left panel, but for Pos-9.

consist of the two-component VNEI model. Thus we also employed two-component VNEI model which has two different electron temperatures. We found that this model cannot reach the physically meaningful results by setting all the parameters free. Therefore, in the low-$kT_e$ component, we fixed the metal abundances to the values from the northeast limb observations Tsunemi et al. (2007). Other parameters were set free such as $kT_e$, $\tau$, and EM. In the high-$kT_e$ component, we set all parameters to those of the single-$kT_e$ VNEI model as explained in the above paragraph. As a result, the values of the reduced $\chi^2$ remain almost unchanged: 6.9 to 6.5 and 3.6 to 3.4 in Pos-8 and Pos-9, respectively. These large values are due to the fact that we took the spectra summed over the entire FOV in which there is a lot of structure. Therefore we divided our FOV into several regions for the spectral analysis. Although we employed the constant temperature, plane-parallel shock plasma model, **vpshock** instead of **vnei**, the best-fit parameters were almost unchanged and the values of the reduced $\chi^2$ were not significantly improved.

### Spatially Resolved Spectral Analysis

From Figure 5.2, we can see a lot of structures within Pos-8 and Pos-9. For example, there is a region of high surface brightness at each center of Pos-8 and Pos-9 even after correcting the vignetting effect. We notice that they are different in color in Figure 5.1, which shows that the plasma temperatures are different from each region. In order to investigate the detail plasma structure, we divided our FOV into a number of box regions for the spectral analysis. To equalize the statistics, we determined the box sizes such that each region has 7,500-15,000 photons for MOS 1 and 2. In this way, we have 33 regions

(22 and 11 regions in Pos-8 and Pos-9, respectively). Figure 5.2 left panel shows the *XMM-Newton* MOS broad band image (0.3-3.0 keV) and box regions are shown in white lines.

To examine the plasma structure of Pos-8 and 9, we fitted 33 spectra extracted from box regions by the single-$kT_e$ VNEI model and two-$kT_e$ VNEI model, respectively. In the two-$kT_e$ VNEI model, we fixed the metal abundances of the low-$kT_e$ component to the result from the observations of the northeast rim as explained in Section 5.1.2. As in the case of the fit for each whole region, the values of the reduced $\chi^2$ are improved $\sim 1.6$ to $\sim 1.3$ and $\sim 1.4$ to $\sim 1.1$ in Pos-8 and 9, respectively. The F-test probability ($> 99\%$) shows that it is reasonable to add the extra low-$kT_e$ VNEI model in more than half of the regions. The best-fit parameters are shown in Figure 5.4 as the maps of the best-fit parameters. The averaged temperature of high- and low-$kT_e$ component are $\sim 0.4$ keV and $\sim 0.2$ keV, respectively. However, the low-$kT_e$ temperatures are determined only as the upper limit in several regions where the contribution of the low-$kT_e$ component is quite low as shown in the $EM_L$ map in Figure 5.4.

We compared these parameters and EMs of heavy elements with the results of Katsuda et al. (2008a). They observed the Cygnus Loop in seven pointings from the northeast to the southwest with *Suzaku* and showed the best-fit parameters using the two-$kT_e$ VNEI model. One of their observation regions (namely P16) is next to the northeast part of Pos-8 (see Figure 4.1). From the results of P16 observations, the temperature of the high-$kT_e$ and low-$kT_e$ component are 0.4 keV and 0.2 keV. These values are similar to our results. Katsuda et al. (2008a) concluded that the emission of the high-$kT_e$ component comes from the ejecta of the Cygnus Loop. Then we compared the EMs of O [=C=N], Ne, Mg, Si [=S], and Fe [=Ni] between in P16 and our FOV as shown in Table 5.1. Katsuda et al. (2008a) showed that each EM in their FOV reduces from the center to the outer region of the Loop. From Table 5.1, we found that this trend is also seen from P16 to our FOV.

Then, we determined the spectral extraction regions in different way to investigate the plasma structure from the inner side of the Loop to the outside.

We divided our FOV into two paths: the east path and west path. Then we divided several annular sectors as shown in Figure 5.2 right. To compare our analysis with that of Tsunemi et al. (2007), we set the annular center on $20^h51^m34.7^s, 31°00'00''$ (J2000). In order to equalize the statistics, we determined the annular widths such that each sector has at least $\sim 10,000 \pm 1,000$ photons. In this way, we have 26 annular sectors (16 and 10 sectors in the east and the west path, respectively) whose angular distances from the center are from $35'$ to $95'$. The width ranges from $1'$ to $6.5'$.

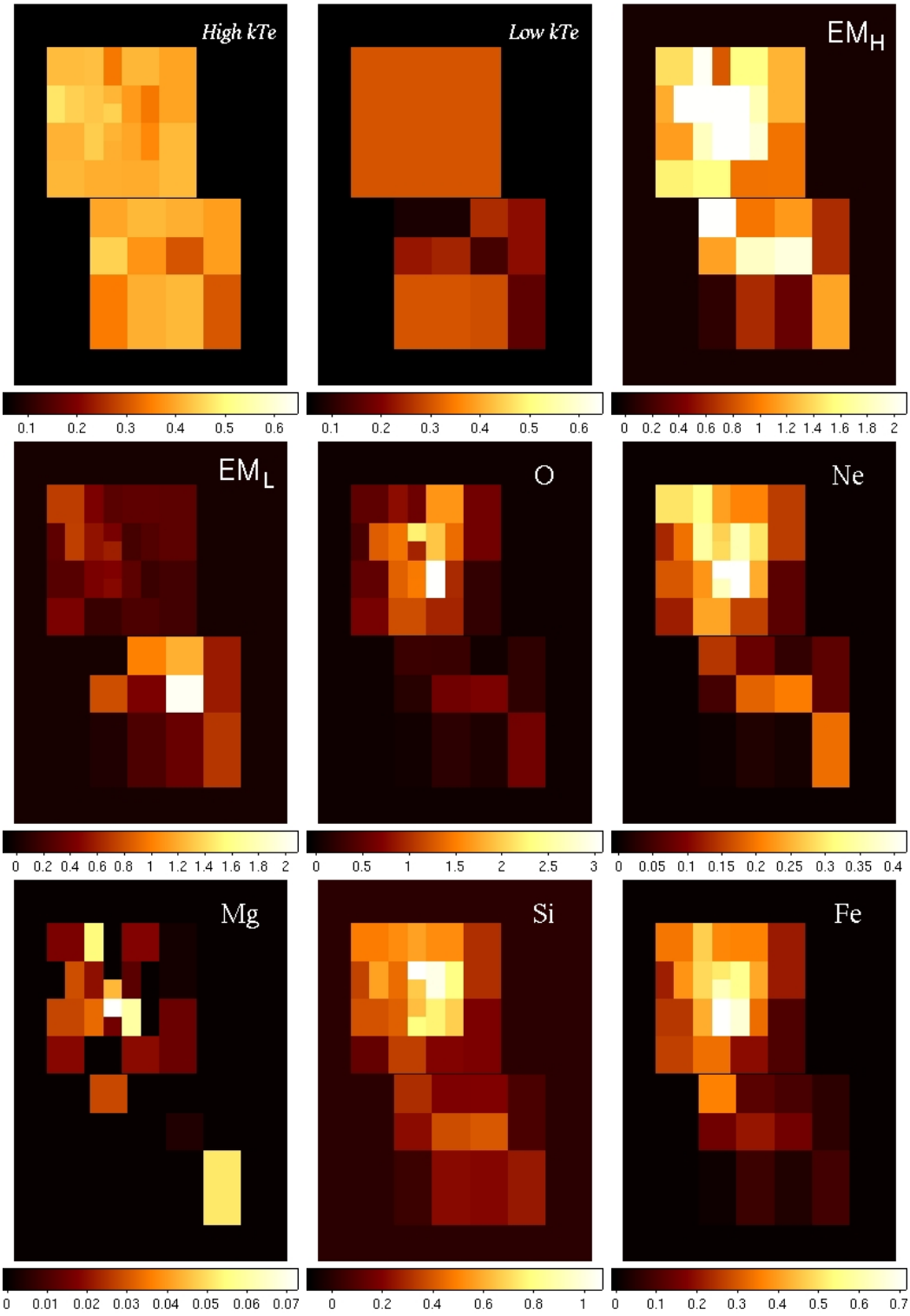


Figure 5.4: Maps of the best-fit parameters. $\mathrm{EM_H}$ and $\mathrm{EM_L}$ mean the emission measure of the high-$kT_e$ and low-$kT_e$ component, respectively. Last five panels show the EMs of O [=C=N], Ne, Mg, Si [=S], and Fe [=Ni] for the high-$kT_e$ component in units of $10^{14}\,\mathrm{cm}^{-5}$. The values of $kT_e$ and $\mathrm{EM}_{[H,L]}$ are in units of keV and $10^{18}\,\mathrm{cm}^{-5}$, respectively.

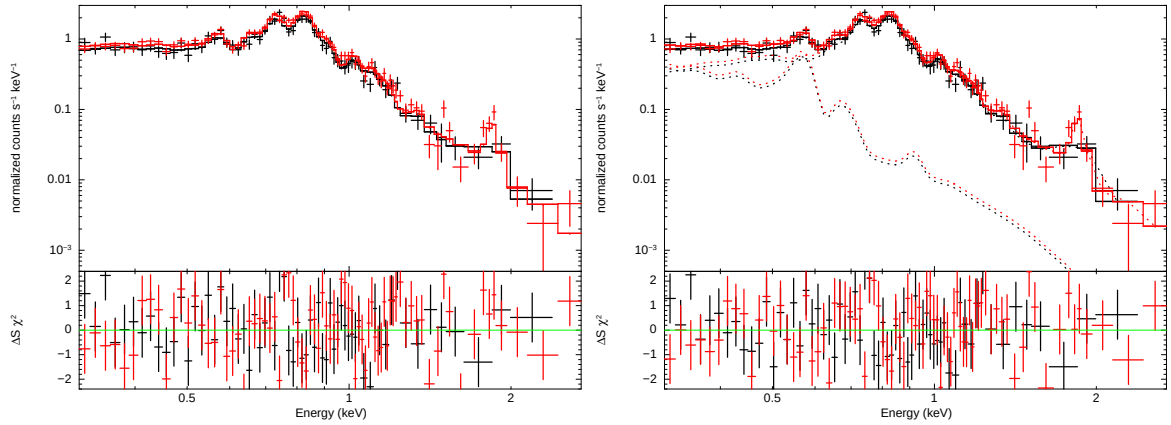


Figure 5.5: Example spectra at $R = 42.'5$. The solid line of each panel shows the best-fit curve with the single-$kT_e$ VNEI model and the two-$kT_e$ VNEI model, respectively. Each lower panel shows the residual. The dotted lines of the right panel show individual component of the two-$kT_e$ VNEI model.

Figure 5.5 shows the example of the spectrum from the sector at $R = 42'.5$, where $R$ represents the angular distance from the center. The left and right panels show the best-fit curves with the single- and the two-$kT_e$ VNEI model, respectively. The fitting parameters are set as explained in Section 5.1.2. Dotted lines in Figure 5.5 represent the individual model. From Figure 5.5 right, we found that the contribution of the low-$kT_e$ component is lower than that of the high-$kT_e$ component. The best-fit parameters are shown in Table 5.2 and 5.3, respectively. The F-test probability ($> 99\%$) shows that it is reasonable to add the extra low-$kT_e$ VNEI model in this sector.

Thus, we analysed all other sectors in the same way. Figure 5.6 shows the radial plot of the values of $\chi^2$ along the east path (top) and the west path (bottom). The single-$kT_e$ VNEI model is shown in black, while the two-$kT_e$ VNEI model is shown in red. From

Table 5.1: Comparison between the averaged EM for each element in our FOV and P16 (Katsuda et al. 2008a).

| EM of Each Element ($10^{14}$ cm$^{-5}$) | P16 | Pos-8 | Pos-9 |
|---|---|---|---|
| O(=C=N) | 4.2 | 1.2 | 0.28 |
| Ne | 0.42 | 0.25 | 0.09 |
| Mg | 0.04 | 0.02 | 0.01 |
| Si | 1.7 | 0.54 | 0.22 |
| Fe(=Ni) | 1.1 | 0.41 | 0.12 |

Table 5.2: Spectral Fit Parameters

| Parameter | Pos-8 |
|---|---|
| $N_H$ [$10^{20}$ cm$^{-2}$] | $4 \pm 1$ |
| $kT_e$ [keV] | $0.46 \pm 0.02$ |
| O(=C=N) | $0.04 \pm 0.01$ |
| Ne | $0.09 \pm 0.01$ |
| Mg | $0.04 \pm 0.02$ |
| Si | $0.79 \pm 0.16$ |
| Fe(=Ni) | $0.33 \pm 0.03$ |
| log $\tau$ | 10.58 |
| EM [$10^{18}$ cm$^{-5}$] | $2.54 \pm 0.56$ |
| $\chi^2$/dof | 187/133 |

the results, we calculated the F-test probability and determined whether or not the extra component is needed for each sector. Applying the significance level of 99%, the extra component is not required at $47'.5 < R < 75'.0$, and $77'.5 < R < 95'.0$ along the east path, and $36'.0 < R < 43'.0$, $47'.0 < R < 65'.0$, and $85'.0 < R < 95'.0$ along the west path. In other words, $\sim$ 60% of our FOV requires the two-$kT_e$ VNEI model. We find that the fit shown in Figure 5.5 (at $R = 42'.5$) is improved the most by using the two-$kT_e$ VNEI model. Even in this sector, the contribution of the additional low-$kT_e$ component is not so large.

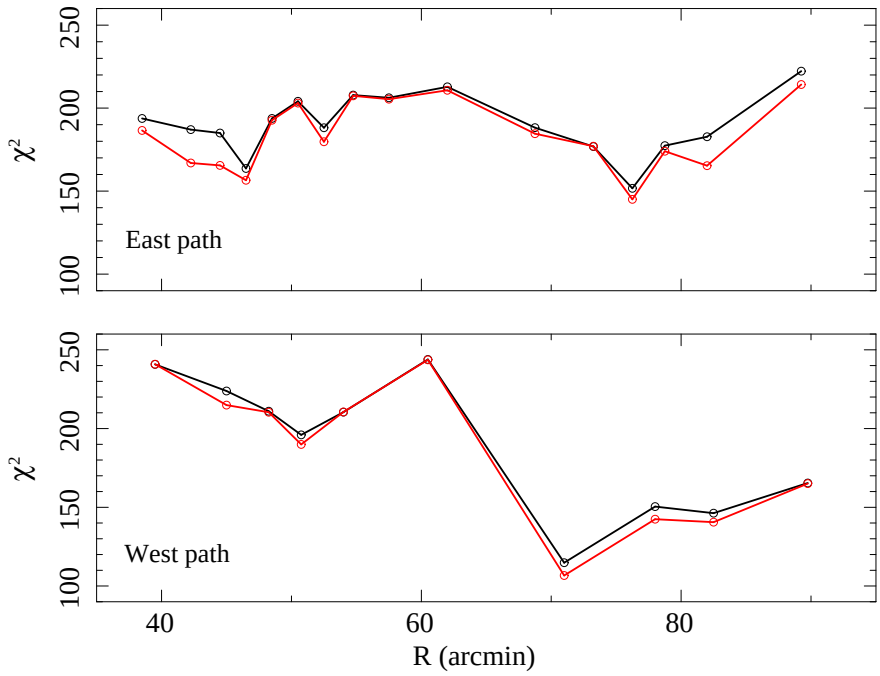


Figure 5.6: Radial plot of the values of $\chi^2$ as a function of $R$ along the east path (top) and the west path (bottom). The single-$kT_e$ and two-$kT_e$ VNEI model are shown in black and red, respectively. The degrees of freedom are all $\sim 130$.

Table 5.3: Spectral Fit Parameters

| Parameter | Value |
|---|---|
| $N_H$ [$10^{20}$ cm$^{-2}$] | $< 4$ |
| Low-$kT_e$ component: | |
| $kT_e$ [keV] | 0.26 ± 0.07 |
| C | 0.27 (fixed) |
| N | 0.10 (fixed) |
| O | 0.11 (fixed) |
| Ne | 0.21 (fixed) |
| Mg | 0.17 (fixed) |
| Si | 0.34 (fixed) |
| S | 0.17 (fixed) |
| Fe(=Ni) | 0.20 (fixed) |
| log $\tau$ | 10.62 |
| EM [$10^{18}$ cm$^{-5}$] | $< 0.57$ |
| High-$kT_e$ component: | |
| $kT_e$ [keV] | 0.47 ± 0.02 |
| O(=C=N) | 0.06 ± 0.02 |
| Ne | 0.08 ± 0.03 |
| Mg | 0.06 ± 0.03 |
| Si | 0.65 ± 0.14 |
| Fe(=Ni) | 0.42 ± 0.05 |
| log $\tau$ | 11.29 ± 0.03 |
| EM [$10^{18}$ cm$^{-5}$] | 1.88 ± 0.38 |
| $\chi^2$/dof | 167/130 |

### 5.1.3 Discussion

The first two panels of Figure 5.4 show the temperature distributions of the two components based on the analysis in Figure 5.2 left. Figure 5.7 shows the temperature distributions along the east path (top) and the west path (bottom) based on the analysis in Figure 5.2 right. Black and red represent the low-$kT_e$ temperature and the high-$kT_e$ temperature. From Figure 5.4 and 5.7, the averaged values of low-$kT_e$ and high-$kT_e$ temperature are $\sim$ 0.2 keV and $\sim$ 0.4 keV, respectively. In this way, we clearly separated the high-$kT_e$ component and the low-$kT_e$ component just as the observation obtained in Katsuda et al. (2008a) and Tsunemi et al. (2007). Tsunemi et al. (2007) showed the temperature of the low-$kT_e$ component is almost constant ($\sim$ 0.2 keV) along the diameter, while that of the high-$kT_e$ component is different in the northeast ($\sim$ 0.6 keV) and the southwest ($\sim$ 0.4 keV). Since our FOV is very close to southwest, our result shows smooth extrapolation from that of Tsunemi et al. (2007) in the southwest rather than that in the northeast.

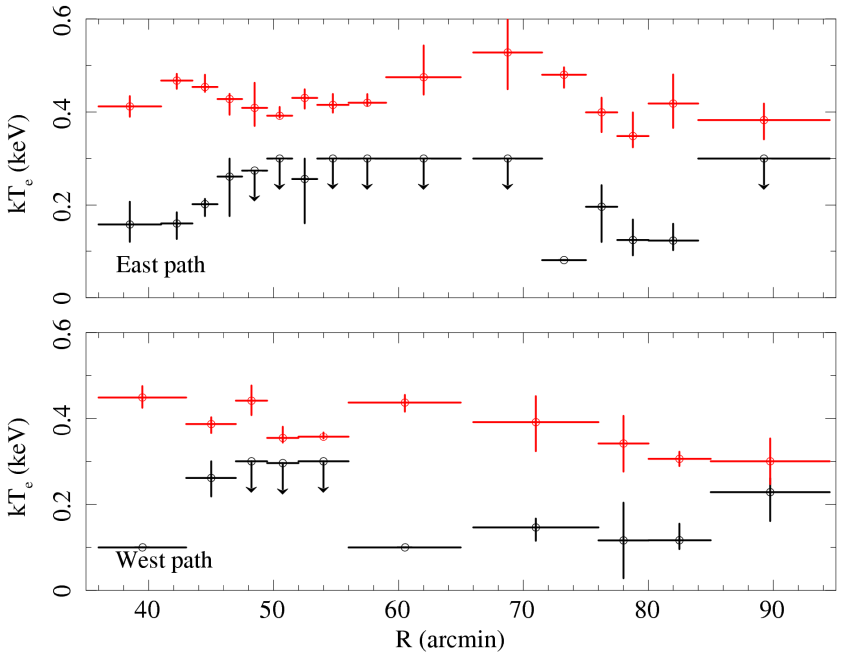


Figure 5.7: Temperature distributions of the two components as a function of $R$ along the east path (top) and the west path (bottom). Red shows the high-$kT_e$ component, while black shows the low-$kT_e$ component.

The third and fourth panels of Figure 5.4 shows the EM distributions for each component. Although there are some structures seen in the EM of the high-$kT_e$ component ($EM_H$) map, it is clear that the $EM_H$ is higher in Pos-8 than that in Pos-9. The EM of

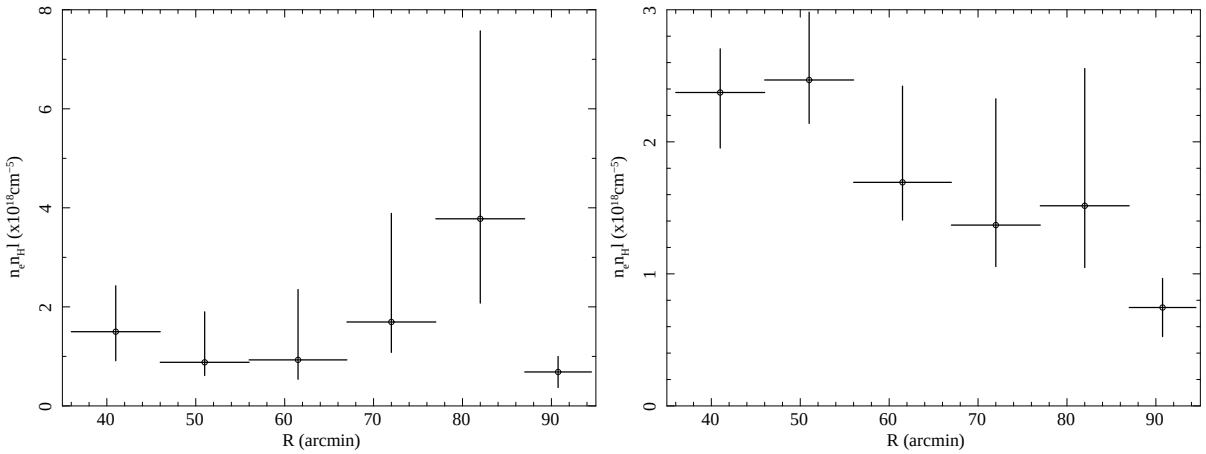


Figure 5.8: *Left*: $EM_L$ distribution as a function of $R$. *Right*: Same as the left, but for $EM_H$.

the low $kT_e$ component ($EM_L$) in all of our FOV are lower than those of $EM_H$. Figure 5.8 shows the radial profile of the EMs for each component. In this figure, we calculated the EMs as a function of $R$ into $10'$ bin. The $EM_L$ stays almost constant while it peaks around $R = 80'$. From the morphological point of view, the Cygnus Loop has an almost circular shape with a radius $\sim 80'$ except for the south "blowout". Then, it is suggested that the $EM_L$ distribution reflects the rim brightening structure around the "blowout" region. On the other hand, the value of $EM_H$ gradually decreases from the center to the outer region. This decrease can be easily explained by assuming that the emission comes from the ejecta component filling inside the Cygnus Loop. Then we also measured the EMs of various heavy elements in the high-$kT_e$ component such as O [=C=N], Ne, Mg, Si [=S], and Fe [=Ni] and compared them with the result of Tsunemi et al. (2007). Figure 5.9 shows the EM distribution for these elements as a function of $R$. We also plot the results of Pos-2 to 6 (Tsunemi et al. 2007) in the same panels. Although some structures are remaining in the annular regions as seen in Figure 5.2, the radial distribution of each EM clearly shows the smooth extrapolation of the results of Tsunemi et al. (2007). They showed the decrease of each EM from the center to the outer region and concluded that the high-$kT_e$ component is derived from the Cygnus Loop ejecta. It is reasonable to understand that the EMs in Pos-8 and 9 shows a smooth connection to those in their FOV. Therefore we concluded that the high-$kT_e$ component originates from the ejecta of the Cygnus Loop.

From the fitting parameters of the high-$kT_e$ component, we calculated the abundances of ejecta component for various elements. Figure 5.10 shows the abundance ratios of heavy elements (Ne: black, Mg: red, Si [=S]: green, Fe [=Ni]: red) relative to O. From Figure

5.10, we found that Si/O (∼20) and Fe/O (∼10) are heavily over abundant and Ne/O is ∼ 2, while Mg/O (< 1) is depleted. This tendency is kept throughout our observing region. The other observations of the ejecta in the Loop such as Tsunemi et al. (2007) and Katsuda et al. (2008a) showed the similar results.

Uyaniker et al. (2002) and Sun et al. (2006) reported that the Cygnus Loop consists of two SNRs interacting with each other in the southwest. Their main arguments are the difference of the radio morphology and the polarization intensity between the main part of the Cygnus Loop and the south "blowout" region. However, based on the X-ray data, we found that there is no evidence of the extra SNR within our FOV. If these SNRs are at the same distance as claimed by Uyaniker et al. (2002) and Sun et al. (2006), the smaller radius of the extra SNR, ∼7 pc $(R/\sim 0.7^\circ)(d/540\,\mathrm{pc})$, than that of the Cygnus Loop, ∼ 13 pc $(R/\sim 1.4^\circ)(d/540\,\mathrm{pc})$, strongly suggests that the extra SNR is younger than the Cygnus Loop is. If we employ the Sedov-Taylor solution, the temperature $T$ of the extra SNR is

$$T \sim 1.8\,\mathrm{keV}\left(\frac{\mathrm{E}_0}{10^{51}\,\mathrm{ergs}}\right)\left(\frac{n}{1\,\mathrm{cm}^{-3}}\right)^{-1}\left(\frac{R}{7\,\mathrm{pc}}\right)^{-3} \tag{5.1}$$

where $\mathrm{E}_0$ and $n$ are the explosion energy and the surrounding medium density of the extra SNR, respectively. Therefore, the temperature of the extra SNR should be significantly higher than that of the Cygnus Loop. However, we found no sign of such high temperature plasma. The spectra from all regions are almost represented by a single-$kT_e$ VNEI model (∼ 0.4 keV). If we add an extra component, we found in Section 5.1.2 that the extra component shows low temperature rather than high temperature. Furthermore, from Figure 5.7, the temperatures of each component are in good agreement with those obtained in other regions of the Loop (Tsunemi et al. 2007; Katsuda et al. 2008a). This result suggests that the X-ray emission from the southwest region mainly comes from the Cygnus Loop. If the secondary SNR exists in the sothwest at the same distance, the contribution of the X-ray emission to the spectra is much less than that of the Cygnus Loop. We cannot rule out the possibility that the extra SNR exists far side of the Cygnus Loop. However, even if that is the case, the fact remains that the spectrum from our FOV mainly consists of the ejecta and the ISM components of the Cygnus Loop. As a result, we find no evidence in X-ray that there exists the second SNR at the same distance to the Cygnus Loop.

Thus, we can estimate the mass of the progenitor star of the Cygnus Loop from the EMs of the high-$kT_e$ component, assuming that all these emissions come from the Loop. Then, we multiplied the EMs by the area of each annular sector and integrated the EMs along the path. In this way, we obtained the emission integral (EI $= \int n_e n_X dV$, where $dV$ is the X-ray-emitting volume) for O, Ne, Mg, Si, and Fe. Table 5.4 shows the calculated EI

Table 5.4: Calculated Emission Integrals ($= \int n_e n_X dV$) of the Cygnus Loop Ejecta

| | EI |
|---|---|
| Element | ($10^{52}\,\mathrm{cm}^{-3}$) |
| O | $1.34 \pm 0.20$ |
| Ne | $0.34 \pm 0.03$ |
| Mg | $0.02 \pm 0.01$ |
| Si | $1.02 \pm 0.10$ |
| Fe | $0.65 \pm 0.03$ |

of each element. To compare our data with the supernova explosion models, we calculated the ratios of Ne, Mg, Si and Fe relative to O. Figure 5.11 shows the number ratios of Ne, Mg, Si and Fe relative to O of the ejecta component. We also plotted the result from Tsunemi et al. (2007), the core-collapse models Woosley & Weaver (1995) for various progenitor masses and Type Ia supernova models Iwamoto et al. (1999) for comparison. The type Ia supernova yields more Fe than our results but less Ne. On the contrary, the number ratios of Si and Fe are higher than those of any core-collapse models, which attributes to the fact that our calculations are derived from the small part of the Cygnus Loop. These models were calculated under the assumption of the symmetric explosion. However, Tsunemi et al. (2007) and Katsuda et al. (2008a) reported the asymmetry of the metal distribution of the ejecta component: Si and Fe were more abundant, while Ne and Mg were less abundant in the southwest rather than that in the northeast. These results support an asymmetric explosion of the progenitor star. Our FOV is close to the southwest region in Tsunemi et al. (2007) rather than the northeast region. Taking into account the effect of the asymmetric structure, we support the idea that the Cygnus Loop originates from the core-collapse explosion rather than the Type Ia supernova.

### 5.1.4 Conclusion

We observed the southwest region of the Cygnus Loop with *XMM-Newton* . To examine the plasma structure, we divided our FOV in two different ways: 33 box sectors and 26 annular sectors. We fitted the spectrum extracted from each region with two-$kT_e$ VNEI model. The plasma structure of the low-$kT_e$ component and that of the high-$kT_e$ component are quite different from each other: each temperature is $\sim$0.2 keV and $\sim$0.4 keV for the former and the latter, respectively.

The EM distribution of the low-$kT_e$ component suggest the rim brightening structure,

while that of the high-$kT_e$ component monotonously decreases from the center of the Loop to the outside. In the high-$kT_e$ component, the abundances of Si and Fe are relatively high compared to those of Ne and Mg. The distributions of EMs as well as the relative abundances in the high-$kT_e$ component match the view that the low- and high-$kT_e$ components, respectively, originate from the ISM and the ejecta of the Cygnus Loop, which was derived by earlier observations such as Tsunemi et al. (2007) or Katsuda et al. (2008a). We found that the emission from this ISM component is relatively weak. This suggests that the thickness of the shell is thin in Pos-8 and Pos-9. We also calculated the relative abundances of Ne, Mg, Si, and Fe to O in the ejecta component for the entire FOV, and estimated the origin of the Cygnus Loop as the core-collapse explosion rather than the Type Ia supernova. We found no evidence in X-ray that the nature of the "blowout" region originated from the extra SNR.

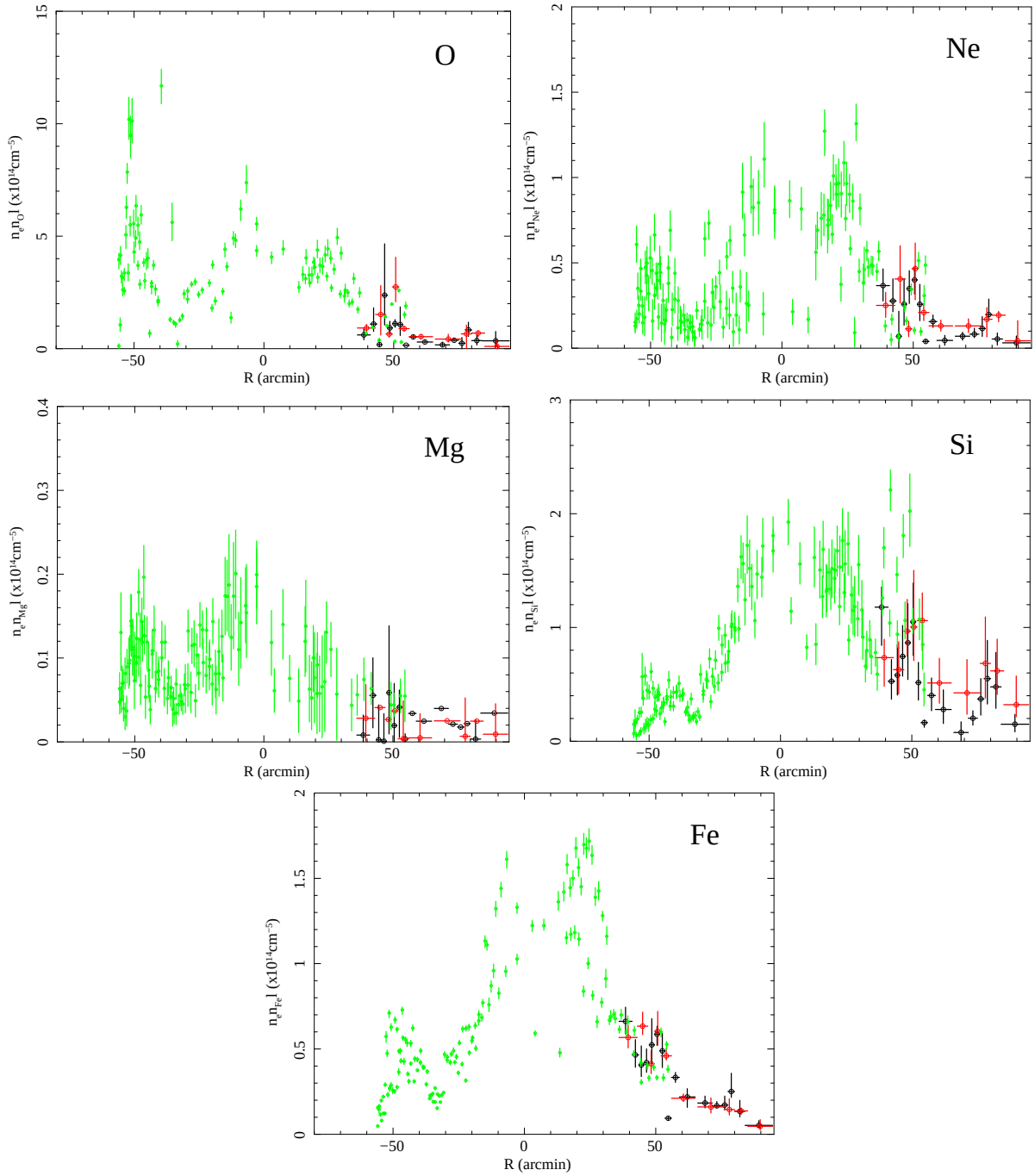


Figure 5.9: EM distributions for various metals (O [=C=N], Ne, Mg, Si [=S], and Fe [=Ni]) in the ejecta. Black and red show the west path and east path, respectively. Green shows the result of Tsunemi et al. (2007) taken from Pos-2 to Pos-6 (see Figure 4.1).

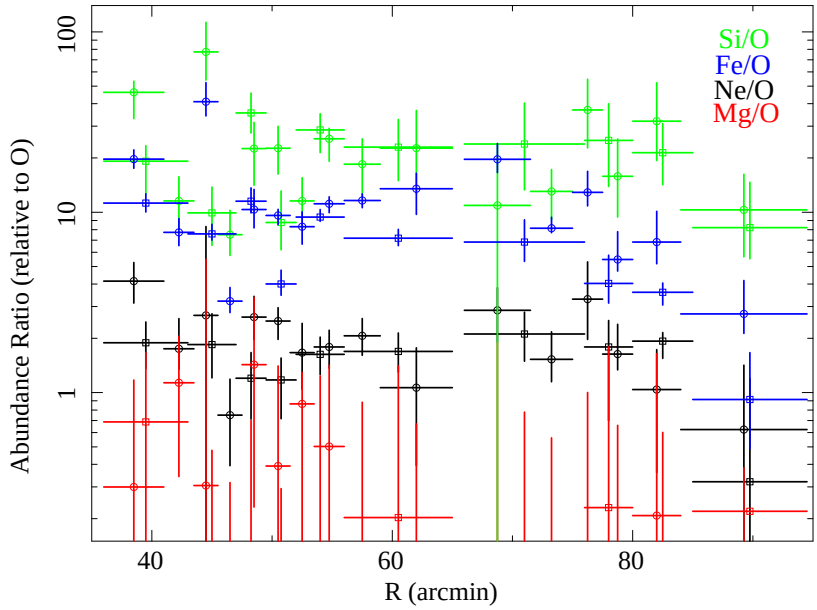


Figure 5.10: Distributions of relative abundance of heavy elements to O are shown as a function of $R$. Si/O, Fe/O, Ne/O, and Mg/O are shown in green, blue, black, and red, respectively. The results of east path and those of west path are plotted in the same color.

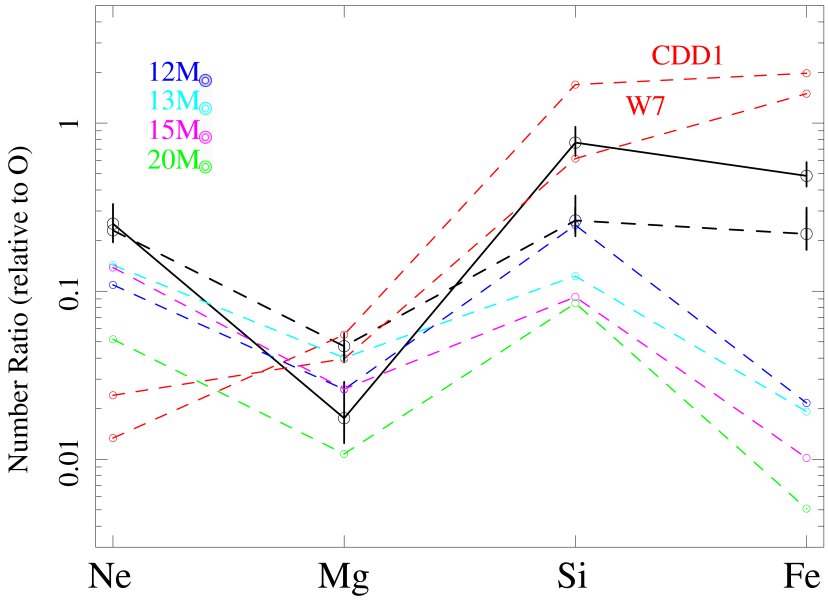


Figure 5.11: Number ratios of Ne, Mg, Si, and Fe relative to O of the high-$kT_e$ component, estimated for the entire Loop (solid line). Dotted and solid black lines show the result of Tsunemi et al. (2007) and that from our FOV. Dotted red lines represent the CDD1 and W7 Type Ia supernova models of Iwamoto et al. (1999). Dotted blue, light blue, magenta, and green lines represent core-collapse models with progenitor masses of 12, 13, 15, 20$M_\odot$ , respectively (Woosley & Weaver 1995).

## 5.2 Abundance-enhanced Region

Section 5.1 investigated the origin of the blowout region and we concluded that there exists a large break of the cavity wall in the south. In this section, we show the abundance inhomogeneity in the northern limb and discuss about the possibility of other breakouts of the cavity wall.

Section 5.2 is based on the results of Uchida et al. (2009a).

### 5.2.1 Observations

We observed the northern limb of the Cygnus Loop with *Suzaku* in 5 pointings (P21, P22, P23, P24, and P25; see Table 4.2). Their FOV are shown in Figure 5.12 left panel with the white solid squares. We also show the FOV of the other limb observations with the white dotted squares: four pointings of the northeastern limb (NE1-NE4; Katsuda et al. 2008b) and a southwestern limb observation (P27; Tsunemi et al. 2009). We intended to expand our observation westward from NE1-NE4 along the limb. We note that the FOV of P21 is next to that of NE4.

### 5.2.2 Spectral Analysis

Figure 5.12 right shows the three-color X-ray image for P21-P25 using *Suzaku* XIS data after correcting for exposure and vignetting effects. Red, green and blue correspond to the energy ranges of 0.3-0.5 keV, 0.5-1.0 keV and 1.0-3.0 keV, respectively. To investigate the plasma structure of the northern limb of the Loop, we divided our FOV into several box regions as shown in Figure 5.12 right middle. In order to equalize the statistics, we initially divided all images of XIS1 into two parts and if each divided region has more than 10,000 photons, it was once again divided. In this way, we obtained 115 box regions. Each region contains 5,000-10,000 photons for XIS1. The side length of each box ranges from $2'.3$ to $9'.0$. Therefore, box sizes are not smaller than the angular resolution capability of the *Suzaku* XIS. We grouped 115 spectra into bins with a minimum of 20 counts so that $\chi^2$ statistics is appropriate.

We first applied an absorbed single-$kT_e$ component of VNEI model for all the spectra. We employed **TBabs** (Tübingen-Boulder ISM absorption model; Wilms et al. 2000) and in XSPEC version 12.4.0. In this model, the abundances of C, N, O, Ne, Mg, Si and Fe were free while we set the relative abundances of S to the solar value (Anders & Grevesse 1989) equal to that of Si, Ni equal to Fe. Other elements were fixed to their solar values. Other parameters were all free such as the electron temperature $kT_e$, the

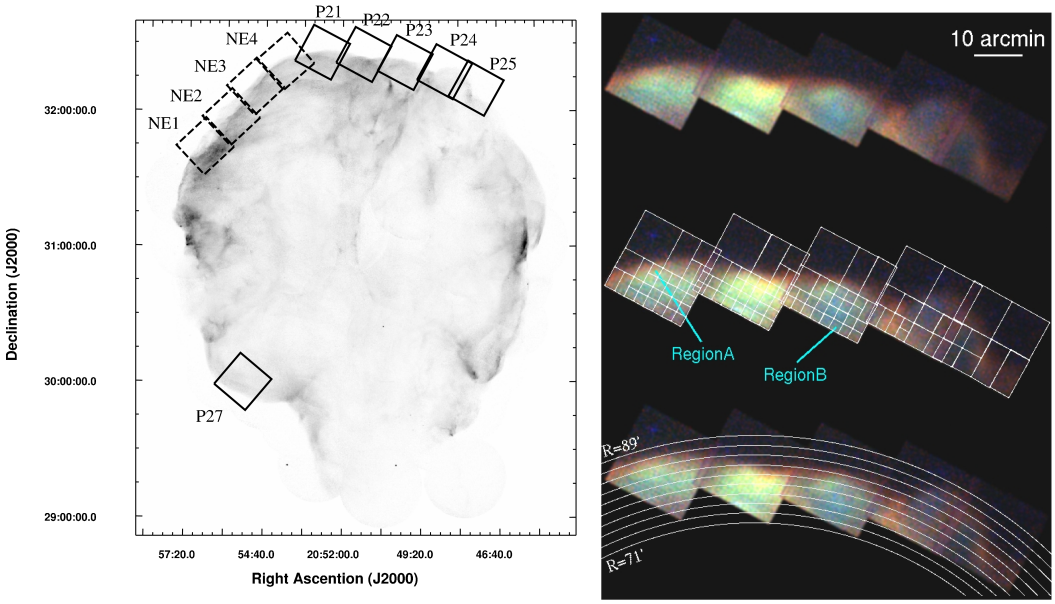


Figure 5.12: *Left*: *ROSAT* HRI image of the entire Cygnus Loop. The *Suzaku* FOV are shown with white rectangles. The dotted and solid lines represent the past and our observations, respectively. *Right top*: Three-color X-ray image for P21-P25 using XIS data. Red, green and blue correspond to the energy ranges of 0.3-0.5 keV, 0.5-1.0 keV and 1.0-3.0 keV, respectively. *Right middle*: Same as the right top panel, but for overlaid with the spectral extraction regions with white rectangles. *Right bottom*: Same as the right middle panel, but for the different spectral extraction regions.

ionization timescale $\tau$, and the emission measure (EM). We also set the column density $N_{\rm H}$ free. The spectra are reasonably well fitted by the single-$kT_e$ VNEI model for almost all regions. The values of the reduced $\chi^2$ show around 1.5 and the degrees of freedom (dof) are 300-400. We also fitted all the spectra with the two-$kT_e$ VNEI model in which the values of the abundances and $\tau$ were tied in two components. This model was applied for the northeast limb observations in Miyata et al. (2007) and Katsuda et al. (2008b). However, this model does not improve the values of $\chi^2$ for almost all regions and the best-fit parameters are consistent with those obtained from the single-$kT_e$ VNEI model. Therefore, we concentrate on the results of the single-$kT_e$ VNEI model in what follows.

The example spectra and the best-fit curves are shown in Figure 5.13. The best-fit parameters are shown in Table 5.5. We also show the spectral extracted regions in Figure 5.12 right middle. These two spectra are taken from the regions where N, O and Ne are relatively abundant (region-A) and depleted (region-B). From Figure 5.13, we can clearly see the difference in the feature of each spectrum: the spectra obtained from region-B

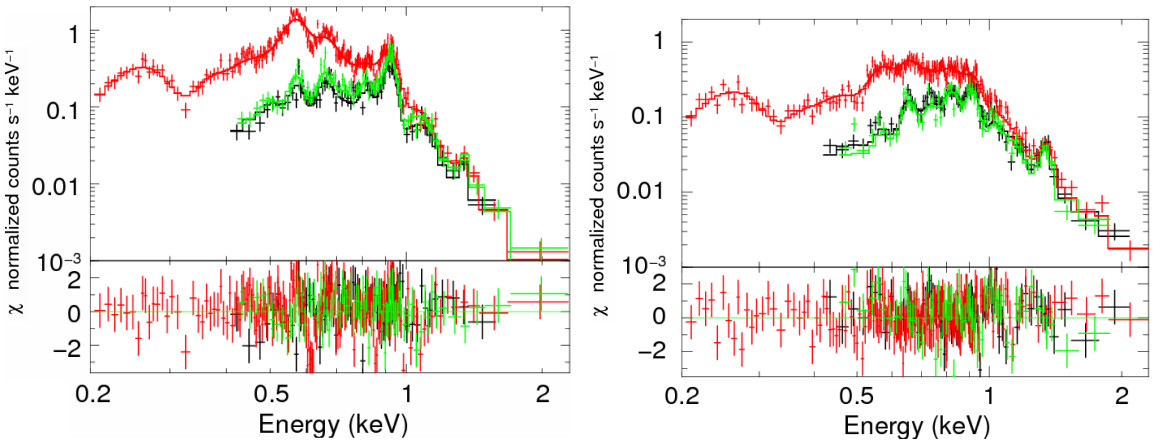


Figure 5.13: Example spectra from the regions where N, O and Ne are abundant (region-A: left) and depleted (region-B: right), respectively. The best-fit curves are shown with solid line. The residuals are shown in the lower panels. Black, red, green correspond to the XIS 0, 1, 3, respectively.

is smoother than that from region-A and the line emissions of some elements such as N, O and Ne are prominent in region-A. The best-fit parameters in Table 5.5 support these differences statistically. The abundances of N, O and Ne are significantly higher in region-A than those in region-B. Figure 5.14 shows the maps of the best-fit parameters obtained from all 115 spectra. The images are smoothed by Gaussian kernel of $\sigma = 1'.5$. The color code scale is normalized by the maximum values. From Figure 5.14, the values of $kT_e$ distribute around 0.3 keV and those in the inner region of P23 are higher than the other parts of our FOV. The values of $\log(\tau)$ are higher in the west than those in the east and spread between 10.5-11.5. Some elements such as N, O and Ne are particularly abundant in the outer edge of the limb in P21-P22 while they seem to be depleted inward. These results suggest that the abundances of these elements have radial dependencies. Then, we determined the spectral extraction regions in different way to investigate the plasma structure from the inner side to the outer edge of the limb.

As shown in Figure 5.12 right bottom, we divided our FOV into several annular sectors. We set the center of the annular regions to the "geometric center" estimated by Levenson et al. (1998). It is located on $\alpha$ =$20^{\rm h}51^{\rm m}21^{\rm s}$, $\delta$ =$31°01'37''$, determined by fitting the *ROSAT* HRI map of the Cygnus Loop by the model circle. We set the annular width to $2'$ which is restricted by the angular resolution capability of the *Suzaku* XIS. The distance from the geometric center ranges from $72'$ to $88'$. In this way, we have totally 36 annular sectors from 5 observations. Figure 5.15 shows two examples of the spectra from P21. One is extracted from the outer edge of the limb ($R$=$88'$, where $R$ represents the

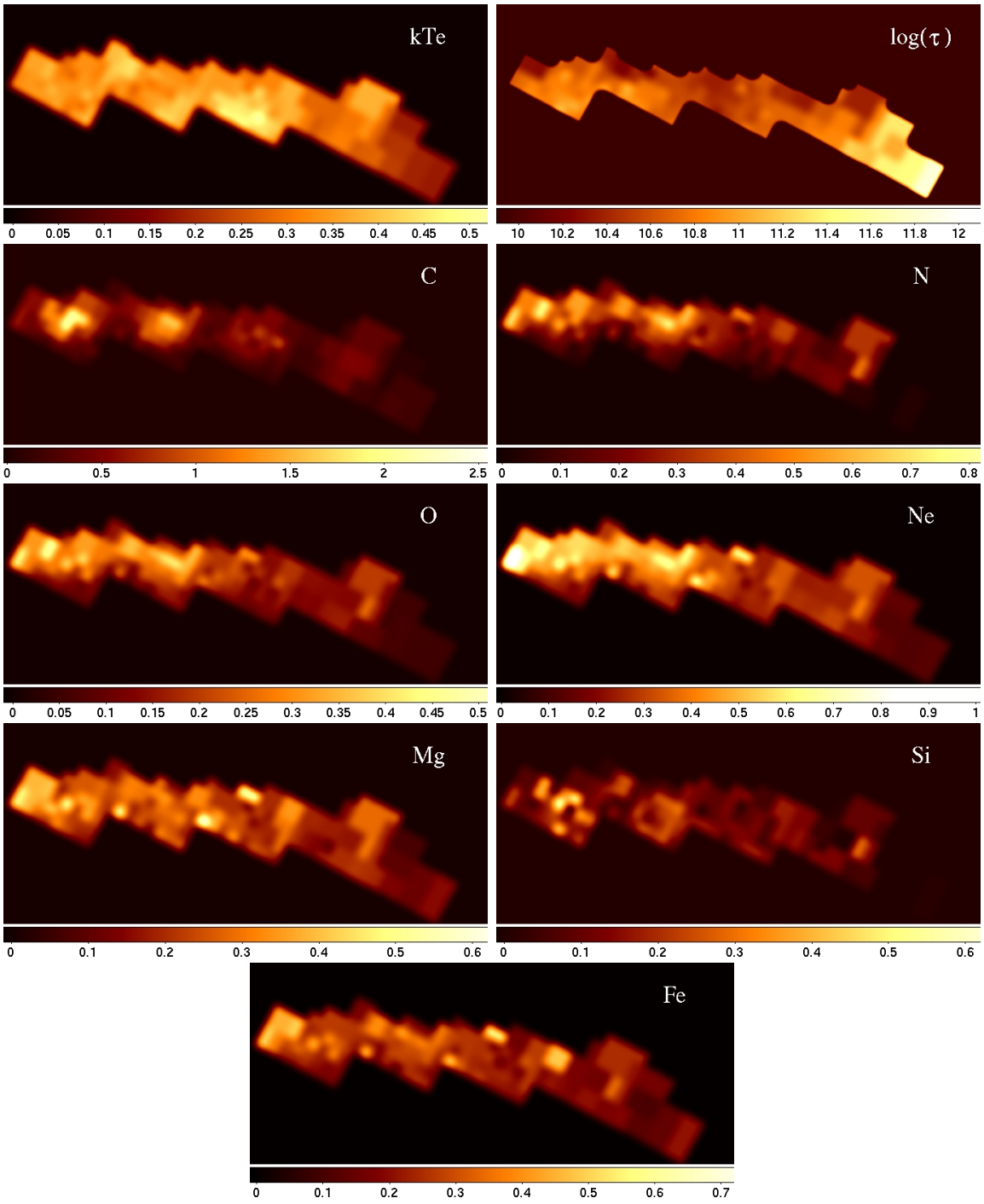


Figure 5.14: Maps of the best-fit values for various parameters. The value of $kT_e$ is in units of keV.

Table 5.5: Spectral fit parameters

| Parameter | region-A (VNEI) | region-B (VNEI) |
|---|---|---|
| $N_H$ [$10^{20}$ cm$^{-2}$] | $1.0 \pm 0.1$ | $1.0 \pm 0.1$ |
| $kT_e$ [keV] | $0.32\ ^{+0.04}_{-0.07}$ | $0.43\ ^{+0.04}_{-0.05}$ |
| C | $0.81\ ^{+2.79}_{-0.43}$ | $0.18\ ^{+0.16}_{-0.13}$ |
| N | $0.61\ ^{+0.72}_{-0.45}$ | $< 0.06$ |
| O | $0.45\ ^{+1.03}_{-0.26}$ | $0.10\ ^{+0.03}_{-0.02}$ |
| Ne | $1.04\ ^{+2.03}_{-0.64}$ | $0.24\ ^{+0.06}_{-0.04}$ |
| Mg | $0.56 \pm 0.18$ | $0.25\ ^{+0.08}_{-0.06}$ |
| Si (=S) | $< 0.17$ | $0.18\ ^{+0.12}_{-0.10}$ |
| Fe (=Ni) | $0.58\ ^{+0.83}_{-0.39}$ | $0.21\ ^{+0.05}_{-0.03}$ |
| $\log(\tau)$ | $10.52\ ^{+0.37}_{-0.07}$ | $10.79\ ^{+0.37}_{-0.14}$ |
| EM [$10^{20}$cm$^{-5}$] | $0.24 \pm 0.01$ | $0.23 \pm 0.09$ |
| $\chi^2$/dof | 672/437 | 398/322 |

angular distance from the center) and the other, extracted from the inner region ($R$=76′). As is the case in Figure 5.13, the emission lines of N, O, and Ne appear more in the outer region ($R$=88′) than those in the inner one ($R$=76′). The best-fit curves and the best-fit parameters with the single-$kT_e$ VNEI model are shown in Figure 5.15 and Table 5.6, respectively. From Table 5.6, we found that the abundances of some elements such as N, O, Ne, Mg and Fe are significantly higher at $R$=88′ than those at $R$=76′. Figure 5.16 and 5.17 shows the radial plot of the best-fit parameters, $kT_e$, $\log(\tau)$, and abundances of various elements as a function of $R$. We found that the abundances of N, O, and Ne increase toward the outer edge of the limb only in P21-P22. This result is consistent with that of figure 5.14.

### 5.2.3 Discussion and Conclusion

#### Abundance depletion at the limb of the Cygnus Loop

Miyata et al. (1994) observed the northeastern limb of the Loop (overlapping with the NE2 region) with *ASCA* and found the deficient metal abundances there (typically $\sim 0.1$ times solar). Miyata et al. (2007) confirmed it with the *Suzaku* satellite. The abundance depletion is also seen at the other side of the Loop (Leahy 2004). Leahy (2004) observed southwestern limb of the Loop with *Chandra* and showed that the abundance of the O-group (C, N and O) is depleted about twice as that of the Ne-group (Ne, Mg, Al, Si, S

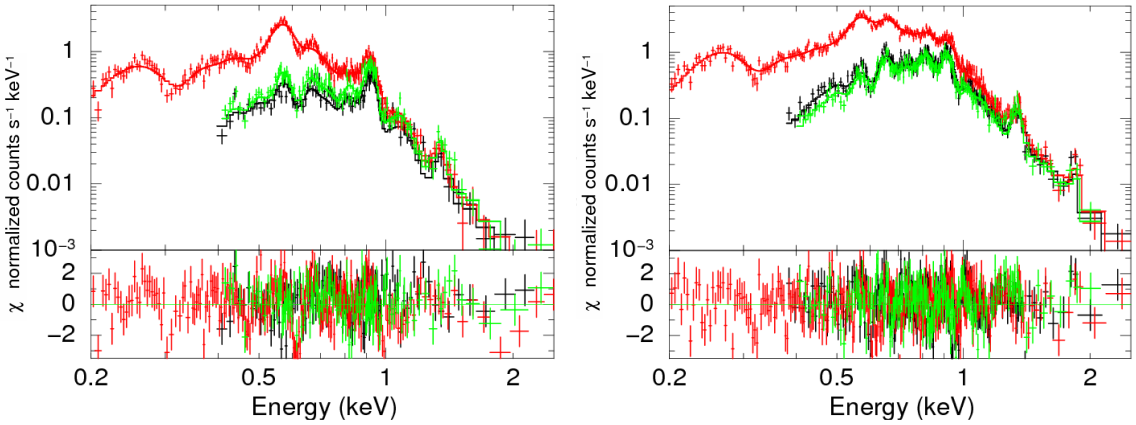


Figure 5.15: Example spectra extracted from the outer edge of the limb ($R$=88′) and the inner region ($R$=76′). The best-fit curves are shown with solid line. The residuals are shown in the lower panels. Black, red, green correspond to the XIS 0, 1, 3, respectively.

and Ar) and the Fe-group (Ca, Fe and Ni). He showed the O-group abundance to be 0.22 times the solar value. Likewise, several other X-ray studies reported such low metal abundances (Miyata et al. 1998; Miyata & Tsunemi 1999; Tsunemi et al. 2007; Nemes et al. 2008; Katsuda et al. 2008b,c; Tsunemi et al. 2009). It seems to be a common result at the limb of the Cygnus Loop. Our result confirmed this trend at the northern limb of the Loop, except the outermost part of P21-P22 (e.g., see Figure 5.14).

Cartledge et al. (2004) observed the O and H absorption line and measured the interstellar O along 36 sight lines. The results indicate that the O/H ratio is homogeneous within 800pc of the sun and that the O abundance is $\sim$ 0.4 times the solar value. Since the Cygnus Loop is located at 540pc of the sun, the O abundance is expected to be that of the interstellar medium (ISM). The past observations do not show such values and it is not clear why the O abundance and the other elemental abundances are all deficient at the limb of the Loop.

Raymond et al. (2003) studied the effect of the resonance-scattering for the O VI emission from the FUV observations in the northeastern limb of the Cygnus Loop. Miyata et al. (2008) proposed that the effect of the resonance-line-scattering optical depth lowers the apparent abundances of some elements on the basis of the NE2 observation. They calculated the optical depths in their FOV for some K emission lines (C VI K$\alpha$, N VI K$\alpha$, O VII K$\alpha$, O VIII Ly$\alpha$, and Ne IX K$\alpha$) and concluded that the optical depth effects play a significant role in the X-ray emission lines, particularly those of O. They calculated that the O abundance is underestimated by a factor of 20-40% in the northeastern limb where

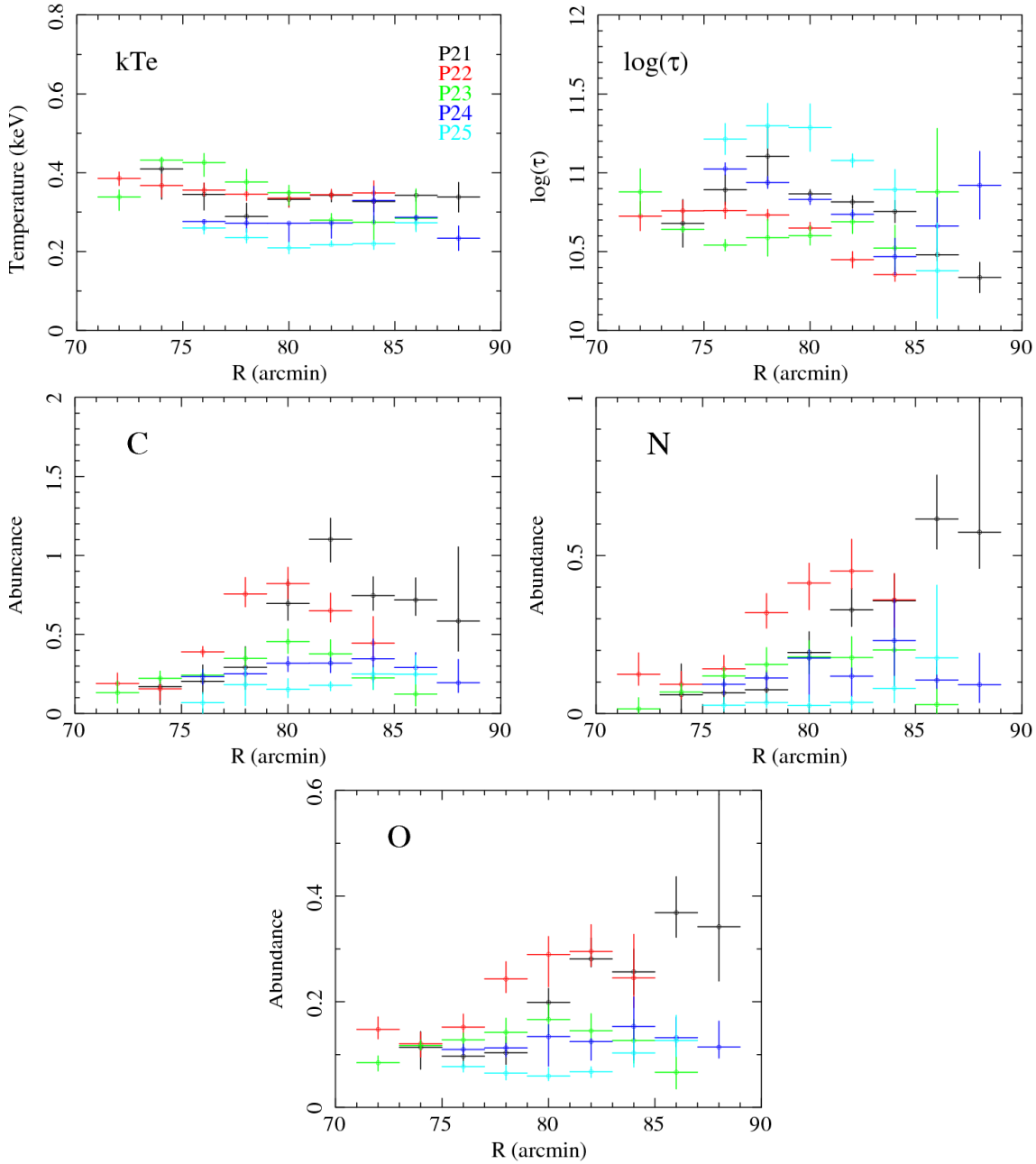


Figure 5.16: Radial plot of $kT_e$, $\log(\tau)$, and abundances of C, N, and O as a function of $R$. Black, red, green, blue and light blue correspond to P21, P22, P23, P24 and P25, respectively.

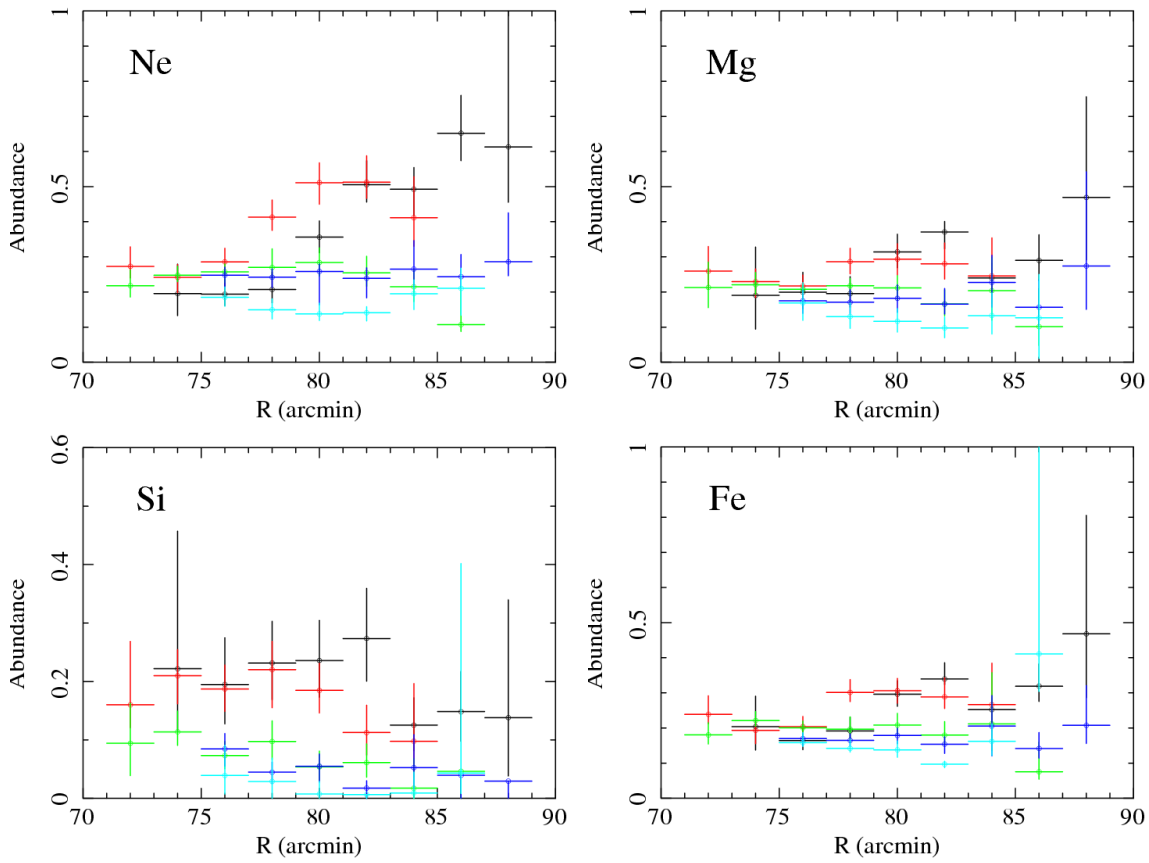


Figure 5.17: Same as Figure 5.16, but for the abundances of Ne, Mg, Si, and Fe.

Table 5.6: Spectral fit parameters

| Parameter | $R$=88′ (VNEI) | $R$=76′ (VNEI) |
|---|---|---|
| $N_H$ [$10^{20}$ cm$^{-2}$] | $1.3\ ^{+0.7}_{-0.6}$ | $2.6\ ^{+0.7}_{-1.0}$ |
| $kT_e$ [keV] | $0.34 \pm 0.04$ | $0.29\ ^{+0.03}_{-0.02}$ |
| C | $0.58\ ^{+0.19}_{-0.47}$ | $0.29 \pm 0.13$ |
| N | $0.57\ ^{+0.52}_{-0.12}$ | $0.08\ ^{+0.06}_{-0.04}$ |
| O | $0.34\ ^{+0.25}_{-0.10}$ | $0.10\ ^{+0.03}_{-0.02}$ |
| Ne | $0.61\ ^{+0.40}_{-0.16}$ | $0.21\ ^{+0.05}_{-0.04}$ |
| Mg | $0.47\ ^{+0.29}_{-0.18}$ | $0.20\ ^{+0.05}_{-0.04}$ |
| Si (=S) | $0.14\ ^{+0.20}_{-0.10}$ | $0.23\ ^{+0.07}_{-0.06}$ |
| Fe (=Ni) | $0.47\ ^{+0.34}_{-0.18}$ | $0.19\ ^{+0.04}_{-0.03}$ |
| $\log(\tau)$ | $10.34\ ^{+0.16}_{-0.09}$ | $11.10\ ^{+0.10}_{-0.19}$ |
| EM [$10^{20}$ cm$^{-5}$] | $0.26 \pm 0.01$ | $3.05 \pm 0.06$ |
| $\chi^2$/dof | 671/448 | 963/640 |

the O emission is the highest in the Cygnus Loop. However, it is not sufficient to account for the abundance depletion in the northeastern limb. The resonance-line-scattering effect depends linearly on the column density, the product of the density and the plasma depth. We here assume that the Cygnus Loop is spherical symmetric and the filling factor in the shell region is unity. Then, the plasma depths in the northeastern limb and our FOV are the same with each other, since these regions are located at about the same radii. Therefore, the resonance-line-scattering effect depends only on the density which in this case squarerootly depends on the EM or the surface brightness. Since the surface brightness in our FOV is lower than that in the northeastern limb, the resonance-line-scattering effect should be even less significant in our FOV than that in the northeastern limb. Therefore, we can conclude that the effect of the resonance-line-scattering is not sufficient enough to account for the abundance depletion observed in our FOV.

The other possibility is the effect of the circumstellar grain. In general, the grain condensation depletes the abundance of the heavy elements such as C, O, Mg, Si and Fe (Savage & Sembach 1996). The cavity wall is considered to be an ISM material pushed into a shell by the stellar wind and radiation while the progenitor was on the main sequence. There is a possibility that the ISM grains were destroyed by shocks as the shell expanded (Vancura et al. 1994) and that the condition of the abundance of grain influences the values of the metal abundances. However, this model does not explain the depletion of rare gasses such as Ne and it remains unclear why the metal abundances

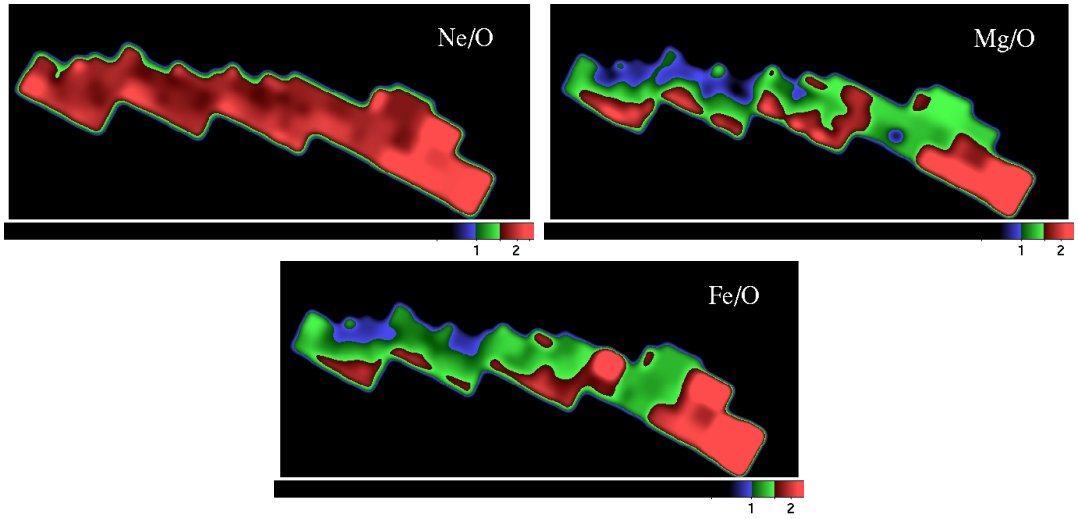


Figure 5.18: Distributions of the relative abundances of Ne/O, Mg/O and Fe/O. Red, green and blue represent the regions where the relative abundance show more than 1.5, from 1 to 1.5, and less than 1, respectively.

show low values almost everywhere in the cavity wall.

### Abundance-enhanced region at the outermost edge of the Cygnus Loop

On the other hand, some recent observations revealed that the limited regions show high abundances (Katsuda et al. 2008b; Tsunemi et al. 2009). Katsuda et al. (2008b) analyzed the *Suzaku* data of the northeastern limb (NE1-NE4) and found that the abundances of the heavy elements have relatively high values (C$\sim$ 0.7, N$\sim$ 0.7, O$\sim$ 0.4, Ne$\sim$ 0.6, Mg$\sim$ 0.3, and Fe$\sim$ 0.3) only at the outermost edge in NE3-NE4, while the other regions show relatively depleted abundances. They also showed the abundance ratios of Mg/O and Fe/O are lower in the abundance-enhanced region than those in the other regions. Katsuda et al. (2008c) made an additional observation with *Chandra* and confirmed these results. The abundance-enhanced region is about $30' \times 3'$ with relatively weak surface brightness. Tsunemi et al. (2009) observed the southeastern limb (P27) with *Suzaku* and showed that the similar abundance-enhanced regions are seen in their FOV (C$\sim$ 0.6, N$\sim$ 0.9, O$\sim$ 0.4, Ne$\sim$ 0.7, Mg$\sim$ 0.5, and Fe$\sim$ 0.5). The width of the abundance-enhanced region is $\sim 3'$. It is striking that these regions are both located at the outermost edges of the limbs, while the inner regions usually show the metal deficient abundances like the other limb observations.

Our FOV is next to that of Katsuda et al. (2008b). From figures 5.14, 5.16, and 5.17, we found that the abundances of N, O and Ne are relatively high at the outermost

edge in P21-P22. It continues into the abundance-enhanced region in NE3-NE4 and these values of abundances are similar to each other. In addition, as shown by Katsuda et al. (2008b) in NE3-NE4, low abundance ratios ($< 1$) of Mg/O and Fe/O are also seen at the abundance-enhanced region in our FOV. Figure 5.18 shows the distributions of the ratios of Mg/O and Fe/O in our FOV. For comparison, we also show the Ne/O map in the same figure. Red, green and blue represent the regions where the relative abundances show more than 1.5, from 1 to 1.5, and less than 1, respectively. From figure 5.18, the values of the Ne/O are more than 1.5 times higher than the solar values for all regions. On the contrary, the Mg/O and the Fe/O are both lower than the solar values at the abundance-enhanced regions in P21-P22. In view of these facts, it is natural to consider that the abundance-enhanced regions in NE3-NE4 and P21-P22 have the similar origin.

Katsuda et al. (2008c) presumed that the abundance inhomogeneity in NE3-NE4 is due to the break of the cavity wall of the Loop. Falle & Gralick (1982) and Shull & Hippelein (1991) both argue for an incomplete cavity of the Cygnus Loop, and the former also makes the case that the north part of the Loop is a very large scale breakout. In that case, NE3-NE4 and our regions observed entirely should have normal ISM abundances. However, Levenson et al. (1997) and Levenson et al. (1998) presented the spherical-cavity model and in that case, the blast wave where a small breakout exists could overrun the cavity wall and proceed first into the surrounding ISM with the ISM metallicity. Thus, the abundances there could reflect the values of the ISM abundance. Although the Cygnus Loop is almost circular in shape, some observations show that the thickness of the cavity wall is not uniform. Kimura et al. (2009) observed northern region of the Loop from northeast to southwest with the *Suzaku* satellite and revealed that the swept-up matter shell is very thin in just the west of center of the Loop. They estimated the diameter of this thin shell region to be 1° and concluded that the breakout exists along the line of sight. We can also see such breakout in the south of the Loop called the "blowout" region (Aschenbach & Leahy 1999). From the X-ray observation with *XMM-Newton* , Uchida et al. (2008) showed that the X-ray shell is thin in the blowout region and concluded that the origin of the blowout can be explained as a breakout into a lower density ISM (Section 5.1). These results suggest that the ambient density of the Loop is not uniform while the Loop seems to be spherical symmetry. The abundance-enhanced regions previously observed have relatively weak surface brightnesses in X-ray (see figure 5.12). As Levenson et al. (1999) point out, the bright soft X-ray emission can result from a slower shock speed in denser cavity material. Conversely, the weak surface brightness at the abundance-enhanced regions observed suggest that the breakout or the thin cavity wall exists there.

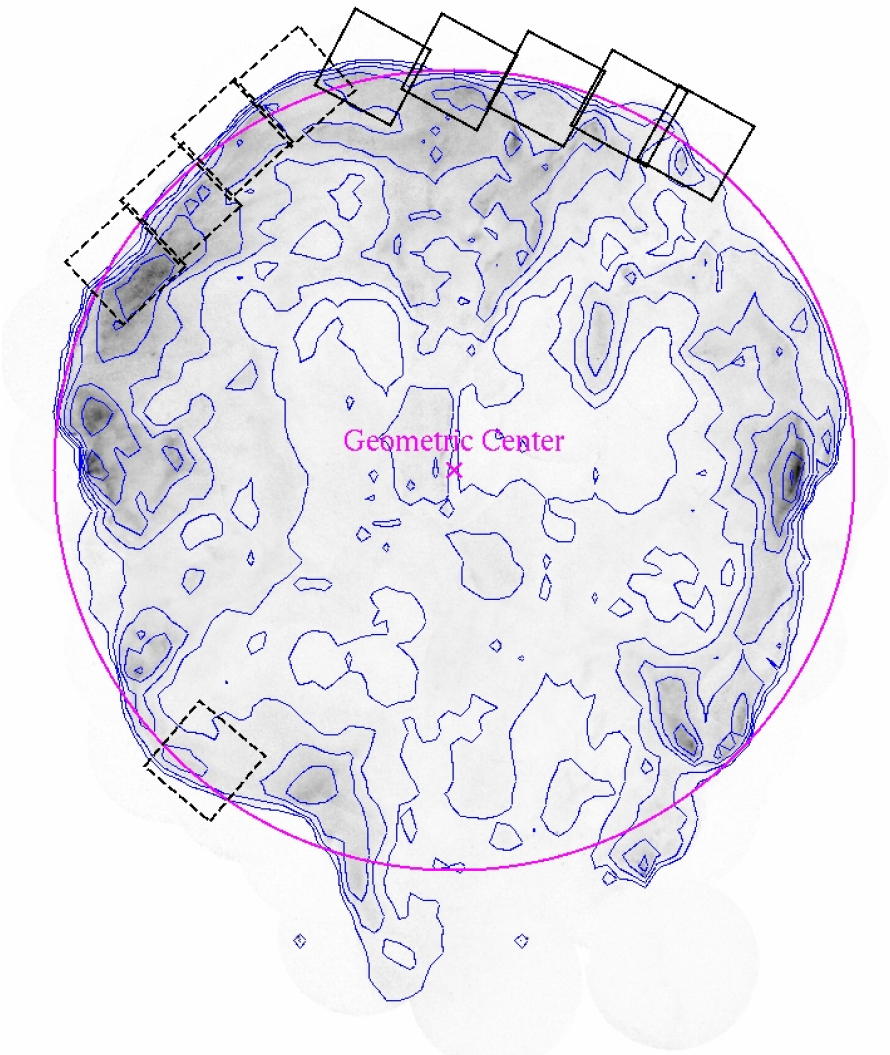


Figure 5.19: *ROSAT* HRI image of the entire Cygnus Loop and its contour (blue line) overlaid with our FOV (black solid line) and those of Katsuda et al. (2008b) and Tsunemi et al. (2009) (dotted line). The geometric center and a circle with radius $\sim 1^{\circ}.4$ are shown by the magenta lines.

We also confirmed it from the morphological point of view. Figure 5.19 shows the *ROSAT* HRI image of the entire Cygnus Loop and its contour (blue line). The geometric center and a circle with radius $\sim 1^{\circ}.4$ are shown by the magenta lines. From Figure 5.19, there are three outwardly-projecting shell regions where the limbs are over the magenta circle, except the large south blowout: a part of the northeastern limb (NE3 to P21), northestern limb (P24 and P25), and the southwestern limb (P27). Under the assumption that the supernova explosion occurred at the geometric center, the cavity walls toward these directions are considered to be thinner than those toward the other ones. Among these projecting shell regions, the northeastern and the southeastern limbs clearly show the abundance-enhanced regions from previous (NE3-NE4, P27) and our observations (P21-P22). It is reasonable to consider that the abundance inhomogeneities in these regions are derived from the breakout or the thinness of the cavity wall. As for the northwestern limb, the abundances there show low values compared with those at the edges of the northeastern or the southeastern limbs (see Figure 5.14). However, even in this region, the abundances such as N , O and Ne at the outer edge are slightly higher than those at the inner region. This fact suggests that the outer edge of the northwestern limb shows the sign of the abundance-enhancement as is the case with those of the northeastern and the southeastern limbs. Then, we concluded that the blast wave in the northwest is now proceeding into the outside of the cavity wall and begins to interact with the surrounding ISM.

We speculate that there are many breaks of the cavity wall in the Cygnus Loop where the abundances show the values of the ISM. However, the spectra at these regions should be observed as the superpositions of those with the depleted abundances in the line of sight. Therefore, the abundance-enhanced regions where we can observe are limited at the outer edges of the Loop.

## 5.3 Line-of-sight Shell Structure

Previous section suggested that some breakouts or thin cavity walls exist at the north-eastern limb regions of the Cygnus Loop as well as the south blowout region (Section 5.1). In this section, we present a method to investigate the line-of-sight shell structure of the Cygnus Loop and the comprehensive study of the shell structure of the Cygnus Loop.

Section 5.3 is based on the results of Uchida et al. (2009b).

### 5.3.1 Observations

We used 32 and 9 pointings observation data obtained by the *Suzaku* and the *XMM-Newton* observatories in order to reanalyze all the data to conduct a comprehensive study on the shell structure of the Cygnus Loop. The observing regions are shown in Figure 5.20 top. The circles and rectangles represent the FOV of the *XMM-Newton* MOS and the *Suzaku* XIS, respectively. The summaries of 41 observations are shown in Table 4.1 and 4.2.

### 5.3.2 Spectral Analysis

To investigate the plasma structure of the Cygnus Loop, we divided the entire FOV into small box regions. In order to equalize the statistics, we initially divided all images of XIS1 or MOS2 into two parts; if each divided region had more than 10,000 photons, it was once again divided. In this way, we obtained 1042 box regions. The spectral extracted regions are shown in Figure 5.20. Each region contained 5,000-10,000 photons for XIS1 and MOS2. The side length of each box ranges from $2.2'$ to $14'$. Therefore box sizes are not smaller than the angular resolution capability of the *Suzaku* XIS. We grouped 1042 spectra into bins with a minimum of 20 counts such that $\chi^2$ statistics are appropriate.

Firstly, we fitted all the spectra by a single-component VNEI model. We employed **TBabs** and **VNEI** in XSPEC version 12.5.0. In this model, the abundances for C, N, O, Ne, Mg, Si and Fe were free, while we set the relative abundances for S to the solar value equal to that of Si, Ni equal to Fe. The other elements were fixed to their solar values. Other parameters were all free such as the electron temperature, $kT_e$, the ionization timescale, $\tau$, and the emission measure, EM. We also set the absorption column density, $N_{\rm H}$, to be free. As a result, the spectra from the limb regions are well fitted by the single-component VNEI model. As shown by earlier observations of the northeast and the southeast limb (Tsunemi et al. 2007; Kimura et al. 2009; Uchida et al. 2009a; Tsunemi et al. 2009), the spectra obtained from the limb regions of the Cygnus Loop

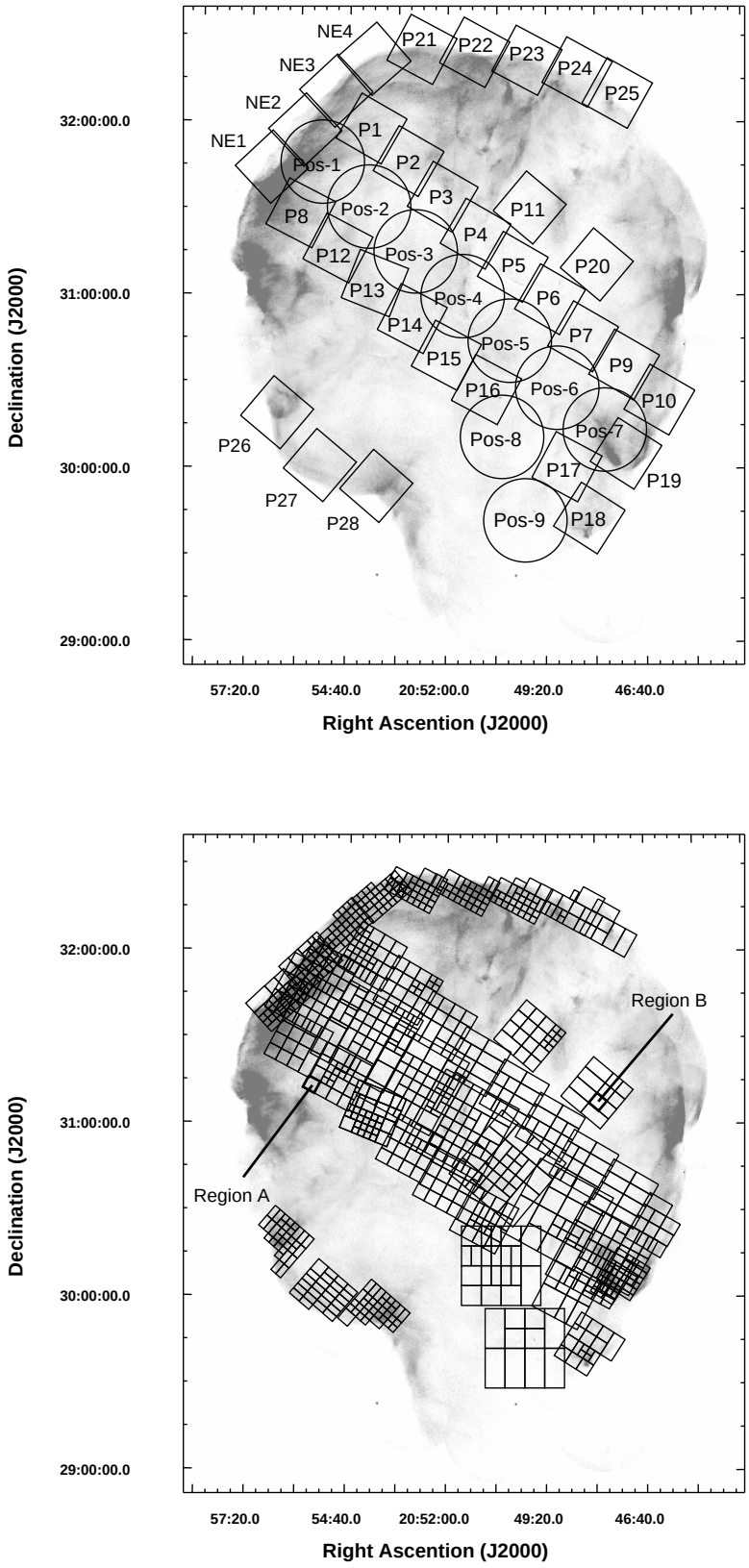


Figure 5.20: *Top*: *ROSAT* HRI image of the entire Cygnus Loop. The circles and rectangles represent our FOV of the *XMM-Newton* MOS and the *Suzaku* XIS, respectively. *Bottom*: Same as the left panel, but for overlaid with the spectral extraction regions with small rectangles.

are typically described by a single-component VNEI model.

On the other hand, the spectra from the inner regions are generally not fitted by the single-component VNEI model. From earlier observations of the northeast to the southwest regions along the diameter, Tsunemi et al. (2007) found that the spectra from the inner regions of the Cygnus Loop consist of a two-component VNEI plasma. They concluded the plasma structure of the Cygnus Loop as follows: the high-$kT_e$ ejecta component is surrounded by a low-$kT_e$ ISM component. Uchida et al. (2009c) showed that the two-component VNEI model is wholly applicable to the inner regions of the Cygnus Loop. Therefore, we next intended to give an additional high-$kT_e$ VNEI component to the single-component VNEI model. In this model, we fixed the metal abundances of the low-$kT_e$ component to the values obtained from the result of Tsunemi et al. (2007), since the model whose abundances set all free could not obtain the physically meaningful results. Tsunemi et al. (2007) showed the relative abundances to the solar values of the ISM component as follows: C=0.27, N=0.10, O=0.11, Ne=0.21, Mg=0.17, Si=0.34, S=0.17, Fe(=Ni)=0.20. In addition, they fixed other elements to the solar values (Anders & Grevesse 1989). Meanwhile, in the high-$kT_e$ component, the abundances for O, Ne, Mg, Si, and Fe were free, while we set the abundances for C and N equal to O, S equal to Si, Ni equal to Fe. Other elements were fixed to their solar values. The other parameters such as $kT_e$, $\tau$, EM, and $N_{\rm H}$ were all free. We applied both single-component VNEI model and two-component VNEI model to all the spectra and determined which model is acceptable by using the F-test with a significance level of 99%. As a result, roughly $< 0.80R_{\rm s}$ of the northeast region and $< 0.85R_{\rm s}$ of the southwest region need an additional component, where $R_{\rm s}$ is a shock radius. Here, we define the "limb observations" as the regions where the single-component VNEI model is acceptable and the "inside observations" as the remaining regions.

Figure 5.21 shows two example XIS1 spectra. The spectral extracted regions are shown in Figure 5.20. Both regions are located at the inside observations and the two-component VNEI model is applicable. The bottom two panels show the best-fit results of the two-component VNEI model. Blue and red lines represent the high-$kT_e$ and the low-$kT_e$ component. We also show the result with the single-component VNEI model at the top two panels for comparison. The best-fit parameters are shown in Table 5.7. These results show that the reduced $\chi^2$ values are significantly improved with the two-component VNEI models.

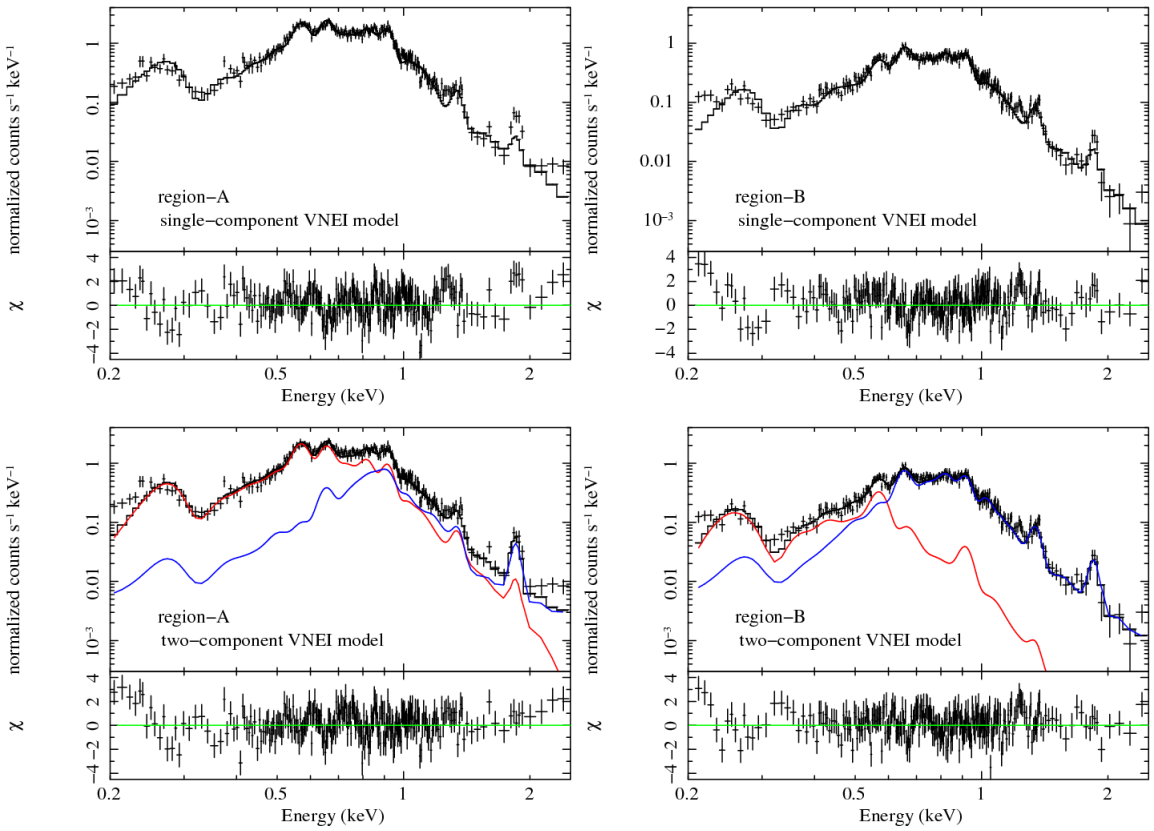


Figure 5.21: Example XIS1 spectra from the regions where the flux of the swept-up matter is high (region-A: left two panels) and low (region-B: right two panels), respectively (see figure5.20). The best-fit curves for the single-component VNEI models are shown by solid black lines in the top two panels. Bottom two panels are the same as the top panels, but for the fitting results with the two-component VNEI models. In the bottom panels, blue and red lines represent the high-$kT_e$ component and the low-$kT_e$ component, respectively. The residuals are shown in lower panels.

### 5.3.3 Discussion

#### Temperature distribution of the low-$kT_e$ component

All the spectra are well fitted by either the single-component VNEI model or the two-component VNEI model. From the best-fit parameters of the inside observations, we found that the electron temperature of the low-$kT_e$ component is almost uniform. The averaged value is 0.23 keV ($\sigma = 0.08$ keV) and it is sufficiently lower than that of the high-$kT_e$ component (0.52 keV, $\sigma = 0.17$ keV). The temperature of the low-$kT_e$ component is close to that of the limb observations (0.29 keV, $\sigma = 0.07$ keV). Therefore we collectively call these components "low-$kT_e$ component" hereafter.

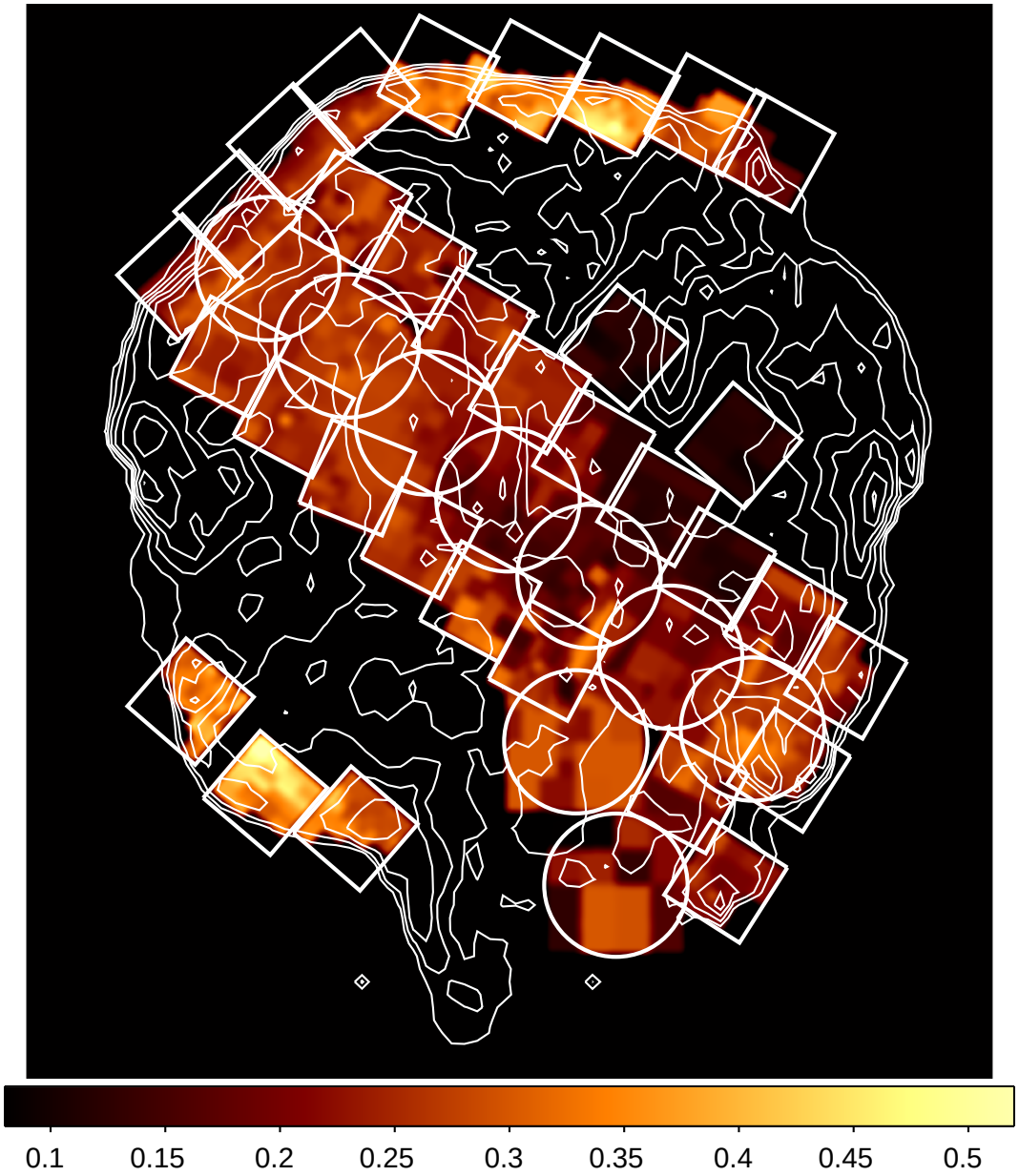


Figure 5.22: Our FOV and the electron temperature distribution of the low-$kT_e$ component overlaid with the white contour from the *ROSAT* HRI image. The images are smoothed by Gaussian kernel of $\sigma = 2.8'$. The values are in units of keV.

Figure 5.22 shows our FOV and the electron temperature distribution of the low-$kT_e$ component overlaid with the white contour from the *ROSAT* HRI image. The averaged value is $\sim 0.28$ keV and it ranges from 0.12 keV to 0.35 keV. Meanwhile, the temperature of the high-$kT_e$ component ranges from 0.4 keV to 0.9 keV, which is consistent with the previous observations (Tsunemi et al. 2007; Katsuda et al. 2008a; Kimura et al. 2009; Uchida et al. 2009c). Then, we confirmed that the temperature of each component is clearly separated. Uchida et al. (2009c) also showed that the temperature distribution of the high-$kT_e$ component is not uniform and that it is lower in the southwest part than that in the northeast part. On the other hand, the temperature of the low-$kT_e$ component is relatively uniform (see Figure 5.22). The detailed distribution shows the temperature near the center is lower than that of the surroundings. We also found that the temperature distribution is seamless at the boundary between the limb observations and the inside observations. Therefore, the low-$kT_e$ components of these regions must have the same origin. The spectra from the limb observations are obviously swept-up ISM origin, and thus, we concluded that any low-$kT_e$ component originates from the ISM component.

**Line-of-sight Shell Structure of the Cygnus Loop**

Taking into account the age of the Cygnus Loop the reverse shocks should have already reached its center. Therefore, on the assumption that the density of the ejecta-origin plasma is homogeneous, the X-ray flux depends exclusively on its plasma depth. In Figure 5.21, the blue line represents the high-$kT_e$ component of the two-component VNEI model. Since the region-A and the region-B are located at the same radial distance from the center ($R \sim 50'$, where we define $R$ as a distance from the "geometric center" determined by Levenson et al. 1998), they should have almost the same plasma depths. Accordingly, the fluxes of the high-$kT_e$ components are actually not so different, while the spectral extracted regions are separated. Meanwhile, the contributions of the low-$kT_e$ components are quite different as shown with the red lines in Figure 5.21. From the bottom left panel of Figure 5.21, the flux of the low-$kT_e$ component in the region-A overwhelms that of the high-$kT_e$ component at 0.2-1.0 keV. On the other hand, the contribution of the low-$kT_e$ component in the region-B is clearly smaller than that in the region-A. Such a difference should be attributed to the difference of the surrounding shell of each region. The value of the flux is proportional to EM ($\propto n_{\rm H}^2 l$), which means that the surface brightness is sensitive to the change of the density and the plasma depth there.

In order to estimate the ambient density of the Cygnus Loop, we calculated the fluxes of the low-$kT_e$ component from all regions. Figure 5.23 left shows the 0.2-3.0 keV flux distribution of the low-$kT_e$ component. We also show that of the high-$kT_e$ component

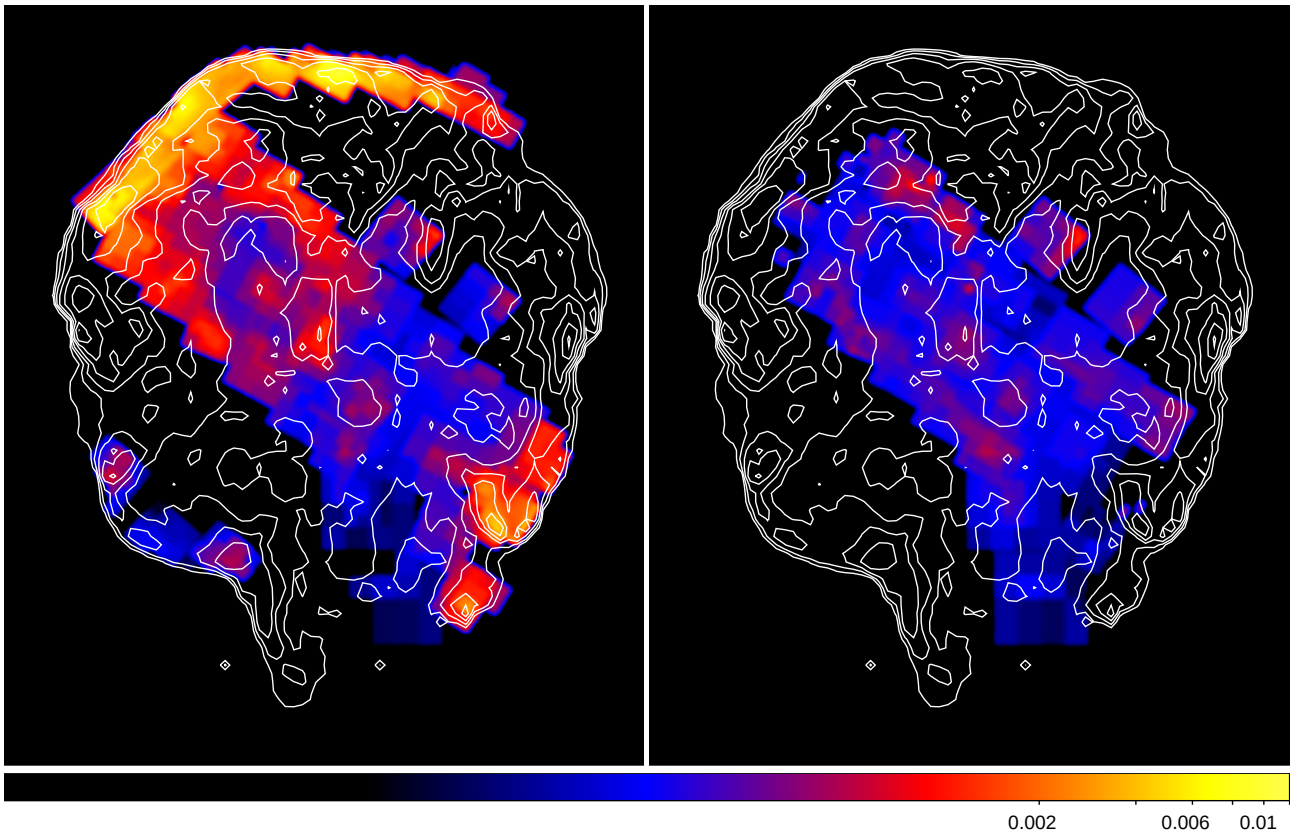


Figure 5.23: 0.2-3.0 keV flux distribution of the low-$kT_e$ (left) and the high-$kT_e$ (right) component in logarithmic scales overlaid with the white contour of the *ROSAT* HRI image. The images are smoothed by Gaussian kernel of $\sigma = 2.8'$. The values are in units of counts $\mathrm{cm}^{-2}\mathrm{s}^{-1}\mathrm{arcmin}^{-2}$ and the scale parameters correspond with each other. Blue and red correspond to $\sim 10^{-4}$ and $\sim 10^{-3}$ counts $\mathrm{cm}^{-2}\mathrm{s}^{-1}\mathrm{arcmin}^{-2}$, respectively.

at the right panel. The flux distribution of the high-$kT_e$ component is relatively uniform compared with that of the low-$kT_e$ component. It reflects that the ejecta component uniformly filled inside the Loop. In contrast, from the left panel, we clearly see the "limb-brightening" which reflects the spherical shell structure. Therefore, we confirmed that the low-$kT_e$ component comes from the surrounding ISM. We also found that the northeast flux is higher than that in the southwest. It suggests that the density is higher in the direction of the northeast than that of the southwest. The detailed shell structures are also seen from the left panel, for example, the "V-shape" knot at the southwest (Aschenbach & Leahy 1999; Leahy 2004).

From the left panel of figure 5.23, we found the flux distribution inside the Loop is far from what we expect in the uniform shell structure. This suggests the ambient density and the shell thickness varies considerably from region to region. Thus, we can study the line-of-sight shell structure of the Loop. Considering the relation between the surface brightness and the plasma density, the flux of the low-$kT_e$ component reflects the local density of the ISM. For example, the bright region in the northeast part is considered that the blast waves are expanding into the dense ISM there. In contrast, there is a low-flux region at the south of the Loop (see figure 5.23). It suggests the ambient density there is extremely low compared with other areas of the Loop. As shown by Uchida et al. (2008), we noticed that there is a large break in the south where the ISM density is very thin. In general, the velocity of the blast wave toward such tenuous ISM should become higher than other region. Therefore, it forms a blowout where the shell thickness must be thin.

From figure 5.23, we also found a large low-flux region at slightly west of the Cygnus Loop center. Although our FOV does not cover the whole region, the structure is close to a circular form, and we estimated the diameter to be $\sim 1.3°$. The size is comparable to that of the south blowout. The existence of such large low-flux region suggests that it has a blowout structure along the line of sight like the south blowout. This result confirms the prediction by Tsunemi et al. (2007) and Kimura et al. (2009). From figure 5.23, the northeast of the center also has lower flux than that of the surrounding region. It strongly indicates that the line-of-sight ambient density there is locally low as well as that in the south blowout. This region has a C-shape structure which could be explained by the superposition of the circular low-flux region and the bright region where the blast wave interacts with a small cloud. We estimate the diameter of this low-flux region to be $\sim 30'$. These results show the ambient density of the Cygnus Loop is quite different from region to region.

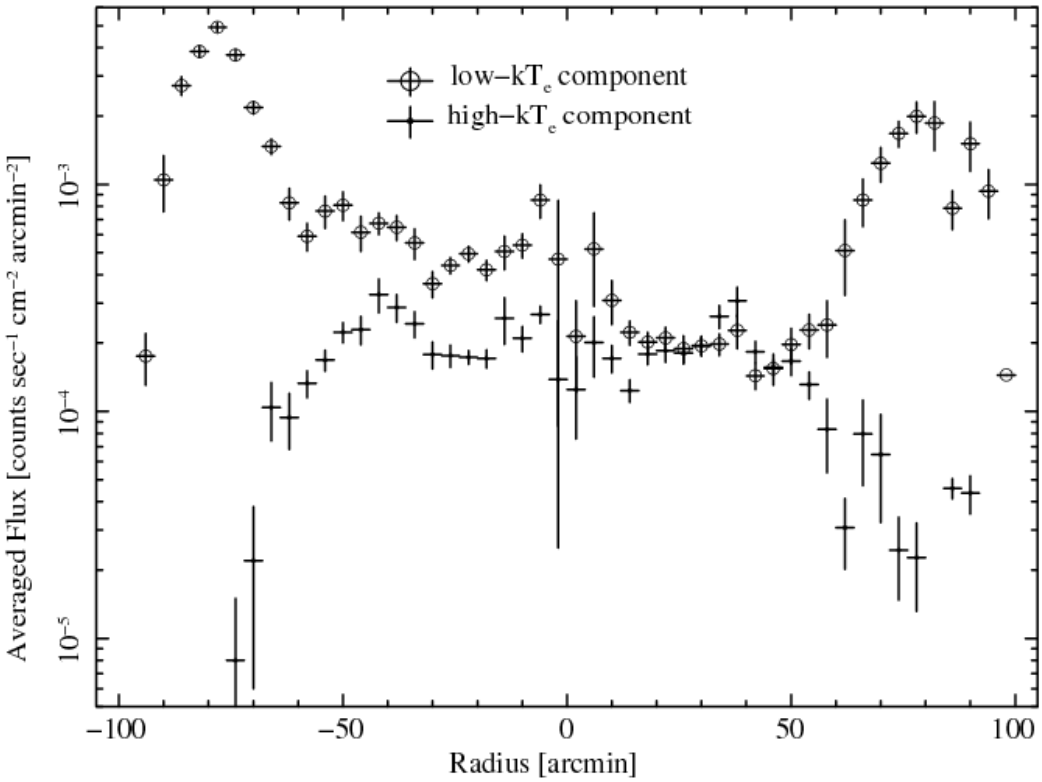


Figure 5.24: Averaged flux profile as a function of $R$. The circles and triangles represent the flux of low-$kT_e$ and high-$kT_e$ components, respectively.

**Evidence of Cavity Explosion**

To put our result into perspective, we plotted the flux of each component as a function of radius $R$ as shown in figure 5.24. From this figure, we found the flux of the high-$kT_e$ component (shown as crosses) decreases from the center to the outside, which reflects the spherical structure of the ejecta filled inside the Cygnus Loop. On the other hand, the flux of the low-$kT_e$ component (circles) has a limb-brightening structure, as mentioned in the previous section. Furthermore the low-$kT_e$ flux at the southwest ($R > 0$) is totally lower than that at the northeast. While the high-$kT_e$ flux distribution is approximately symmetric, the low-$kT_e$ flux is a few times higher at the northeast than that at the southwest. In addition, looking at the inner region of the Loop, the flux distribution of the low-$kT_e$ component is declining from $R = -50$ to $R = 50$. This fact suggests the ambient density of the Cygnus Loop globally decreases from the northeast to the southwest.

In order to estimate the ambient density more quantitatively, we calculated the EM of the low-$kT_e$ component and plotted it as a function of $R$. Figure 5.25 shows the EM distribution of the low-$kT_e$ component. We plotted the EM profiles from six rectangular

regions with different azimuthal angles as shown in figure 5.25 (NE-A to NE-E and SW). That are shown in figure 5.26. We simulated the EM profile of the shell component derived from the Sedov solution with different ambient density $n_0$ and estimated $n_0$ by comparing our observations with the EM models. In this model, we assume the shock radius of the Cygnus Loop to be 13 pc and the ejecta is filled in 90% of it. The results are shown in figure 5.26 with red lines. We also show the best-fit models using the data only in the limb-brightening regions with green lines. As for the northeast regions, the EM profiles inside the Loop are close to the models of $n_0$=0.3-0.4 $\mathrm{cm}^{-3}$ (red) while the EM values at the limb-brightening regions are higher than these models. On the other hand, applying the data only in the limb-brightening regions (green), $n_0$ increases to 0.7-0.9 $\mathrm{cm}^{-3}$. In any case, there are no Sedov models which agree with the EM profiles of the northeast part of the Cygnus Loop. The result is the same as the case of the southwest region while the ambient density $n_0$ is less than half of the northeast results. These results clearly show the Cygnus Loop can not be explained by a simple Sedov evolution model. As explained in Section 2.3, many previous studies show that the Cygnus Loop's SN explosion had occurred in a preexisting cavity (McCray & Snow 1979; Hester & Cox 1986; Hester et al. 1994; Levenson et al. 1997). Considering their results, it is natural that the EM distribution disagrees with a simple Sedov model, and thus, we concluded that our result also supports the cavity explosion as the origin of the Cygnus Loop from the standpoint of the X-ray spectral analysis. It should be noted that the Cygnus Loop is almost perfect circular in shape, although the EM (or flux) is globally higher in the northeast than that in the southwest. This fact strongly suggests that the northeast and the southwest blast waves should have hit the cavity wall very recently, and that the cavity-wall density is higher in the northeast than that in the southwest.

### 5.3.4 Conclusion

By analyzing the X-ray spectra, we clearly distinguished the ISM component from the ejecta component, and established a method to investigate the line-of-sight shell structure. From the flux distribution of the ISM component, we found three low-flux regions in the FOV; one is a well-known southwest blowout which is evidence of the cavity-wall break, and we also found other low-flux regions at the west and the northeast of the Cygnus Loop center. From the EM distribution of the ISM component, we support that the Cygnus Loop is originated from a cavity explosion. Then, the ISM component, or cavity wall does not have an uniform structure but has a lot of breaks or tenuous regions. We also found that the condition of the surrounding cavity wall is not uniform; the density of it is globally higher in the northeast than that in the southwest.

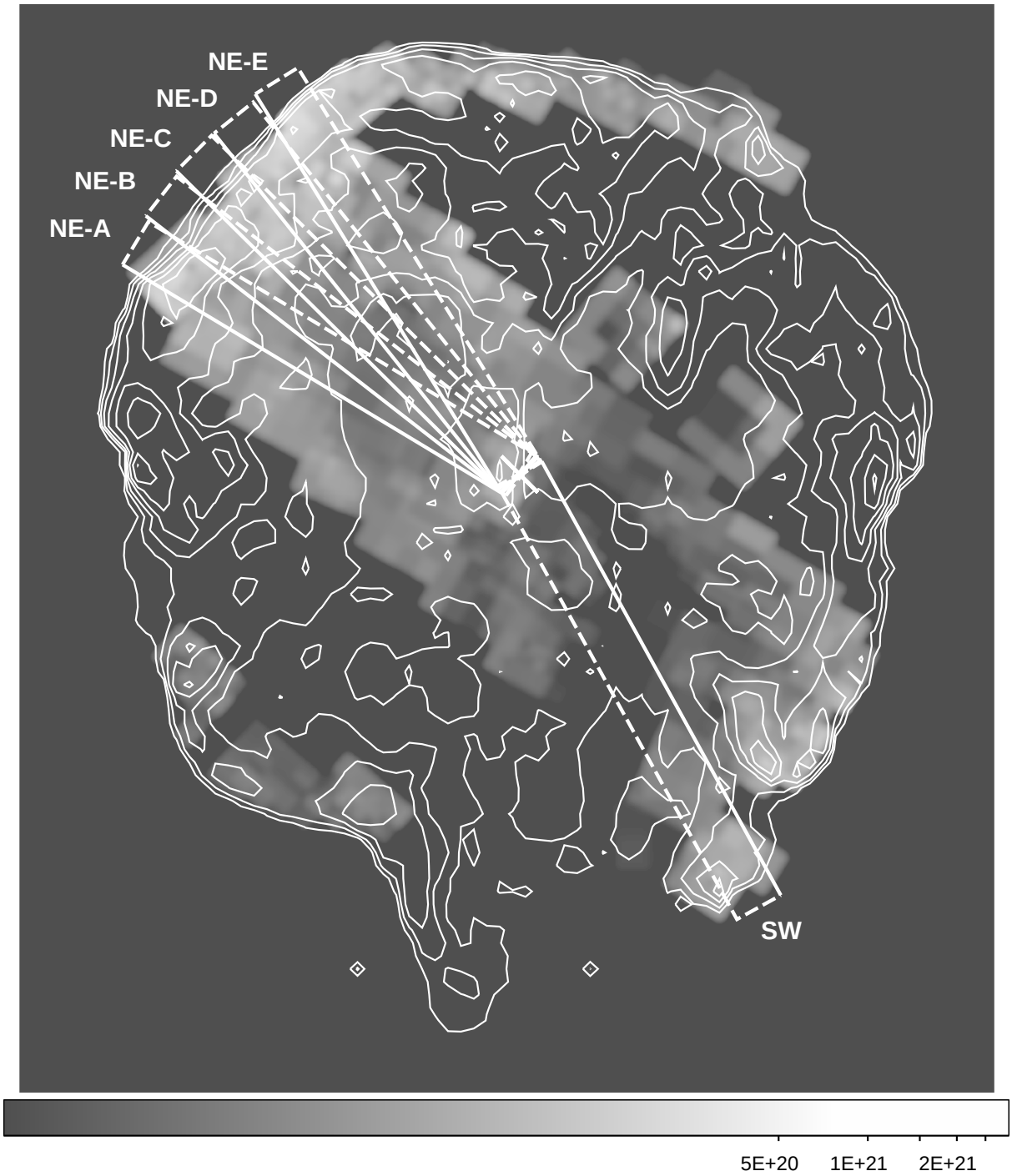


Figure 5.25: EM distribution of the low-$kT_e$ component in logarithmic scales overlaid with the white contour of the *ROSAT* HRI image.

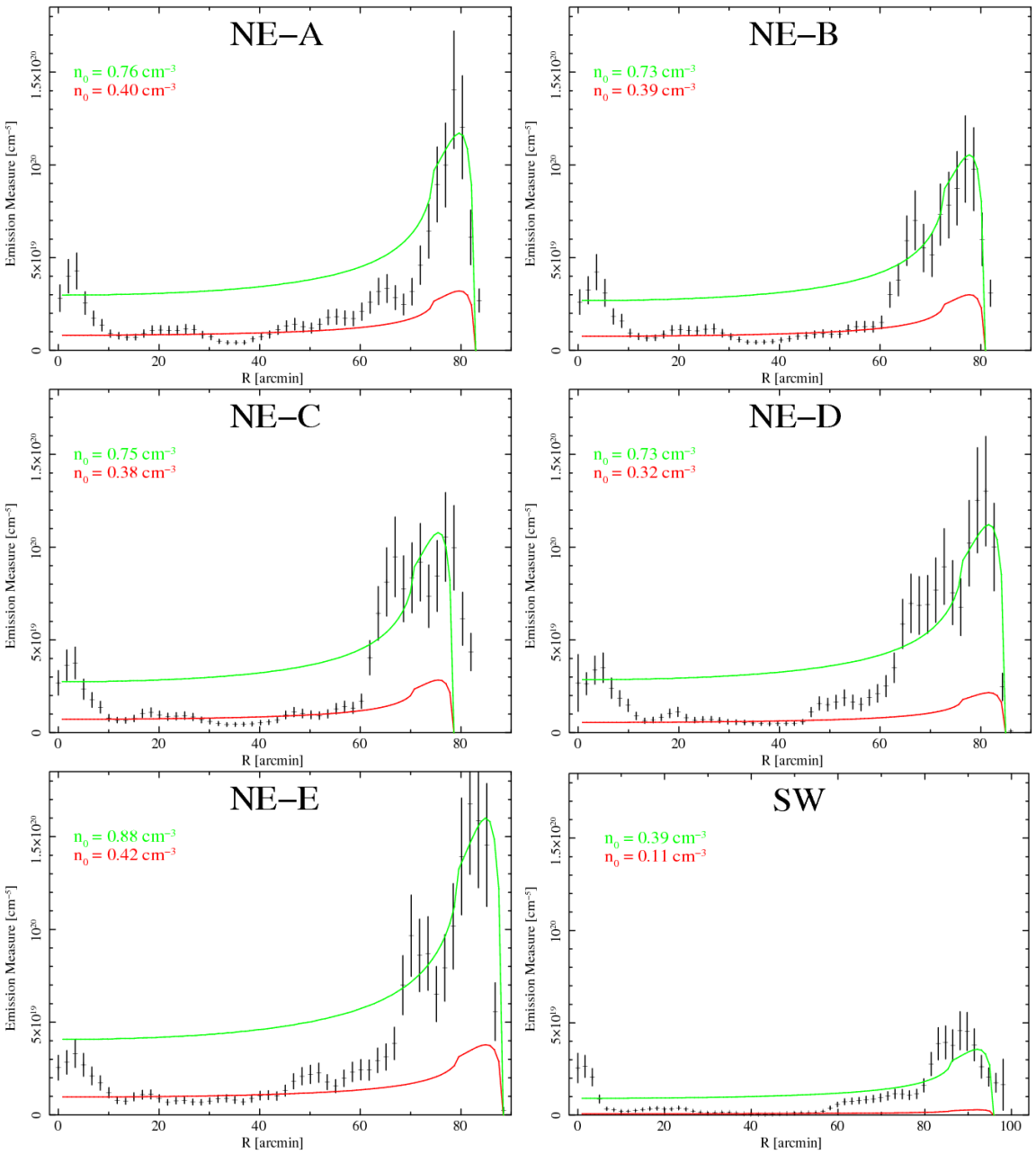


Figure 5.26: EM profiles as a function of $R$ calculated from the data in the rectangular regions shown in figure 5.25. The EM profiles based on the Sedov model and the estimated ambient densities $n_0$ are shown in red and green (see text).

Table 5.7: Spectral fit parameters

| | *single-component VNEI model* | | *two-component VNEI model* | |
|---|---|---|---|---|
| | region A | region B | region A | region B |
| $N_H$ [$10^{20}$ cm$^{-2}$] | 1.8 ± 0.3 | 3.4 ± 0.3 | 5.2 ± 0.2 | 7.0 ± 0.3 |
| | | | *Low-$kT_e$ component:* | |
| $kT_e$ [keV] | 0.59 ± 0.03 | 0.42 ± 0.02 | 0.24 ± 0.01 | 0.12 ± 0.01 |
| C | 0.24 ± 0.05 | 0.96 ± 0.21 | 0.27 (fixed) | |
| N | 0.22 ± 0.05 | 0.09 ± 0.03 | 0.10 (fixed) | |
| O | 0.23 ± 0.02 | 0.14 ± 0.02 | 0.11 (fixed) | |
| Ne | 0.44 ± 0.04 | 0.31 ± 0.03 | 0.21 (fixed) | |
| Mg | 0.26 ± 0.03 | 0.24 ± 0.03 | 0.17 (fixed) | |
| Si | 0.27 ± 0.06 | 0.30 ± 0.06 | 0.34 (fixed) | |
| S | (=Si) | (=Si) | 0.17 (fixed) | |
| Fe(=Ni) | 0.36 ± 0.04 | 0.22 ± 0.02 | 0.20 (fixed) | |
| log $\tau$ | 10.42 ± 0.03 | $10.82^{+0.07}_{-0.08}$ | $11.32^{+0.12}_{-0.16}$ | $< 12$ |
| flux [counts cm$^{-2}$s$^{-1}$arcmin$^{-2}$] | $8.90 \times 10^{-4}$ | $4.34 \times 10^{-4}$ | $7.49 \times 10^{-4}$ | $2.18 \times 10^{-4}$ |
| | | | *High-$kT_e$ component:* | |
| $kT_e$ [keV] | — | — | 0.88 ± 0.13 | 0.43 ± 0.02 |
| O(=C=N) | — | — | 0.34 ± 0.13 | 0.38 ± 0.07 |
| Ne | — | — | 0.82 ± 0.26 | 0.74 ± 0.12 |
| Mg | — | — | 0.56 ± 0.19 | 0.55 ± 0.10 |
| Si(=S) | — | — | 1.28 ± 0.42 | 0.79 ± 0.16 |
| Fe(=Ni) | — | — | $< 1.43$ | 0.48 ± 0.08 |
| log $\tau$ | — | — | $10.66^{+0.09}_{-0.12}$ | 11.11 ± 0.06 |
| flux [counts cm$^{-2}$s$^{-1}$arcmin$^{-2}$] | — | — | $1.41 \times 10^{-4}$ | $2.16 \times 10^{-4}$ |
| $\chi^2$/dof | 1043/739 | 728/548 | 868/738 | 637/547 |

# Chapter 6

# Ejecta Distribution

In this chapter, we discuss about the ejecta of the Cygnus Loop. In Section 6.1, we present the asymmetric ejecta distibution of the Cygnus Loop. Section 6.2 indicates the result of the first detection of the Ar-K line. In both sections, we also discuss about the origin of the Cygnus Loop.

## 6.1 Asymmetric Ejecta Distribution

As shown in the Chapter 5, the spectra form the Cygnus Loop are generally well fitted by the two-component VNEI model. The high-$kT_e$ component is originated from the ejecta of the Cygnus Loop. They provide a clue to obtaining the information about the type of the SN explosion and the condition of the progenitor star.

Section 6.1 is based on the results of Uchida et al. (2009c).

### 6.1.1 Observations

In order to investigate the ejecta distribution of the Cygnus Loop, we used 14 and 7 pointings observation data obtained by the *Suzaku* and the *XMM-Newton* observatories. Their FOV are all located on the inside of the Loop. The target names aere P3 to P7, P9, P11 to P17, and P20 for *Suzaku* and Pos-2 to Pos-6, Pos-8, and Pos-9 for *XMM-Newton* (see Table 4.2 and 4.1).

### 6.1.2 Spectral Analysis

To investigate the plasma structure of the Cygnus Loop, we divided the entire FOV into several box regions outlined in white line in Figure 6.1. In order to equalize the statistics, we initially divided all images of XIS1 or MOS2 into two parts and if each divided region

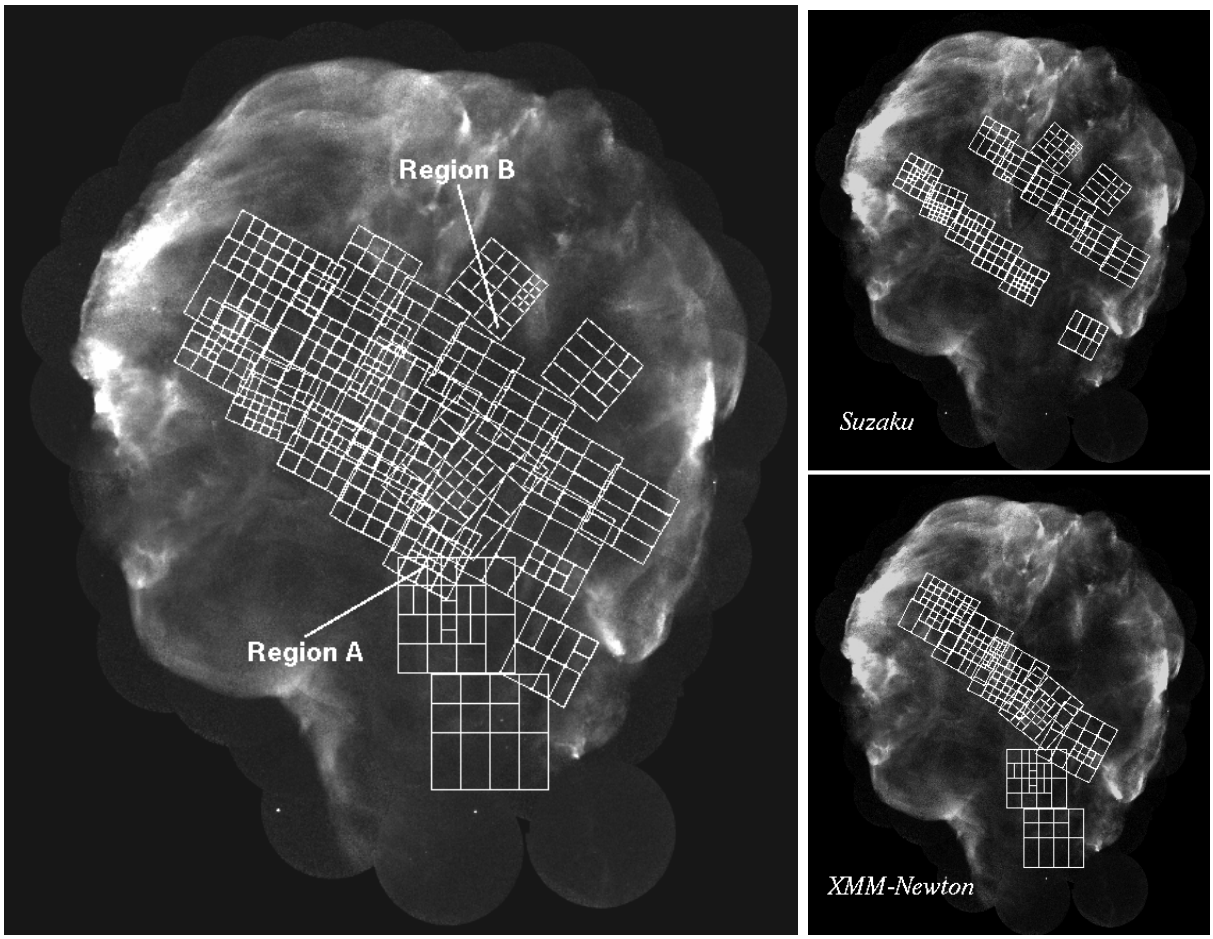


Figure 6.1: Left panel shows the *ROSAT* HRI image of the entire Cygnus Loop overlaid with the spectral extraction regions with white rectangles. Right two panels show the extraction regions for *Suzaku* (top panel) and *XMM-Newton* (bottom panel).

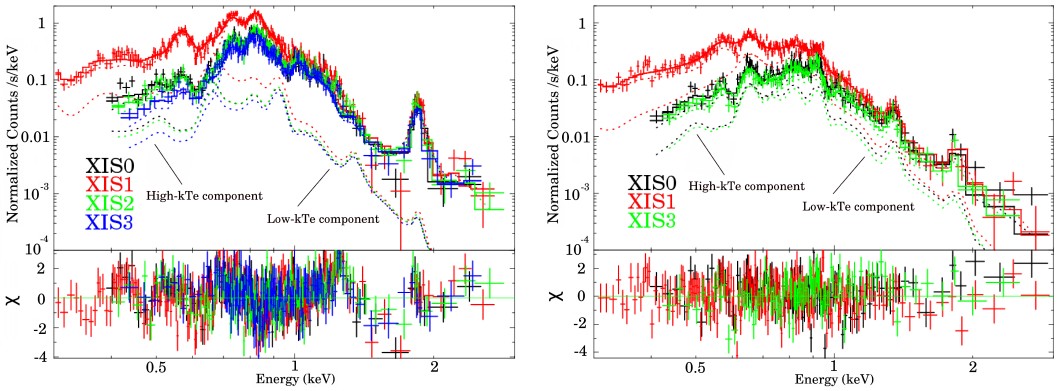


Figure 6.2: Example spectra from the regions where Fe and Si are the most abundant (region-A: left) and the most depleted (region-B: right), respectively. The best-fit curves are shown with solid line and two components are shown with dotted lines. The high- and the low-$kT_e$ components cross at $\sim$0.65 keV (region-A) and $\sim$0.7 keV (region-B), respectively. The residuals are shown in the lower panels. In the left panel, black, red, green, blue correspond to the XIS 0, 1, 2, 3. In the right panel, black, red, green correspond to the XIS 0, 1, 3.

has more than 10,000 photons, it was once again divided. In this way, we obtained 415 box regions. Each region contains 5,000-10,000 photons for XIS1 and MOS2. The side length of each box ranges from 2.2′ to 14′. Therefore box sizes are not smaller than the angular resolution capability of the *Suzaku* XIS. We grouped 415 spectra into bins with a minimum of 20 counts so that $\chi^2$ statistics are appropriate. We applied the two-component VNEI model for the spectra analysis. All the spectra are well fitted by the two-component VNEI model rather than the single-component VNEI model. The detailed parameters and the way of fitting is shown in Section5.3.

The values of the reduced $\chi^2$ shows around $\sim$1.5 and the degrees of freedom are 300-400. Some regions overlap each other and we fitted these spectra separately. In cases like this, we compared each best-fit parameter values and confirmed that they are just within the uncertainties. The example spectra and the best-fit curves are shown in Figure 6.2 and the best-fit parameters are shown in Table 6.1. These two spectra are taken from the region where Fe and Si are the most abundant or the most depleted, respectively. The extracted regions are shown in Figure 6.1.

Figure 6.3 shows the electron temperature distribution of each component. The left panel shows the best-fit $kT_e$ parameters of the high-$kT_e$ component that represents the plasma temperature of the ejecta component. From the left panel, we show the inhomogeneous temperature distribution of the ejecta component. The values of $kT_e$ range

Table 6.1: Spectral fit parameters

| Parameter | region-A | region-B |
|---|---|---|
| $N_H$ [$10^{20}$ cm$^{-2}$] | 3.6 ± 0.2 | 2.6 ± 0.2 |
| Low-$kT_e$ component: | | |
| $kT_e$ [keV] | 0.19 ± 0.01 | 0.28 ± 0.01 |
| C | 0.27 (fixed) | |
| N | 0.10 (fixed) | |
| O | 0.11 (fixed) | |
| Ne | 0.21 (fixed) | |
| Mg | 0.17 (fixed) | |
| Si | 0.34 (fixed) | |
| S | 0.17 (fixed) | |
| Fe(=Ni) | 0.20 (fixed) | |
| log $\tau$ | $11.49^{+0.05}_{-0.04}$ | $11.12^{+0.03}_{-0.03}$ |
| EM [$10^{18}$cm$^{-5}$] | 6.23 ± 0.19 | 4.27 ± 0.14 |
| High-$kT_e$ component: | | |
| $kT_e$ [keV] | 0.42 ± 0.01 | 0.63 ± 0.01 |
| O(=C=N) | 0.47 ± 0.08 | 0.31 ± 0.02 |
| Ne | 0.75 ± 0.09 | 0.47 ± 0.05 |
| Mg | 0.21 ± 0.10 | 0.41 ± 0.08 |
| Si(=S) | 5.36 ± 0.48 | 0.49 ± 0.18 |
| Fe(=Ni) | 2.92 ± 0.05 | 0.55 ± 0.03 |
| log $\tau$ | $11.76^{+0.10}_{-0.06}$ | 10.82 ± 0.02 |
| EM [$10^{18}$ cm$^{-5}$] | 0.55 ± 0.01 | 0.68 ± 0.02 |
| $\chi^2$/dof | 441/308 | 527/402 |

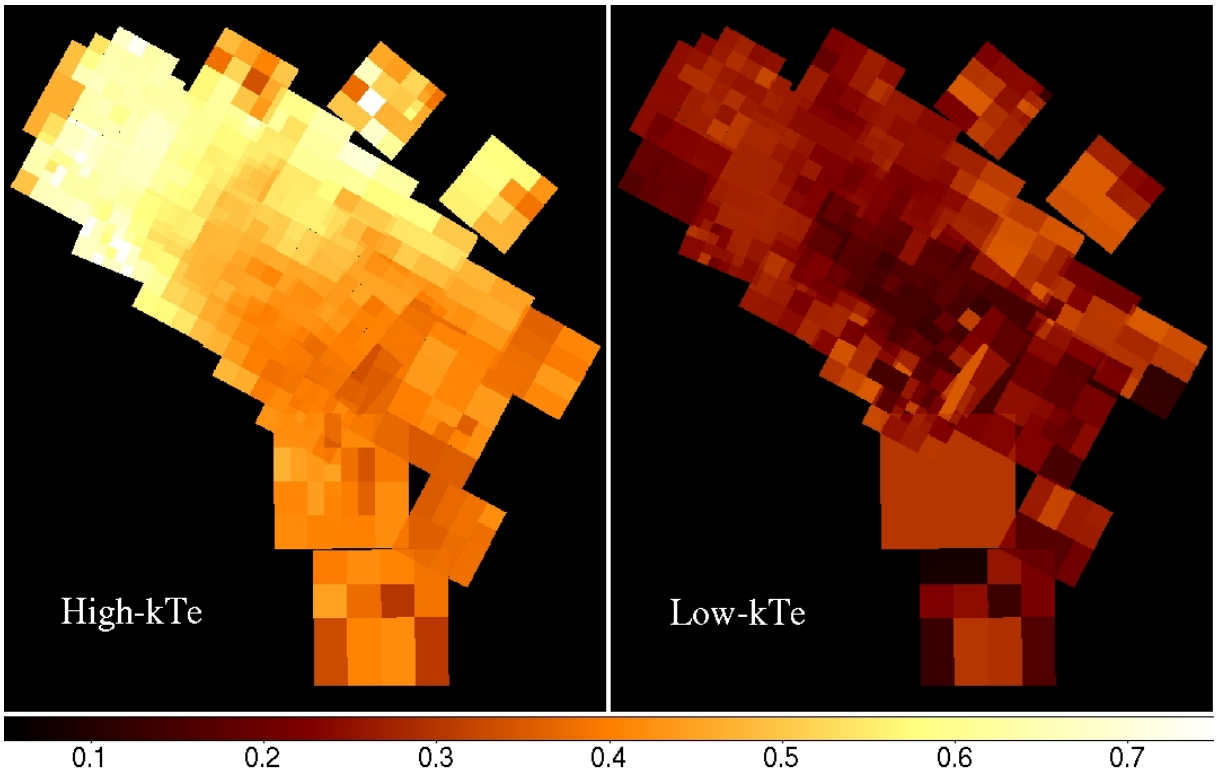


Figure 6.3: Electron temperature distribution of each component. The left and right panel shows the distribution of the high- and low-$kT_e$ component, respectively. The values of $kT_e$ are in units of keV.

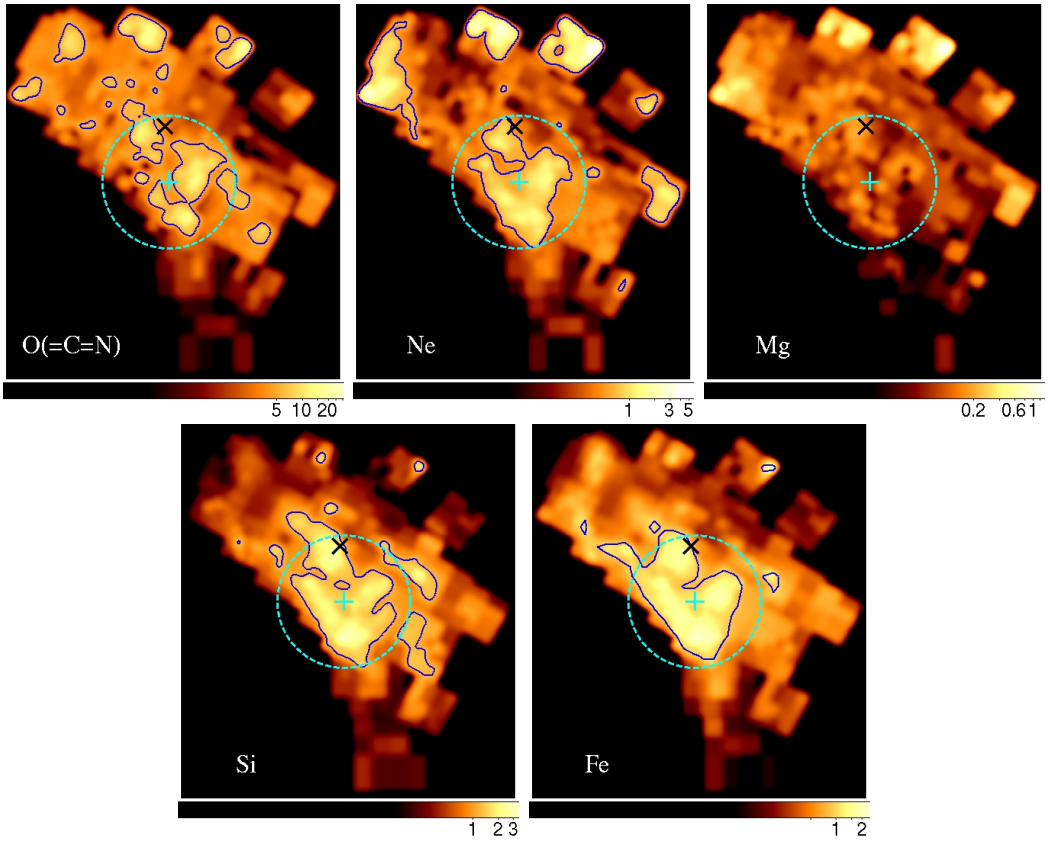


Figure 6.4: EM distributions of the heavy elements in the logarithmic scales. The black X-mark shows the geometric center of the Loop (Levenson et al. 1998). The blue contour shows the EM level of $1/e$ of the maximum around the geometric center. The light blue cross-mark and the dotted circle represent the "metal center" and the "metal circle", respectively (see 6.1.3). The values are in units of $10^{14}\mathrm{cm}^{-5}$.

from 0.4 keV to 0.7 keV and they are lower in the southwestern part than those in the northeastern part. The ejecta temperature of the Cygnus Loop shows smooth decrease from northeast to the southwest. The averaged temperature is ∼0.49 keV. The right panel shows the map of the $kT_e$ parameter obtained from the low-$kT_e$ component that represents the temperature of the swept-up cavity material. The averaged value is ∼0.23 keV and it ranges from 0.2 keV to 0.3 keV. The temperature of the low-$kT_e$ component near the center of the Loop is lower than that of the surrounding temperature. From Figure 6.3, we clearly separated the high-$kT_e$ component and the low-$kT_e$ component just as the observation obtained in Tsunemi et al. (2007), Katsuda et al. (2008a), and Kimura et al. (2009).

Figure 6.4 (or 6.5) shows the EM distributions of the heavy elements. The images are smoothed by Gaussian kernel of $\sigma$=2.8′. The color code scale is normalized by the

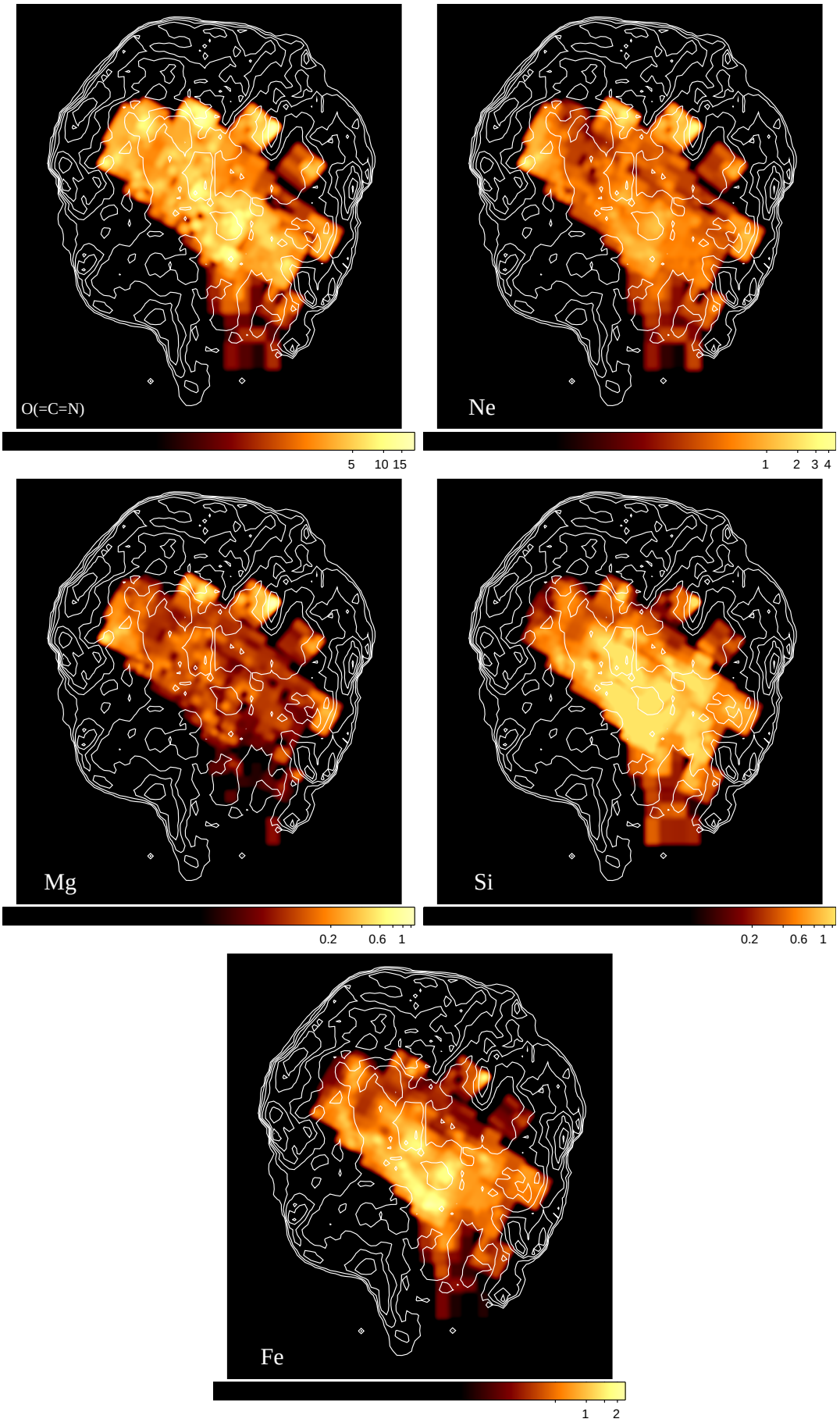


Figure 6.5: Same as Figure 6.4, but overlaid with the white contours from the *ROSAT* HRI image.

maximum values. From Figure 6.4, the EM of Mg is relatively low compared with those of the other elements. The EM values of O, Ne, Mg are higher in the northeast than those around the center while the EM values of Si and Fe are larger in the center and decrease outward. These results are consistent with those of Tsunemi et al. (2007), Katsuda et al. (2008a), and Kimura et al. (2009). These earlier studies were all conducted from the northeast to the southwest in their FOV. Our analysis revealed the plasma structure from the northwest to the southeast of the Loop. The averaged value of each EM [$\times 10^{14}\,\mathrm{cm}^{-5}$] is 3.20 (O=C=N), 0.39 (Ne), 0.08 (Mg), 0.81 (Si=S), 0.59 (Fe=Ni), respectively. We show the geometric center estimated by Levenson et al. (1998) with the black X-mark in Figure 6.4.

### 6.1.3 Discussion

**Low abundances of the low-$kT_e$ component**

We analyzed all the spectra with using a two-component model: the low-$kT_e$ component forms a shell-like structure and the high-$kT_e$ component fills inside (Tsunemi et al. 2007; Katsuda et al. 2008a; Kimura et al. 2009). The fixed abundances of the low-$kTe$ component are depleted compared to the solar values. Cartledge et al. (2004) measured the abundance of the interstellar oxygen in the solar neighborhood along 36 sight lines and showed 0.4 times the solar value. Wilms et al. (2000) employed 0.6 of the total interstellar abundances for the ISM oxygen abundance. The abundances we fixed are significantly lower than those results and it needs to be discussed. The metal deficiency of the ISM component of the Cygnus Loop has been shown by the earlier X-ray observations (Miyata & Tsunemi 1999). The other observations in X-ray by using the *Suzaku* , *XMM-Newton* , and *Chandra* also showed the metal depletion at the rim (Leahy 2004; Tsunemi et al. 2007; Katsuda et al. 2008b). Meanwhile, Katsuda et al. (2008b) found an enhanced abundance region in the very edge of the northeastern rim. The abundance there is about half the solar value which is much higher than those other rim regions. This result is consistent with the observations of the ISM abundance in the solar neighborhood (Wilms et al. 2000; Cartledge et al. 2004). Therefore, the metal abundances of the periphery of the Loop may be higher than those observed in X-ray. Any line of sight through the remnant almost certainly intersects various emitting regions. However, the line of sight near the limb can intersect the very limited plasma condition. Therefore, we can expect that the very rim region Katsuda et al. (2008b) observed consists of thermal plasma with ISM abundance while other regions may include either thin thermal plasma with low abundance or non-thermal emission. Katsuda et al. (2008c) tried to fit the spectrum

with a combination of thin thermal plasma with ISM abundance and the non-thermal emission. They reached no clear result probably due to the simplicity of the model. Although most of the rim regions show low abundance from the X-ray data analysis point of view, it still remains an open question.

**Displacement of the metal distribution from the geometric center**

We noticed that the strong EM regions concentrate just south of the geometric center. Si and Fe concentrate in the inner part while Ne and O have strong regions both in the inner part and the outer part within our FOV. Mg has strong regions only in the outer part. In this paper, we will focus on the strong regions near the geometric center.

The contours in Figure 6.4 show the EM level of $1/e$ of the maximum near the geometric center. The concentration of the inner part of various metals is obviously away from the geometric center. The spread of the strong regions indicated by the contour is not clear in the southeastern region due to the lack of observation. Therefore, it is difficult to precisely determine the spread. Taking into account the lack of information in the southeastern region, we speculate that the center of the metal distribution is determined by the centroid of the Fe distribution at the south of the geometric center. We call it the "metal center", which is located on $\alpha = 20^h51^m14^s, \delta = 30°40'35''$ (J2000), as shown by the light blue cross-mark in Figure 6.4.

We found that the metal center is separated from the geometric center by $25'$ toward the south. It is not clear why it is displaced from the geometric center. On the simple assumption that the SN explosion occurred symmetrically in the uniform ISM, the metals should distribute symmetrically and its center should overlap with the geometric center. The Cygnus Loop shows a nearly circular shape with an exception of the south blowout region. However, the X-ray surface brightness and the optical filamentation suggest that the ambient medium of the Cygnus Loop is not uniform. We consider that its non-uniformity is prominent toward the south blowout region. If the south blowout is originated from the lower-density cavity wall or the ISM, the displacement of the metal distributions to the south could be naturally explained. In general, the non-uniformity produces the asymmetrical reverse shocks. Taking into account the estimated age of the Loop, the reverse shocks should have reached the center of the Loop. However, the times for the reverse shocks to return to the center, $t_{\rm R}$ significantly depend on the ambient density in the direction which the forward shock propagates. From the recent theoretical calculation, Ferreira & de Jager (2008) obtained the relation of $t_{\rm R} \propto (\rho_{\rm ISM})^{-1/3}$, where $\rho_{\rm ISM}$ represents the ambient density. Therefore, in directions where $\rho_{\rm ISM}$ is higher, the forward shock decelerates and the reverse shock propagates toward the center more quickly.

From the morphological point of view, it is suggested that the cavity wall must be very thin in the south blowout region, although the origin of the blowout is still not clear.

As described in Section2.3, from the radio observations, Uyaniker et al. (2002, 2004) and Sun et al. (2006) claim that the extra SNR exists in the south and interacts with the Cygnus Loop. Their main arguments are the difference of the radio morphology and the polarization intensity between the main part of the Loop and the south blowout. However, as shown in Section5.1, we obtained no evidence that a smaller SNR exists at the same distance to the Cygnus Loop. We also found that the emission from the cavity material of the Loop is relatively weak. It suggests that the X-ray shell is very thin in the south. On the other other hand, the ambient medium in the north part of the Cygnus Loop is thought to be denser than that in the south. The north areas have the strong emission in X-ray and it suggests that the forward shock has decelerated enough to become radiative in places. Then, the reverse shocks in some part other than south should be formed earlier and reaches the center faster than that in the south. In that case, the pressure exerted by the north reverse shock is higher than that exerted by the south one. If the metal distributions are formed by the imbalance of the pressure surrounding them, they should be created southward from the geometric center. Our result is consistent with the assumption that the south blowout is originated not from an extra SNR but from a non-uniformity of the cavity wall.

**Metal circle and the progenitor star mass**

Although the metal abundance is not uniform within the high-$kT_e$ component, the contents in our FOV reflect the abundance of the progenitor star. We calculate the metal abundances around the metal center and in our FOV relative to O in order to compare them with the theoretical models. We defined the "metal circle" which is centered in the metal center with radius of $25'$. We added the EM of ejecta component of each region weighting each area of the region for the heavy elements, O, Ne, Mg, Si, and Fe. These values reflect the total amount of each heavy element in our FOV. Then, we obtained the number ratios of each element relative to O. Figure 6.6 shows the number ratios of Ne, Mg, Si and Fe relative to O of the ejecta component. The vertical bars show the uncertainties of the values. The black lines represent the results from the metal circle and the entire FOV. We also plotted the core-collapse models (Woosley & Weaver 1995) for various progenitor masses and Type Ia SN models (Iwamoto et al. 1999) for comparison. The result from the metal circle is similar to that from our entire FOV, which suggests the mixing of the metal. We found that the calculated Ne/O, Mg/O, and Si/O are in good agreement with the core-collapse model with the progenitor mass of $12M_{\odot}$. However, the

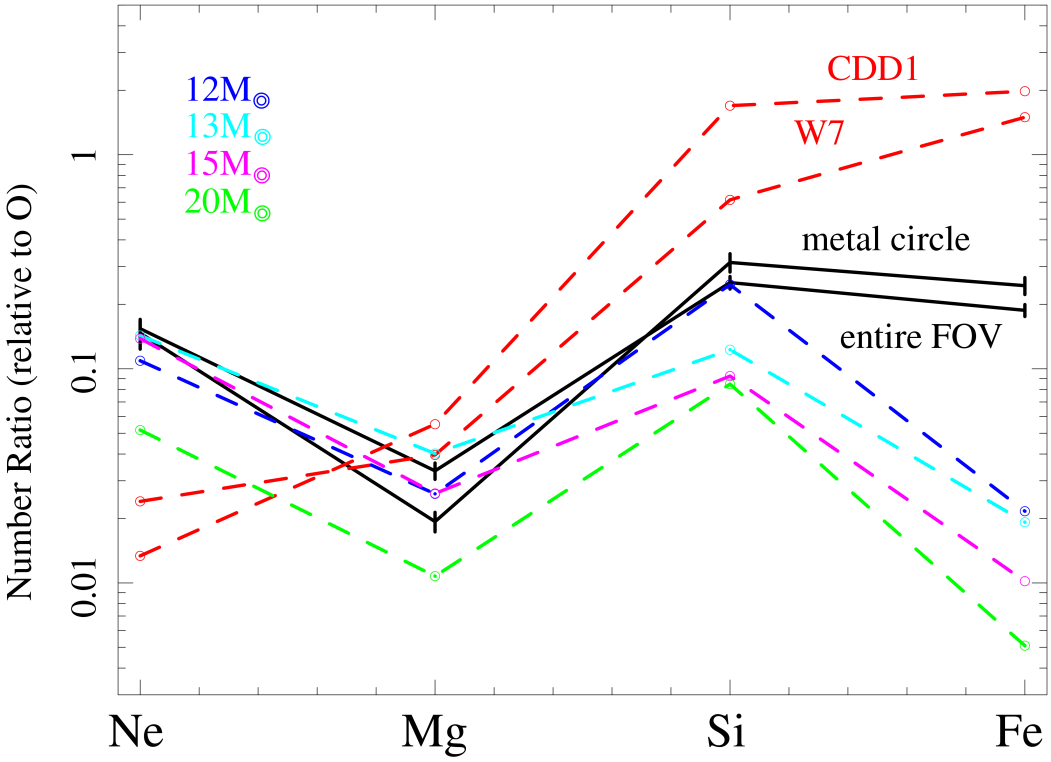


Figure 6.6: Number ratios of Ne, Mg, Si, and Fe relative to O of the high-$kT_e$ component estimated from the metal circle and that from the entire FOV (black lines). Dotted red lines represent the CDD1 and W7 Type Ia supernova models of Iwamoto et al. (1999). Dotted blue, light blue, magenta, and green lines represent core-collapse models with progenitor masses of 12, 13, 15, $20M_{\odot}$, respectively (Woosley & Weaver 1995).

Fe/O ratio is 10 times higher than that of the $12M_{\odot}$ model, and it does not fit any other models. This may be partly because our FOV does not cover the entire region of the Loop. From Figure 6.4, we found that the EM values of O, Ne, Mg are higher around our FOV rather than those near the center of the Loop. By contrast, Si and Fe decrease toward the outside of the Loop. If these trend continue to the outside of our FOV, we expect that the total EMs of O, Ne, Mg will increase considerably more than those of Si and Fe. In that case, Si/O and Fe/O estimated by the whole remnant will decrease and approach the values the core-collapse models rather than those of the Type Ia SN models. We can conclude that the progenitor star mass of the Cygnus Loop is 12-15$M_{\odot}$.

### 6.1.4 Conclusion

We analyzed the metal distribution of the Cygnus Loop using 14 and 7 pointings observation data obtained by the *Suzaku* and the *XMM-Newton* observatories. We fit all the

spectra by the two-$kT_e$ non-equilibrium ionization plasma model (VNEI model) as shown by the earlier observations (Tsunemi et al. 2007; **?**; Kimura et al. 2009). The results indicate that Si and Fe are more abundant near the center of the Loop than those around our FOV. We measured a center of the Si and Fe distributions from the metal spread and called it as "metal center". We found that the metal center is located at the southwest of the geometric center toward the blow-out region.

From the best-fit parameters, we also estimated the progenitor mass of the Cygnus Loop. We calculated the number ratios of the heavy elements (relative to O) both from the entire FOV and inside the metal circle. The result from the metal circle is not different from that of our entire FOV, which suggests mixing of the metals. The results show that Ne/O, Mg/O, and Si/O are well fitted by the core-collapse models with progenitor masses of 12, 13, $15M_{\odot}$. However, Fe/O is 10 times higher than those of the models. This may be partly because our FOV does not cover the entire region of the Loop. We can conclude that the progenitor mass of the Cygnus Loop is 12-$15M_{\odot}$.

## 6.2 First Detection of Ar-K Line Emission

In this section, we present the result of the spectral analysis of the Cygnus Loop by using all available data obtained by *Suzaku* and *XMM-Newton* satellites.

Section 6.2 is based on the results of Uchida et al. (2009d).

### 6.2.1 Observations

The 41 observations are summarized in Table 4.1 and 4.2. Their FOV are shown in Figure 6.7. Top and bottom panels show the FOV of *Suzaku* XIS and *XMM-Newton* MOS, respectively. As shown in Figure 6.7, our FOV covers more than half the region of the Cygnus Loop. We therefore intended to improve a signal-to-noise ratio and created a global spectrum of the Cygnus Loop by using all the available data.

### 6.2.2 Spectral Analysis

First, we created a spectrum from each observing region and combined them with FTOOLS *mathpha*. In this analysis, we treated the XIS, MOS, and pn data independently. In order to generate a RMF and an ARF, we employed *xisrmfgen* (Ishisaki et al. 2007) and *xissimarfgen* for the *Suzaku* data, *rmfgen* and *arfgen* for the *XMM-Newton* data. We added the RMF and the ARF with FTOOLS *addrmf* and *addarf*, respectively. Thus, we obtained the combined XIS, MOS, and pn spectra. Figure 6.8 shows the spectra from the entire FOV of the Cygnus Loop. Top, middle, and bottom panels show a spectrum obtained from XIS, MOS, and pn, respectively. We also show background spectra in red lines. In these spectra, we can see many emission lines, such as C Ly$\alpha$, N He$\alpha$, O He$\alpha$, O Ly$\alpha$, the Fe-L complex, Ne He$\alpha$, Ne Ly$\alpha$, Mg He$\alpha$, Si He$\alpha$, Si He$\beta$, and S He$\alpha$. Since these lines are all located below $\sim 3.0$ keV, they are clearly detected above the background level. On the contrary, it is difficult to detect the line emissions above $\sim 3.0$ keV because the X-ray emission is buried in the background level. Since the Cygnus Loop is a middle-aged SNR, the electron temperature is much lower (0.2-0.9 keV; Uchida et al. 2009c) than that of the younger SNRs. Previous studies have not detected the line emissions of Ar, Ca, Cr, and Fe-K from the Cygnus Loop and thus the abundances of these elements (except for Fe) have not been determined. For example, Tsunemi et al. (2007) fixed Ar and Ca abundances to their solar values and some other studies makes their spectral analysis in almost the same way (e.g., Leahy 2004; Kimura et al. 2009; Uchida et al. 2009c). However, from Figure 6.8, some line structures are seen around 3.0 keV above the background level due to the improvement of the statistics. This structure is likely to be

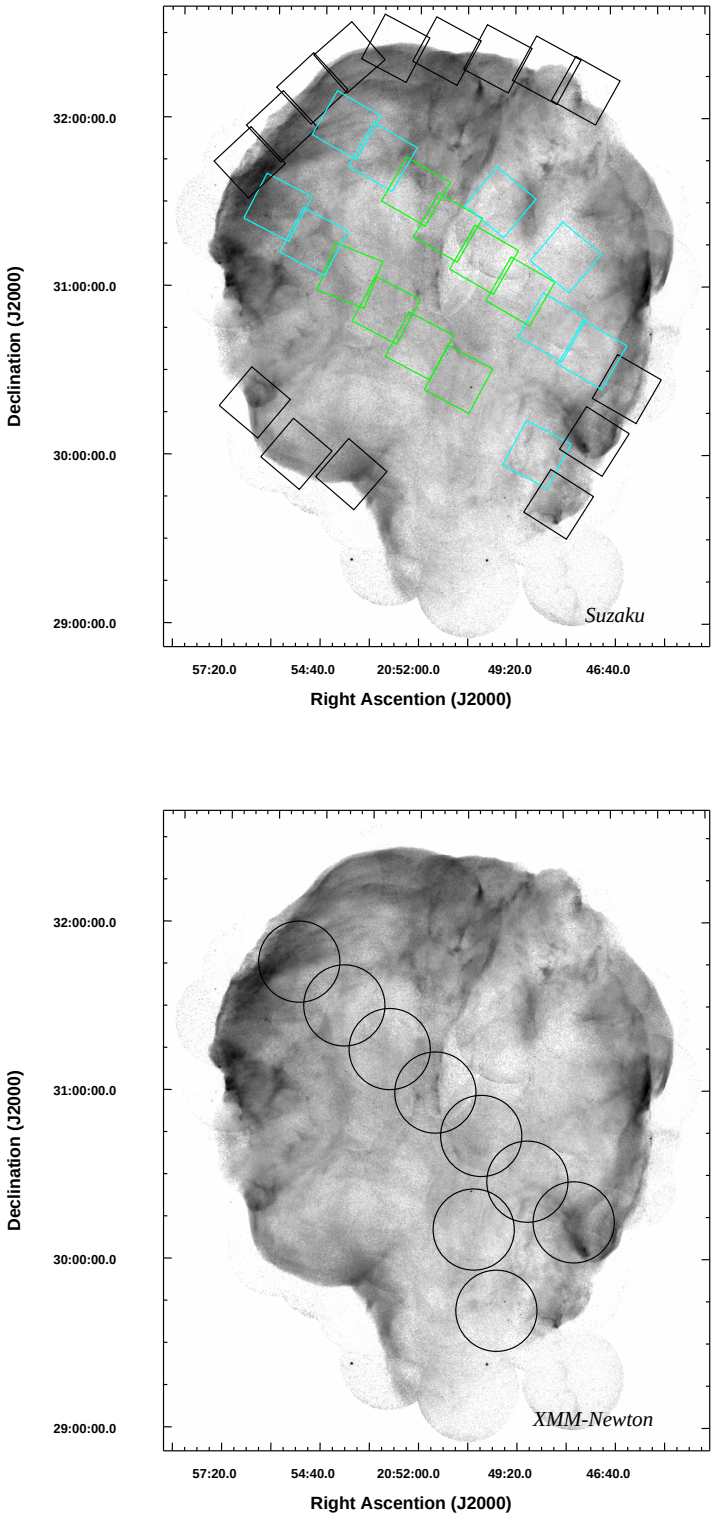


Figure 6.7: *ROSAT* HRI image of the Cygnus Loop. The FOV of *Suzaku* XIS and *XMM-Newton* MOS are shown with white rectangles (top) and circles (bottom), respectively. In left panel, green, blue, and white correspond to Region-A, Region-B, and Region-C, respectively.

Table 6.2: Spectral parameters inferred from combined XIS data (see Figure 6.9)

| | | Line Center [eV] | | | | | | |
|---|---|---|---|---|---|---|---|---|
| | $kT$ [keV] | A | B | C | D | E | F | $\chi^2$/dof |
| Bremss+4Gauss | $0.56^{+0.01}_{-0.02}$ | $1569^{+8}_{-15}$ | 1849±1 | $2181^{+6}_{-10}$ | $2435^{+3}_{-2}$ | – | – | 126/101 |
| Bremss+6Gauss | $0.56^{+0.01}_{-0.04}$ | $1571^{+7}_{-6}$ | 1850±1 | 2182±1 | $2435^{+3}_{-2}$ | $2905^{+92}_{-61}$ | $3113^{+54}_{-48}$ | 95/98 |

made by S He$\beta$ and Ar He$\alpha$ lines which have not been detected by previous observations. This structures are seen in all three spectra, and it is particularly prominent in the XIS spectrum due to the low background level of the *Suzaku* satellite.

Figure 6.9 shows 1.5-5.0 keV spectra obtained from XIS data with different models. First we fitted the spectrum with bremsstrahlung plus four Gaussian components as shown in Figure 6.9 top panel. In this model, four Gaussian components correspond to the emission lines of Mg He$\beta$, Si He$\alpha$, Si He$\beta$, and S He$\alpha$. The parameters in the bremsstrahlung model were all free such as the $kT_e$ and the emission measure (EM). In the Gaussian models, we set all parameters such as line energy, line width, and the EM to be free. We fixed the column density $N_{\rm H}$ to be $4.0\times10^{20}{\rm cm}^{-2}$ (Inoue et al. 1980; Kahn et al. 1980). The best-fit parameters are shown in Table 6.2. As shown in Table 6.2, this model is statistically acceptable, but the spectrum shows an excess from the model at around 3.0 keV (figure 6.9 top). Thus we added two more Gaussian components to the model (figure 6.9 middle) and then the reduced $\chi^2$ value was improved as shown in Table 6.2. Furthermore, the line center energies of the extra components are $2.89 \pm 0.04$ keV and $3.11 \pm 0.03$ keV, respectively, which are close to the expected values for S He$\beta$ (2.884 keV) and Ar He$\alpha$ (3.104 keV) lines according to the Astrophysical Plasma Emission Code (APEC[1]). From this result, we confirmed the excess structure at 3.0 keV is attributed to the S He$\beta$ and Ar He$\alpha$ lines.

In order to determine the abundance of Ar, we next fitted the spectrum with a VNEI model (figure 6.9 bottom). As shown by Tsunemi et al. (2007), the Cygnus Loop spectrum generally consists of two components with different origins: high-temperature ejecta component and low-temperature ISM component. Then we applied two-component VNEI model for the fitting. First, we set all the abundances of the heavy elements free. However this model cannot reach the physically meaningful results. Therefore, in the low-$kT_e$ component, we fixed the metal abundances to the values from the result of Tsunemi

[1]http://cxc.harvard.edu/atomdb/WebGUIDE/index.html

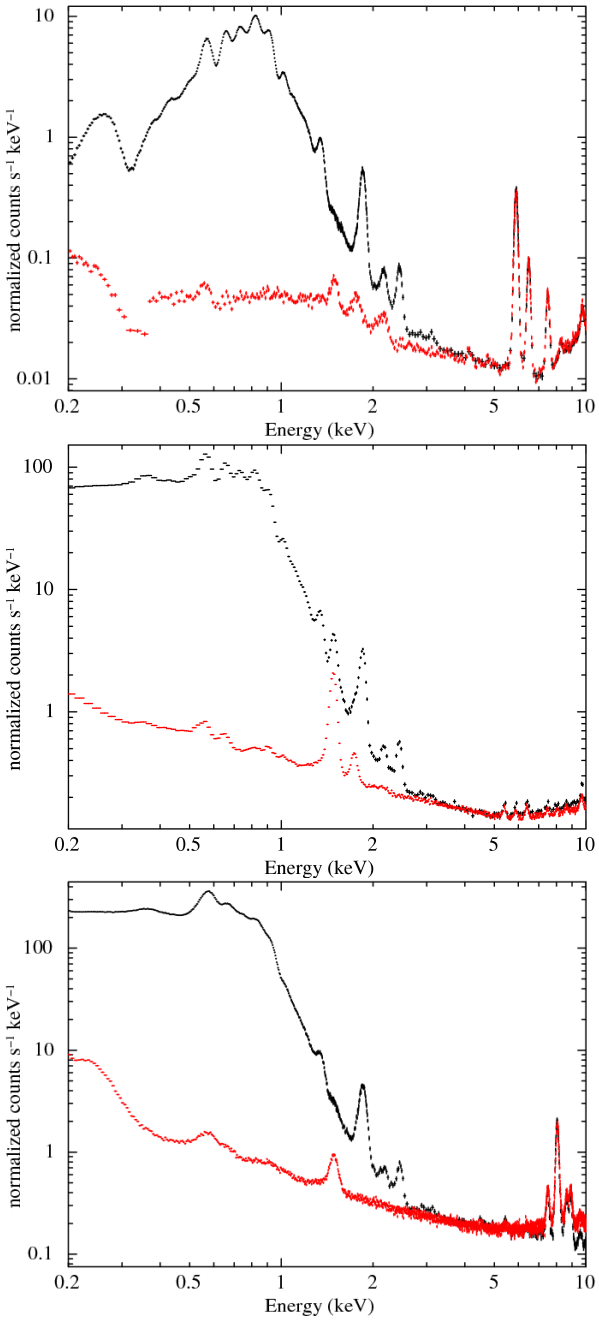


Figure 6.8: Spectra from the entire FOV of the Cygnus Loop. Top, middle, and bottom panels show a spectrum obtained from XIS, MOS, and pn, respectively. Background spectra are also shown in red.

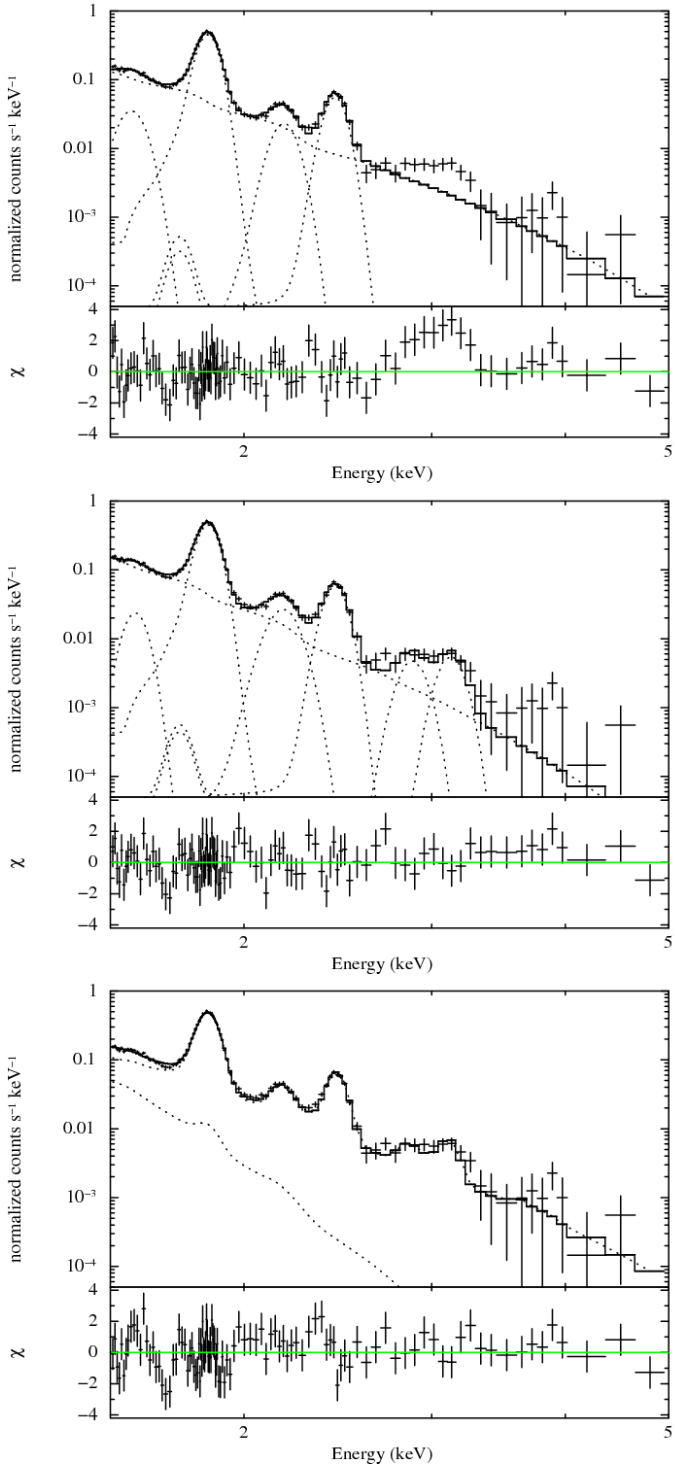


Figure 6.9: 1.5-5.0 keV spectra of Cygnus Loop with different models. We combined all XIS data shown in Figure 6.7 top. They are fitted with bremsstrahlung plus four Gaussian components (top), bremsstrahlung plus six Gaussian components (middle) and two-component VNEI model (bottom), respectively. The residuals are shown in the lower panels.

Table 6.3: Spectral parameters (see Figure 6.9 bottom and Figure 6.10)

| | Ejecta Component | | | | ISM Component | | |
|---|---|---|---|---|---|---|---|
| | $kT$ [keV] | log $\tau$ | Si | Ar | $kT$ [keV] | log $\tau$ | $\chi^2$/dof |
| XIS | 0.59±0.01 | $11.08^{+0.03}_{-0.02}$ | 1.91±0.02 | 7.88±2.19 | <0.3 | $10.84^{+0.08}_{-0.10}$ | 140/107 |
| MOS | $0.54^{+0.02}_{-0.01}$ | 11.08±0.06 | 2.27±0.02 | 5.90±2.89 | <0.3 | <12 | 368/167 |
| pn | 0.48±0.01 | $11.17^{+0.04}_{-0.09}$ | $1.11^{+0.08}_{-0.07}$ | $6.40^{+3.87}_{-3.25}$ | <0.3 | <12 | 290/122 |

et al. (2007). The abundances of the low-$kT_e$ component shown by them are as follows: C=0.27, N=0.10, O=0.11, Ne=0.21, Mg=0.17, Si=0.34, S=0.17, Fe(=Ni)=0.20. We fixed the other elements to the solar values. As for the high-$kT_e$ component, the abundance of some elements such as C, N, and O were not determined by freeing their abundances because these emission lines are out of the range of 1.5-5.0 keV. Thus, we set only the abundances of Si and Ar to be free, whereas the other elemental abundances such as O, Ne, Mg, S, and Fe were linked to that of Si by fixed raios calculted from the results of Tsunemi et al. (2007) and Uchida et al. (2009c). We set the abundances of C and N equal to O, Ni equal to Fe, and other elements fixed to their solar values. Other parameters were all free such as $kT_e$, the ionization timescale $\tau$ , and the EM. We fixed the column density $N_{\rm H}$ to be $4.0\times10^{20}{\rm cm}^{-2}$ (Tsunemi et al. 2007). Since the improvement of the statistics of the XIS data is so substantial that the absolute energy uncertainty becomes considerable (measured with the $^{55}$Fe calibration sources is within ±0.2%), we set the parameter of the redshift, $z$, to be free. As a result, the reduced $\chi^2$ value is improved 4.8 to 1.3 by freeing the $z$ parameter and thus the best-fit value of $z$ is $2.98\times10^{-3}$. We also applied the two-component VNEI model for MOS and pn spectra (figure 6.10). The best-fit parameters are shown in Table 6.3. Judging from the fitting results of every detector, the temperature of each component indicates a typical value of the Cygnus Loop (e.g., Tsunemi et al. 2007). Then, we consider the high and the low-temperature component originates from the ejecta and the ISM, respectively. From Figure 6.9 bottom and Figure 6.10, the contribution of the ISM component is quite low at 1.5-5.0 keV and thus we can estimate the Ar abundance derived from the Cygnus Loop ejecta. Table 6.3 shows the value of the Ar abundance is significantly higher than that of the solar value and is consistent with each detector within the margin of the errors. For all of these reasons, we concluded that the Ar He$\alpha$ line was detected for the first time and that we could also estimate the value of the Ar abundance.

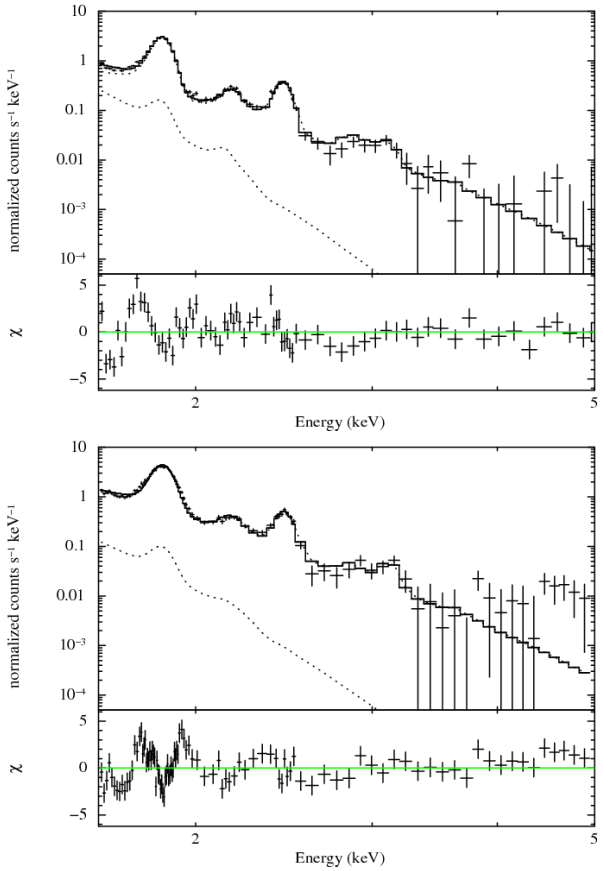


Figure 6.10: 1.5-5.0 keV spectra obtained from all MOS data (top) and pn data (bottom). The spectra are fitted with two-component VNEI model. The residuals are shown in the lower panels.

We also intended to investigate the spatial distribution of Ar using the *Suzaku* XIS data. We divided our FOV into three regions as shown in Figure 6.7. We label the regions surrounded by green, blue, and black lines as Region-A, Region-B, and Region-C, respectively. The spectrum from the Region-C is virtually dominated by the radiation from ISM component, while those of the Region-A and the Region-B are the superposition of both ISM and ejecta components. Figure 6.11 shows 1.5-5.0 keV spectra obtained from Region-A (top), Region-B (middle), and Region-C (bottom). The first two are fitted with the two-component VNEI models, whereas the last one is fitted with the single-component VNEI model. The best-fit parameters are indicated in Table 6.4. Each $\chi^2$ value shows that two-component and single-component VNEI models are statistically acceptable for Region-A/B and Region-C, respectively, while the contribution of the low-temperature component is quite low for the Region-A spectrum. This is simply because the Region-A is located on near the center of the Loop where the ejecta component is considerably

Table 6.4: Spectral parameters inferred from combined XIS data (see Figure 6.11)

| | Ejecta Component | | | | |
|---|---|---|---|---|---|
| | $kT$ [keV] | log $\tau$ | Si | Ar | |
| Region-A | $0.55^{+0.01}_{-0.03}$ | $11.33^{+0.14}_{-0.07}$ | $2.54^{+0.21}_{-0.19}$ | 9.78±3.89 | |
| Region-B | $0.42^{+0.03}_{-0.01}$ | $11.71^{+0.30}_{-0.17}$ | 0.62±0.03 | $3.65^{+1.63}_{-1.38}$ | |
| Region-C | – | – | – | – | |
| | ISM Component | | | | |
| | $kT$ [keV] | log $\tau$ | Si | Ar | $\chi^2$/dof |
| Region-A | $< 0.3$ | $< 12$ | 0.34(fixed) | 1.00(fixed) | 147/158 |
| Region-B | $0.15^{+0.08}_{-0.04}$ | $< 12$ | 0.34(fixed) | 1.00(fixed) | 136/135 |
| Region-C | 0.32±0.01 | $10.97^{+0.03}_{-0.04}$ | $0.32^{+0.02}_{-0.01}$ | $< 0.67$ | 98/74 |

dominant. Both the spectra from Region-A and Region-B show that the Ar abundances is significantly higher than that of the solar value.

### 6.2.3 Discussion

#### Spatial Distribution of Ar

As shown in the previous section, we clearly detected the Ar-K line emission from the Cygnus Loop and concluded that it is originated from the ejecta component. Also, the spectral analysis shows the value of the Ar line emission is prominent especially in the inner regions (Region-A/B) rather than that in the limb region (Region-C).

In order to examine the Ar distribution, we plotted Ar abundances as a function of radius (distance from the geometric center of the Loop) in Figure 6.12. From Figure 6.12, we found that the Ar abundance is significantly higher near the center (Region-A) than at the circumference (Region-B). Furthermore, the Ar abundance at Region-C where the ISM component is dominant is lower than the solar value and we could only determine the upper limit. These results strongly support the Ar emission comes from the ejecta of the Cygnus Loop. We also plotted Si abundances in Figure 6.12 for comparison. It is clear that the distribution of Si appears similar to that of Ar. From the point of view of the nucleosynthesis process, Si, S, and Ar are mostly produced in the same layer of the star before the explosion. Therefore, after the explosion, the ejected elements should show the similar distributions with each other. As for the Cygnus Loop, Uchida et al. (2009c)

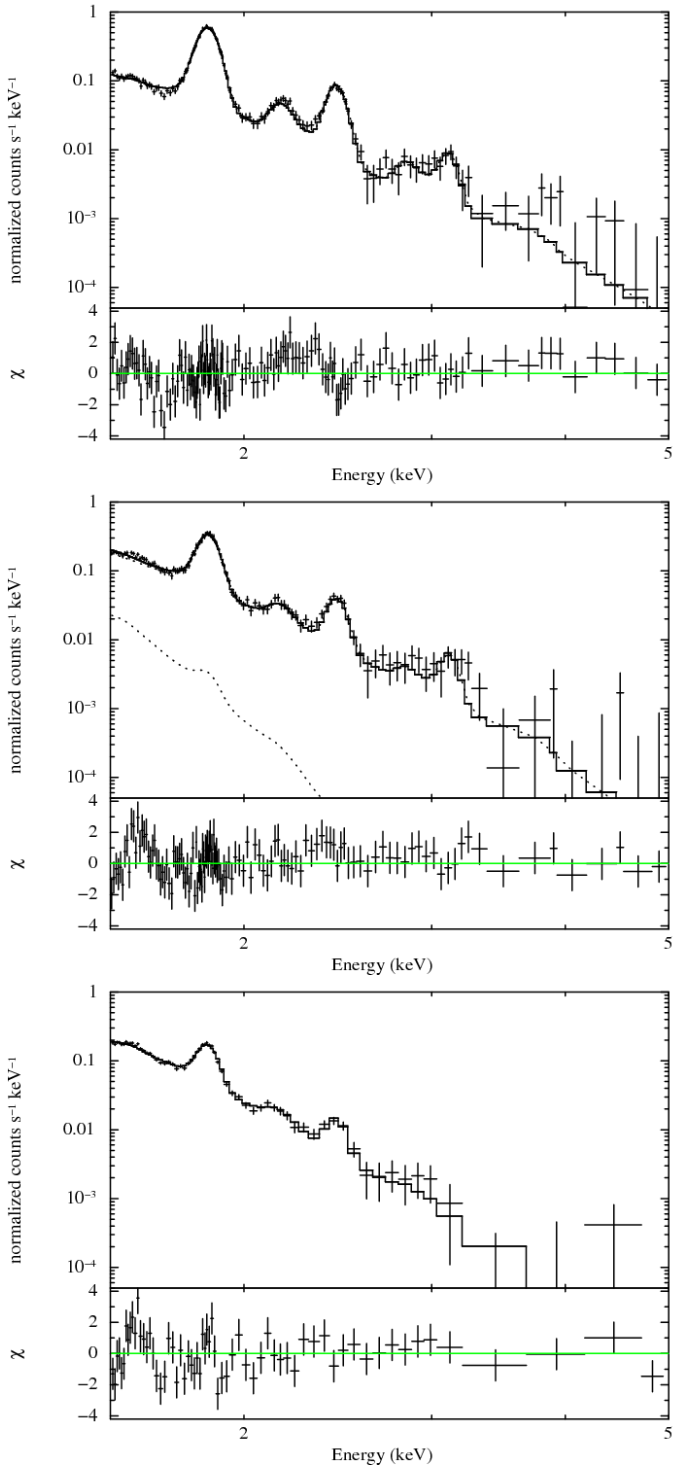


Figure 6.11: 1.5-5.0 keV spectra obtained from Region-A (top), Region-B (middle), and Region-C (bottom). The first two are fitted with two-component VNEI models. The last one is fitted with single-component VNEI model. The residuals are shown in the lower panels.

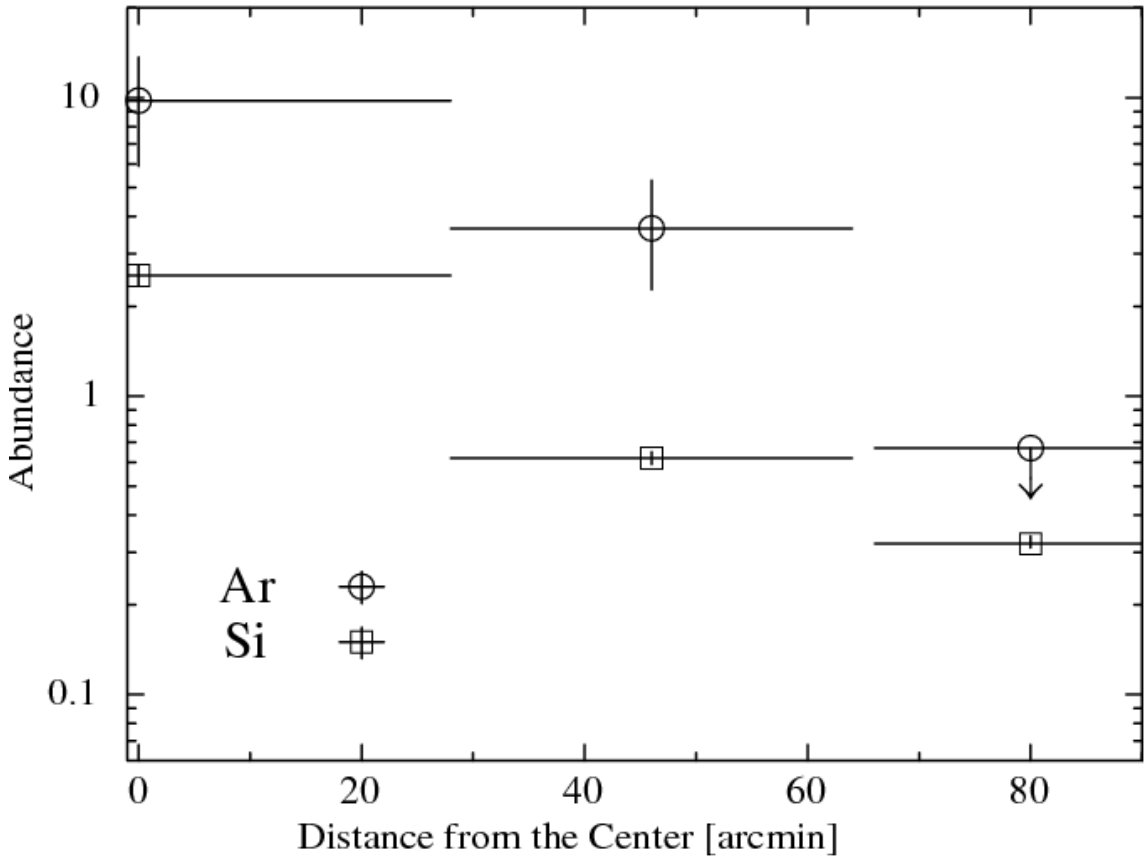


Figure 6.12: Abundance distributions of Ar and Si.

indicated that the ejected Si is concentrated on near the center of the Loop. Thus, it is natural to consider that Ar is also distributed near the center. Due to the lack of the statistics, we could not subdivide our FOV, investigating the spatial distribution in more detail. However, the very least we could conclude is that the Ar emission is originated from the ejecta of the Cygnus Loop and that its distribution shows a central concentration as with the case of Si.

### Estimation of Progenitor Star Mass

From our results, we calculated the number ratios of Ne, Mg, Si, S, Ar, and Fe relative to O of the ejecta component. We plotted them with black line in Figure 6.13. The vertical bars show the uncertainties of the values. We also plotted the core-collapse models (Woosley & Weaver 1995) for various progenitor masses and Type Ia SN models (Iwamoto et al. 1999) for comparison. We found that the calculated values of Ne/O, Mg/O, Si/O, and S/O are all in good agreement with the core-collapse model with the core-collapse model of $12M_{\odot}$ progenitor star. We note that massive stars above $\sim 20M_{\odot}$

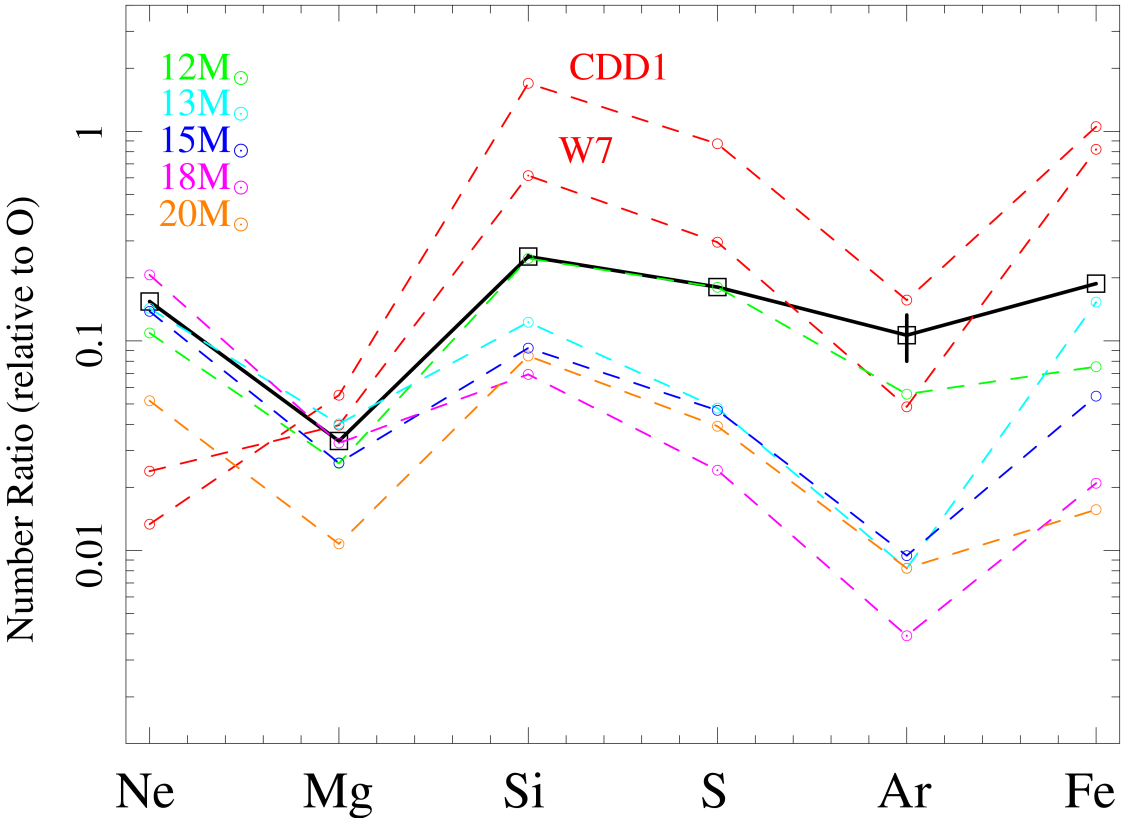


Figure 6.13: Number ratios of Ne, Mg, Si, S, Ar, and Fe relative to O of the high-$kT_e$ component, estimated by the *Suzaku* XIS data (solid black line). Dotted red lines represent the CDD1 and W7 Type Ia models of Iwamoto et al. (1999). Dotted green, light blue, blue, magenta, and orange lines represent core-collapse models with progenitor masses of 12, 13, 15, 18, and $20M_{\odot}$, respectively (Woosley & Weaver 1995).

produce larger amount of O in theory than those of the relatively low-mass stars. In this case, even the values of Si/O and S/O drastically decrease from the results of the Cygnus loop. Therefore, at this point, we confirm that the Cygnus Loop's progenitor mass is more likely to be less than $20M_{\odot}$.

However, the Ar/O ratio is roughly two times higher than that of the $12M_{\odot}$ model and also the Fe/O ratio is a few times higher. Our results suggest that the heavier elements which existed near the stellar core tend to be ejected more by the SN explosion compared with the model. Some previous observations show that the heavy elements of the Cygnus Loop are distributed asymmetrically which may suggest an off-center explosion of the progenitor star (Katsuda et al. 2008a; Kimura et al. 2009; Uchida et al. 2009c). Thus we considered the possibility that an off-center explosion may significantly affect the total amount of the ejected elements.

In the following analysis, we assumed a simple geometrical calculation for the first approximation and thus simulated the total mass of the ejected O, Ar, and Fe. Figure 6.14 shows an example mass fraction models of $^{16}$O, $^{38}$Ar, and $^{56}$Fe in a $15M_{\odot}$ solar-metallicity star against the presupernova radius which takes into account explosive nucleosynthesis and radioactive decay (Umeda & Nomoto 2005; Nomoto et al. 2006; Tominaga et al. 2007). We note that radioactive decays such as $^{56}$Ni$\rightarrow^{56}$Fe are calculated preliminarily in these distributions, therefore, they do not reflect the real elemental distribution inside the star. The vertical line in figure 8 represents a boundary between the ejecta and the central remnant to yield a canonical amount of $^{56}$Ni ($\sim 0.08M_{\odot}$; e.g., 1987A; Blinnikov et al. 2000), which locates at $R_{\rm bound}$ =1600 km in the progenitor star corresponding $1.50M_{\odot}$ in the symmetric case. From Figure 6.14, we assumed a simple geometrical calculation for the first approximation. We attempt slight displacement of the fallback center from the explosion center. The resultant SN yield is an integration of matter outside a fallback sphere with a radius of $R_{\rm bound}$. In this calculation, all stable isotopes were taken into account; for example, the total amount of Fe was obtained by summing the amounts of $^{54}$Fe, $^{56}$Fe, $^{57}$Fe, and $^{58}$Fe. Thus, we obtained the number ratios as the functions of the shift lengths ($L_{\rm shift}$) as shown in Figure 6.15. As a result, the value of Fe/O slightly increases with the displacement of the fallback center, which is qualitatively interpreted that the dense $^{56}$Ni-rich material close to the stellar center can be ejected outside by shifting the fallback sphere. However, the increment of Fe/O is insufficient to explain the observed excess of Fe by considering the simple off-center explosion model.. In order to double the value of Fe/O, we need to shift the explosion center more than $L_{\rm shift} \sim 2 \times 10^3$ km ($\simeq 2R_{\rm bound}$), which cannot be assumed as an approximation for a simple geometrical calculation any more. As for the Ar, the value of Ar/O remains almost unchanged in Figure 6.15 top panel, while enlarged view (Figure 6.15 bottom right) shows rapid decreasing at shift length $L_{\rm shift} > 2.3 \times 10^3$ km. The rapid decreasing of Ar/O is due to the reason that the central core moves to the Ar-rich layer at $L_{\rm shift} > 2.3 \times 10^3$ km. However, the reduction rate is much less than 5% from $L_{\rm shift} = 2.3 \times 10^3$ km to $L_{\rm shift} = 2.5 \times 10^3$ km. In any case, the simple off-center explosion does not explain the excess of the observed Ar/O and Fe/O. We note that the amount of the ejected $^{56}$Ni is highly dependent on the fallback (Figure 6.14), for example, the observed Fe/O is reproduced if the Cygnus Loop yielded $0.1M_{\odot}$ of $^{56}$Ni in which the boundary locates at $R_{\rm bound}$ =1200 km corresponding $1.46M_{\odot}$ in the symmetric case. Therefore the fallback may need to be given more consideration as the cause of the discrepancy between the observed Fe/O and the model. On the other hand, since the Ar-rich layer is located at $\simeq 2R_{\rm bound}$ (Figure 6.14), the value of Ar/O is mostly independent on the position of the mass cut. Most of Si, S,

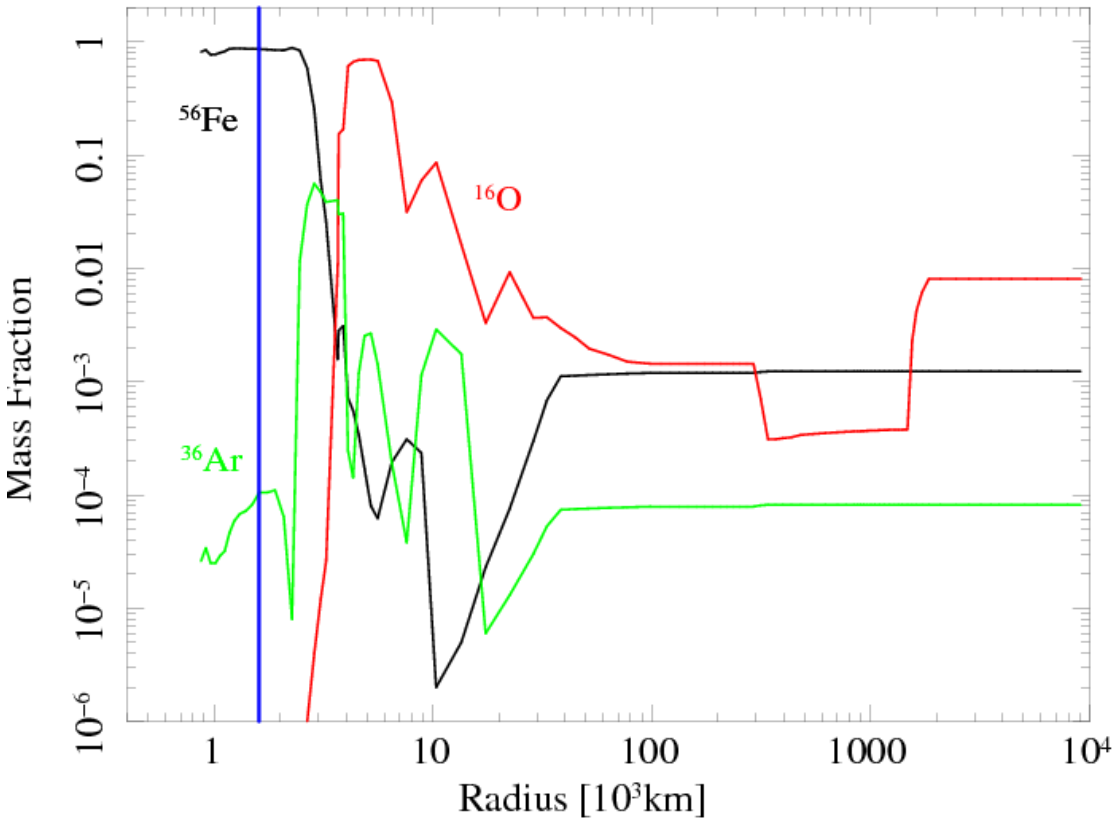


Figure 6.14: Mass fractions of $^{16}$O, $^{38}$Ar, and $^{56}$Fe in a $15M_{\odot}$ star after taking into account the radioactive decays (based on the results of Umeda & Nomoto 2005; Nomoto et al. 2006; Tominaga et al. 2007). The vertical line represents the mass cut of $1.50M_{\odot}$.

and Ar are synthesized in the incomplete Si-burning layer and thus the ratios of Ar/Si and Ar/S are determined mainly by the nuclear reaction rates. Therefore, the ratios should be similar for each theoretical model unless the nuclear reaction rates related to the synthesis of S and Ar are revised. As shown in Figure 6.14, the observed Ar/Si and Ar/S are higher than the theoretically-expected values. There are neither core-collapse models nor Type Ia models which explain these ratios and this point remains controversial.

In summary, our results strongly suggest the Cygnus Loop's origin as a core-collapse SN rather than a Type-Ia SN. We also confirmed that its progenitor mass is less than $20M_{\odot}$ and most likely to be $\sim 12M_{\odot}$. The overabundances of Ar and Fe still remain open questions.

### 6.2.4 Conclusion

We intended to improve a signal-to-noise ratio of the spectrum by using all the available X-ray data. Accordingly, every spectrum obtained from XIS, MOS, and pn shows some

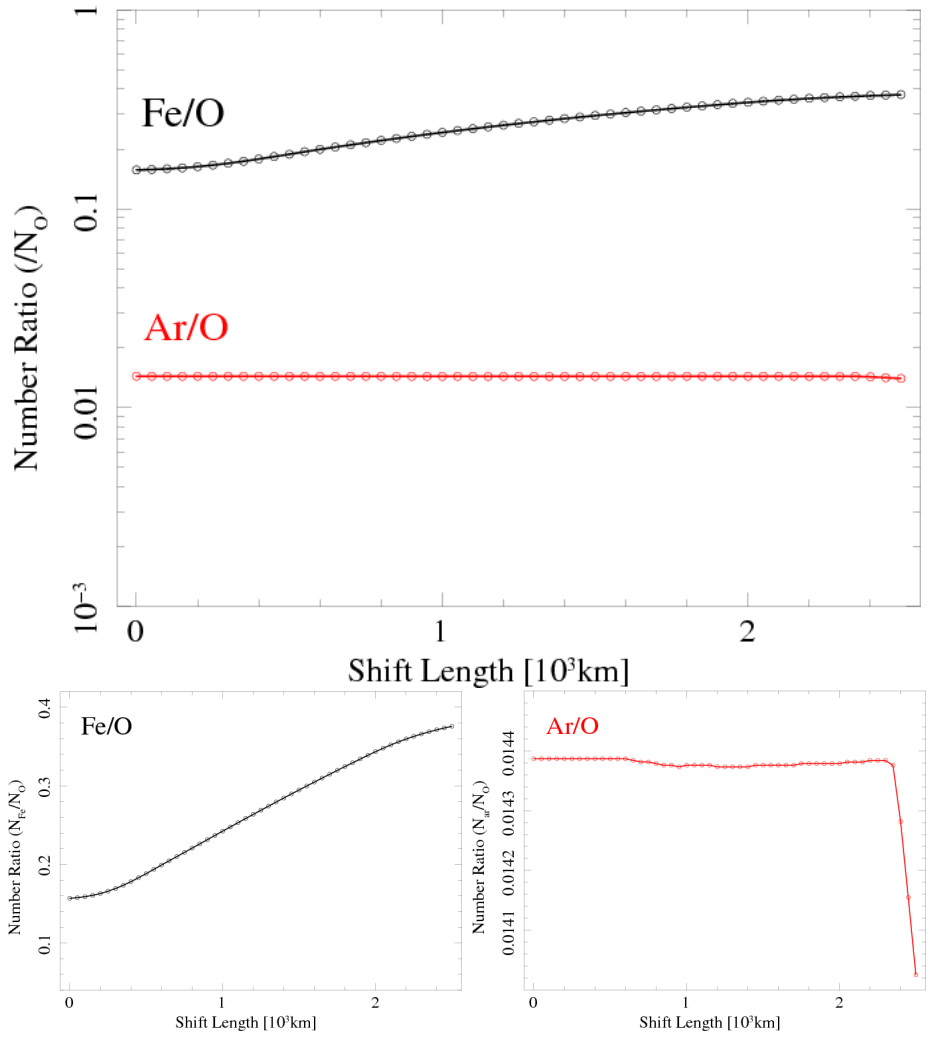


Figure 6.15: Number ratio of each element as a function of shift length. Top panel shows the number ratios of Fe/O (black) and Ar/O (red) in logarithmic scale. Bottom two panels are the enlarged views of the lines of these elements.

line structure around 3.0 keV above the background level. As a result, we concluded that this structure is attributed to S He$\beta$ and Ar He$\alpha$ lines, respectively. The Ar He$\alpha$ line is first detected from the Cygnus Loop and we found that its abundance (7.88±2.19) is significantly higher than that of the solar value. We also showed that the Ar is distributed near the center of the Cygnus Loop and concluded that the observed Ar is originated from the ejecta component of the Loop.

We also calculated the number ratios of Ne, Mg, Si, S, Ar, and Fe relative to O of the ejecta component and compared them with some theoretical models. We found that the calculated values of Ne/O, Mg/O, Si/O, and S/O are all in good agreement with the core-collapse model with the progenitor mass of $12M_{\odot}$, while the Ar/O ratio is roughly two times higher than that of the $12M_{\odot}$ model and also the Fe/O ratio is a few times higher. In order to explain this discrepancy, we considered the possibility that an off-center explosion may significantly affect the total amount of the ejected elements. However, the simple off-center explosion does not explain the excess of the observed Ar/O as well as that of the Fe/O. Although the overabundances of Ar and Fe still remains an open question, our results strongly suggest that the Cygnus Loop's origin is a core-collapse SN rather than a Type-Ia SN.

# Chapter 7

# Discussion

## 7.1 Shell Structure and Surrounding Environment

### 7.1.1 Interaction between Blast Wave and Ambient Medium

The results in Section 5.1 indicate that the Cygnus Loop's south blowout originates from the break of the cavity wall. Section 5.2 and 5.3 suggest such break may also exist in the northern limb or along the line of sight. As for the other cavity-born SNRs, for example, the X-ray morphology of the N132D also shows a "blowout" that closely resembles the Cygnus Loop's blowout region (Chen et al. 2003; Borkowski et al. 2007). We need to consider whether such nonuniformity of the cavity wall is common or not. On the contrary, some limb regions show the evidence of the interaction with the blast wave and dense cloud (Danforth et al. 2001; Patnaude et al. 2002; Levenson et al. 2002; Levenson & Graham 2005). The shell morphologies of such regions have higher surface brightness and concave structures (see Figure 5.19). As mentioned in Section 5.3, we also found such region along the line of sight in the C-shape structure. In this way, we could obtain the information about the surrounding environment of the Cygnus Loop including the line-of-sight structure.

The interaction between the blast wave and the ambient medium is important for investigating the origin of the Galactic cosmic-ray. As for the leptonic process, the detection of synchrotron (non-thermal) X-rays from the young SNRs is a strong evidence that electrons are accelerated up to the *knee* energy, $\sim 10^{15}$ eV ($\sim 10$ TeV) (e.g., Koyama et al. 1995, 1997; Bamba et al. 2005b). On the other hand, recent evidence suggests that the proton is also accelerated at the limb of an young SNR, RCW 86 (Helder et al. 2009). TeV $\gamma$-ray observations of several young shell-type SNRs suggest that protons are accelerated to $\sim 10$ TeV, for example, RX J1713.7-3946 (Enomoto et al. 2002), RX

J0852.0-4622 (Aharonian et al. 2005; Katagiri et al. 2005). The hadronic process can be originated from the decay of neutral pion (pion decay), arising from the collision of the high-energy protons and ISM. As reported by Fukui et al. (2003), there is a clear association with a CO molecular cloud interacting with the RX J1713.7-3946 and its TeV $\gamma$-ray peak, providing the evidence for proton acceleration.

As for the electron acceleration, the SNRs which show synchrotron emissions are all younger ($< 1000$ yr) than the Cygnus Loop and we could not detect the synchrotron X-rays from the Cygnus Loop (Tsunemi et al. 2009). This is because the shock speed of the evolved SNRs is insufficient to provide the accelerated electrons keeping up the synchrotron cooling. However, as for the proton acceleration, recent observations indicate that TeV $\gamma$-ray emissions are detected from some old SNRs. Aharonian et al. (2008) detected the high energy $\gamma$-ray emission coincident with molecular clouds in the W 28 whose age is $\sim 10^5$ yr. Other old SNRs such as G23.3-0.3 (Aharonian et al. 2006) and G8.7-0.1 (Fang & Zhang 2007) are also detected the TeV $\gamma$-ray emission. From a theoretical point of view, Yamazaki et al. (2006) showed that when the SNR age is $\sim 10^5$ yr proton acceleration is efficient enough to emit TeV $\gamma$-rays at the interacting region between the shock and the molecular cloud. Their results also indicate that in the younger SNR ($\sim 10^4$ yr) the X-ray emission is still dominated by the synchrotron radiation rather than the pion decay emission. However, from the observation of the shell-type SNR IC 443, Zhang & Fang (2008) showed the evidence of TeV $\gamma$-ray emission and the correlation between the emitting region and a molecular cloud. The age of the IC 443 is estimated to be $\sim 30,000$ yr (Chevalier 1999), which is close to that of the Cygnus Loop ($\sim 10,000$ yr). Therefore, in the future we may need to consider the possibility of the $\gamma$-ray emission from the Cygnus Loop, particularly focusing on the region where the blast wave interacts with the dense ambient medium.

### 7.1.2 Abundance Inhomogeneity

As shown in Section 5.2, the spectra obtained from the limb regions of the Cygnus Loop are generally well fitted by a single-$kT_e$ VNEI model. This is interpreted as radiation from swept-up ISM or material from the shell created by the progenitor's wind. It is therefore expected that the elemental abundances of the limb spectra reflect those of the ambient medium. However, many previous studies including our observations report on the abundance depletion at the limb of the Cygnus Loop. The problem is why the abundances of the limb regions (except the abundance-enhanced regions) are commonly metal deficient.

We first considered the effect of synchrotron radiation which may lower the apparent

elemental abundances such as C, N, and O. However, we found that there is no evidence of such non-thermal emission. In fact, the X-ray synchrotron emission is not expected for the relatively low shock velocities in the Cygnus Loop (Zirakashvili & Aharonian 2007). We also considered the effect of the resonance-scattering. However, previous calculation shows that the O abundance is underestimated by a factor of 20-40% at the northeastern limb and this result is not sufficient to account for the abundance depletion observed (Miyata et al. 2008). Thus, we consider another promising possibility, the underestimation of the bremsstrahlung continuum due to a nitrogen enhanced medium. As mentioned in Section 2.3, the origin of the Cygnus Loop is most likely to be a 12-15$M_{\odot}$ type B0 star. Such kind of star may create a nitrogen-rich stellar wind and form a cavity wall around the star. From the previous observations, we confirmed that the spectra obtained from limb regions come from the shock-heated cavity material. Therefore, if the blast wave interacts with the cavity wall under a nitrogen-rich environment, the underestimation of the continuum is considerable. This is simply because the intensity of the bremsstrahlung significantly depends on the atomic number of ion ($\propto n_e n_i Z^2$, where $n_e$ and $n_i$ represent a density of electron and ion, $Z$ is an atomic number of ion). In a nitrogen enhanced medium, the additional continuum derived from the bremsstrahlung becomes considerable ($14 n_{\rm H} \propto 1 n_{\rm N}$). Thus, we consider the additional component from a nitrogen enhanced medium may lower the apparent elemental abundances. In order to verify our hypothesis, we need to estimate the nitrogen abundance at the limb of the Loop with better spectral resolution. We proposed to observe the Cygnus Loop's thin filament with the RGS for the *XMM-Newton* Ninth Announcement of Opportunity (AO-9). In the future, we may need to observe the Cygnus Loop with a microcalorimeter such as SXS (Soft X-ray Spectrometer) which will be instrumented on the ASTRO-H[1].

## 7.2 Ejecta and Progenitor Star

### 7.2.1 Asymmetric Explosion

In Section 6.1, the EM distribution of Fe and Si in Figure 6.5 suggests that the SN explosion of the Cygnus Loop occurred asymmetrically. From a theoretical point of view, it is becoming clearer that any scenario considering a simple spherically-symmetric simulation does not cause a SN explosion. The neutrino heating is important for the explosion mechanism because a stalled bounce shock is reenergized by neutrino energy (e.g., Behte & Wilson 1985; Wilson & Mayle 1993; Burrows et al. 1995; Liebendörfer et al. 2001).

[1]http://astro-h.isas.jaxa.jp/index.html.ja

However, there are no calculations which produce enough energy to explode a star by heated shock. For example, Kitaura et al. (2006) assumed a spherical symmetry model of $1.38M_{\odot}$ O-Ne-Mg core of the $8.8M_{\odot}$ star (Nomoto & Hashimoto 1988) and simulated a delayed neutrino-driven explosion. The results indicate that the explosion energy is an order of $10^{50}$ ergs. As shown in Section 2.1, the required explosion energy is at least $10^{51}$ ergs. Such spherical simulation suggests that an additional condition is needed to explode a star.

Some recent observations show the evidences for the asymmetric SN explosion. The most prominent example is the case of a supernova, 1987A which appeared in Large Magellanic Cloud (LMC) on 23, February, 1987 (e.g., Menzies et al. 1987). Earlier observations of 1987A suggests an asymmetric explosion by polarization measurements (Jeffery 1987) and shapes of the spectral lines (Larson et al. 1987). Today we can clearly see the asymmetric morphology from the optical image of the 1987A SNR (e.g., Michael et al. 2003). From the spectropolarimetry, some other SNe also show the evidences for asymmetric explosion: SN 2004dj (Type II; Leonard et al. 2006), SN 1996cb, SN 1997X and SN 1998S (Type IIB, Ic, and IIn, resp.; Wnag et al. 2001), and SN 2002ap (Type Ic; Kawabata et al. 2002; Leonard et al. 2002; Wnag et al. 2003).

Recent studies of extragalactic SNe suggest that all core-collapse SNe are commonly asymmetric explosions (Maeda et al. 2008). As a result, in order to explain the observational evidences of their asymmetry, some theoretical models involved some asymmetrical effects, for example, a jet-like explosion (Ishikawa et al. 1991) and a Rayleigh-Taylor instability in the presupernova structure (Arnett et al. 1989). More generally, recent simulations show that the standing accretion shock has been recognized to be unstable to the non-radial deformation (Standing Accretion Shock Instability (SASI); Blonding et al. 2003). Although SASI-aided simulation of $11.2M_{\odot}$ progenitor star (Woosley et al. 2002) produced only $\sim 10^{49}$ ergs (Buras et al. 2006), Burrows et al. (2006) took into account the advective-acoustic oscillation in the $11M_{\odot}$ progenitor simulation and showed that the acoustic power is sufficient to drive the explosion.

Based on SASI model, Burrows et al. (2007) also calculated the inner ejecta asymmetries of 2:1 or 3:1. We note that their result is consistent with the Fe and Si distributions of the Cygnus Loop as already shown by Katsuda et al. (2008b). Also, as shown in Section 6.1.3, we found that the metal center is separated from the geometric center by $25'$ toward the south. Assuming 540 pc for the Cygnus Loop's distance, the center of the ejecta should have moved $\sim 3.9$ pc in 10,000 yr, hence $\sim 390$ km s$^{-1}$ for the proper velocity. On the other hand, Maeda et al. (2007) observed the late-phase nebular spectra of SN 2005bf (Type Ib) and concluded the center-of-mass velocity of the ejected elements

to be $< 2,000\,\mathrm{km\ s^{-1}}$ judging from the blueshift of their emision lines. If we assume their result as an upper limit of the asymmetrically-ejected element, it is reasonable to consider that the Cygnus Loop's Fe and Si were ejected southward. In summary, our results, the ejecta distributions of the Cygnus Loop, support the need for the asymmetric effect from the standpoint of the X-ray observation of an evolved SNR.

### 7.2.2 Origin of the Cygnus Loop

As shown in Chapter 6, the origin of the Cygnus Loop is most likely to be a core-collapse SN explosion of $12M_{\odot}$ star. However, two problems, the excess of the observed Ar and Fe abundances and undetected compact star, still remain open questions.

In Section 6.2, we considered a simple off-center explosion model in order to explain the excess of Ar and Fe. The result indicates that it is insufficient to explain the observed excess by considering the off-center model. Alternatively, looking at the EM of Fe, the total amount of Fe is highly dependent on the position of the mass radius, which may explain the discrepancy between our result and the model. Furthermore, our FOV does not cover the entire Cygnus Loop. O, Ne, and Mg distributions in Figure 6.5 suggest that they exist more outside our FOV. In that case, the ratios of Ne/O and Mg/O (Figure 6.13) remain unaltered while those of Fe/O and Ar/O may decrease. In any case, it is worthwhile to expand the observing region outward. We have a plan to observe the unexplored regions in the Cygnus Loop with *Suzaku* later this year (*Suzaku* AO4), which will be clarify the whole picture of the elemental distributions.

The other problem is that the compact star such as neutron star have never been detected in the Cygnus Loop (Kaplan et al. 2006). As shown in Section 6.2, the origin of the Cygnus Loop is likely to be a relatively low-mass ($< 20M_{\odot}$) star. All core-collapse SNe should create a compact star after the explosion because the bounce in the stellar core is necessary to explode the star. Moreover our result in a low-mass progenitor star strongly suggests that the compact star is not a black hole but rather a neutron star (or pulsar). Therefore, considering a cooling curves of the pulsars (Lattimer & Prakash 2004), the pulsar should be still observable in X-ray in the Cygnus Loop as is the case with the Vela pulsar (Mangano et al. 2005) whose age ($\sim 11,400\,\mathrm{yr}$; Taylor et al. 1993) is comparable to that of the Cygnus Loop. Thus, we consider the possibility that the pulsar was kicked out of the Cygnus Loop. The average pulsar velocities are in the range of 200-500 km $\mathrm{s^{-1}}$. However, some observations discovered the high-velocity pulsars whose velocities are more than $1000\,\mathrm{km\ s^{-1}}$ (e.g., Lyne & Lorimer 1994). For example, Winkler & Petre (2007) measured the transverse velocity of the neutron star RX J0822-4300 (associated with the Puppis A SNR) to be $\sim 1600\,\mathrm{km\ s^{-1}}$. If this value is an upper limit of the

velocity of the kicked pulsar, the Cygnus Loop's pulsar should be located within a radius of $\sim 16\,\mathrm{pc}$ from the geometric center (assuming $\sim 10,000$ yr). In this case, the pulsar could be located outside of the Cygnus Loop. We note that the high-velocity pulsar is related to the asymmetric explosion. For example, Scheck et al. (2004, 2006) simulated the asymmetric explosion based on the SASI and calculated the velocity of the neutron star to be more than $1000\,\mathrm{km\ s^{-1}}$. The result also indicates that the kicked neutron star moves in the opposite direction of the ejecta. As for the RX J0822-4300, Katsuda et al. (2008d) showed that the ejecta of the Puppis A is moving in the opposite direction of the RX J0822-4300, which is consistent with the result of Scheck et al. (2006). If the same mechanism is applicable for the case of the Cygnus Loop, we should search a neutron star in the northeast rather than in the Fe-rich southwest. However, another theoretical model based on the neutrino-driven mechanism suggests that the motion of the ejecta is in the same direction of the neutron star (Fryer & Kusenko 2006). Therefore, the pulsar search around the Cygnus Loop is important not only to determine the SN type but also to put restrictions on the theoretical model of the asymmetric explosion.

Although the above problems still remain, our current conclusion is that the origin of the Cygnus Loop is most likely to be a core-collapse cavity SN explosion of $\sim 12 M_{\odot}$ star.

# Chapter 8

# Conclusions and Future Prospects

We have observed the Cygnus Loop in X-ray with *XMM-Newton* (9 pointings) and *Suzaku* (32 pointings) between 2002 and 2008. We investigated the plasma structure mainly based on the spectral analyses which clearly distinguished between the contribution from the ISM and that from the ejecta.

Conclusions are summarized below.

- *Blowout Region* (Section 5.1)
  - From the X-ray study of the south blowout region, there was no evidence of the extra SNR.
  - The X-ray shell is thin in the blowout region, which suggests the origin of the blowout can be explained as a breakout into a lower density cavity material.
- *Nothern Limb* (Section 5.2)
  - The abundances at the outer edge of the northern limb are consistent with those of the surrounding ISM.
  - The other limb spectra wholly show the lower abundances compared with those of the ISM.
  - From a morphological point of view, the blast waves in the abundance-enhanced regions are now proceeding into the outside of the cavity wall and begin to interact with the surrounding ISM.
- *Whole Picture of Shell Structure* (Section 5.3)
  - From the standpoint of the X-ray spectral analysis, we support the origin of the Cygnus Loop is a cavity explosion.

  - The density of the surrounding cavity wall is lacking in uniformity. For example, we showed the evidence of the line-of-sight cavity wall's break at the west of the center in addition to the south blowout.
  - The density of the surrounding material gradually decreases from the northeast to the southwest.

- *Ejecta Distribution* (Section 6.1)
  - The high-temperature component of the X-ray spectra originates form the ejecta of the progenitor star.
  - The ejecta distributions of the heavy elements reflect the elemental distribution, so-called "onion-like structure" inside the presupernova star; Si and Fe concentrate on the center while Mg is distributed outside of the center.
  - The center of the Si and Fe distributions is separated from the geometric center by $25'$ toward the south, which may suggest an asymmetric explosion.

- Ar *Line Emission* (Section 6.2)
  - The Ar-K line emission was detected from the Cygnus Loop for the first time.
  - The observed Ar originates from the ejecta and it is distributed more near the center.

- *Origin of the Cygnus Loop*
  - The observed values of Ne/O, Mg/O, Si/O, and S/O are all in good agreement with the core-collapse model with the progenitor mass of $12M_{\odot}$, while the Ar/O ratio is roughly two times higher than that of the $12M_{\odot}$ model and also the Fe/O ratio is a few times higher.
  - The results strongly suggest the Cygnus Loop's origin as a core-collapse SN rather than a Type-Ia SN and that its progenitor mass is less than $20M_{\odot}$, most likely to be $\sim 12M_{\odot}$.

The remaining main problems and the future prospects are summarized below.

- **Abundance Depletion:** It is still unclear why the abundances of the limb spectra except the abundance-enhanced regions are commonly metal deficient.
  - One of the promising possibilities is the underestimation of the bremsstrahlung continuum due to a nitrogen enhanced medium. The *XMM-Newton* RGS and ASTRO-H SXS in the future may be helpful due to their high energy resolutions.
- **Overabundances of Some Elements:** While The Cygnus Loop's origin is most likely to be a core-collapse SN, the observed Ar/O and Fe/O are higher than any theoretically-expected values of the core-collapse model.
  - This problem may be partly because our FOV does not cover the entire region of the Cygnus Loop. *Suzaku* AO4 is planned to observe the unexplored regions and will be clarify the whole picture of the elemental abundances and distributions.
  - In addition, improved statistics enables us to determine the abundance of Ar (and also possibly Ca) more accurately, which makes it possible to put restrictions on the SN type and progenitor mass of the Cygnus Loop more strictly.
- **Undetected Compact Source:** Another problem is that the compact source such as neutron star have never been detected in the Cygnus Loop before.
  - If the Cygnus Loop originates from the core-collapse SN of the less than $20M_{\odot}$ star, the neutron star (or pulsar) should be detected. Considering the possibility that the pulsar kicked out of the Cygnus Loop, we should extend the observing region outward to search for the pulsar.

# Acknowledgement

First of all, I am deeply grateful to Prof. Hiroshi Tsunemi for his continuous guidance and warm encouragement through my five years of the graduate course. I also owe a very important debt to Dr. Satoru Katsuda for invaluable guidances, comments, and discussions. I also apprecitate Profs. Koji Mori and Kiyoshi Hayashida for careful reading of this thesis and useful comments. I would like to thank Drs. Emi Miyata, Ken'ichi Torii, Masaaki Namiki, Naohisa Anabuki, Hideki Ozawa, and Hiroshi Nakajima for their valuable comments and advice. I also thank many other members of the X-ray astronomy group in Osaka University.

I wish to thank Prof. Jacco Vink and his students for many useful discussions and their hospitality at Utrecht University.

Finally, I deeply appreciate the supports of all the people in Osaka University and my family.

This study is supported by JSPS Research Fellowship for Young Scientists.

# References


Aharonian F., et al. 2005, *Astron. Astrophys. Letters*, 437, L7

Aharonian F., et al. 2006, *Astron. Astrophys.*, 636, 777

Aharonian F., et al. 2008, *Astron. Astrophys.*, 481, 401

Anders, E., & Grevesse, N. 1989, *Geochim. Cosmochim. Acta*, 53, 197

Arnaud, K. A. 1996, *in ASP Conf. Ser. 101, Astronomical Data Analysis Software and Systems V, ed. G. H. Jacoby & J. Barnes* (San Francisco: ASP), 17

Arnett, W. D. 1969, *Astrophys. Space Science*, 5, 180

Arnett, D., Fryxell, B., & Mueller, E. 1989, *Astrophys. J. Letters*, 341, L63

Aschenbach, B., & Leahy, D. A. 1999, *Astron. Astrophys.*, 341, 602

Baade, F., & Zwicky, F. 1934, *Proc. Natl. Acad. Sci.*, 20, 254

Bamba, A., Yamasaki, R., Yoshida, T., Terasawa, T., & Koyama, K. 2005a, *Astrophys. J.*, 621, 793

Bamba, A., Yamasaki, R., & Hiraga, J. S. 2005b, *Astrophys. J.*, 632, 294

Bautz, M. W., et al. 1998, *Proc. SPIE*, 3444, 210

Beehte, H. A., & Wilson, J. R. 1985, *Astrophys. J.*, 295, 14

Blair, W. P., Long, K. S., Vancura, O., & Holberg, J. B. 1991, *Astrophys. J.*, 374, 202

Blair, W. P., Sankrit, R., & Raymond, J. C. 2005, *Astron. J.*, 129, 2268

Blinnikov, S., Lundqvist, P., Bartunov, O., Nomoto, K., & Iwamoto, K. 2000, *Astrophys. J.*, 532, 1132

Blonding, J. M., Mezzacappa, A., & DeMarino, C. 2003 *Astrophys. J.*, 584, 971

Borkowski, K. J., Lyerly, W. J., & Reynolds, S. P. 2001, *Astrophys. J.*, 548, 820

Borkowski, K. J., Hendrick, S. P., & Reynolds, S. P. 2007, *Astrophys. J. Letters*, 671, L45

Braun, E., & Strom, R. G. 1986, *Astron. Astrophys.*, 164, 208

Buras, R., Rampp, M., Janka, H.-Th., & Kifonidis, K. 2006, *Astron. Astrophys.*, 447, 1049

Burrows, A., Livne, E., Dessart, L., Ott, C. D., & Murphy, J., 2006, *Astrophys. J.*, 640, 878

Burrows, A., Livne, E., Dessart, L., Ott, C. D., & Murphy, J., 2007, *Astrophys. J.*, 655, 416

Burke, B. E., et al. 1998, *IEEE Trans. Nucl. Sci.*, 41, 375

Burrows, A., Hayes, J., & Fryxell, B. A. 1995, *Astrophys. J.*, 450, 830

Cartledge, S. I. B., Lauroesch, J. T., Meyer, D. M., & Sofia, U. J. et al. 2004, *Astrophys. J.*, 613, 1037

Chen, Y., Zhang, F., Williams, R. M., & Wang, Q. D. 2003, *Astrophys. J.*, 595, 227

Chevalier, R. A. 1982, *Astrophys. J. Letters*, 259, L85

Chevalier, R. A. 1999, *Astrophys. J.*, 511, 798

Cioffil, D. F., McKee, C. F., & Bertschinger, E. 1988, *Astrophys. J.*, 334, 252

Danforth, C. W., Blair, W. P., & Raymond, J. C. 2001, *Astron. Astrophys.*, 122, 938

Enomoto, R., et al. 2002, *Nature*, 416, 823

Falle, S. A. E. G., & Garlick, A. R. 1982, *Monthly Notices Roy. Astron. Soc.*, 201, 635

Fang, J., & Zhang, L. 2007, *Monthly Notices Roy. Astron. Soc.*, 384, 1119

Ferreira, S. E. S., & de Jager, O. C. 2008, *Astron. Astrophys.*, 478, 17

Filippenko, A. V., Porter, A. C., & Sargent, W. L. W. 1990, *Astron. J.*, 100, 1575

Filippenko, A. V. 1997, *Astron. Astrophys.*, 35, 309

Fryer, C. L., & Kusenko, A. 2006, *Astrophys. J. Suppl.*, 163, 335

Fujimoto, R., et al. 2007, *Publ. Astron. Soc. Japan*, 59, S133

Fukui, Y., et al. 2003, *Publ. Astron. Soc. Japan Letters*, 55, L61

Garmire, G. P., et al. 1992, in AIAA, *Space Programs and Technologies Conference* (Paper 92-1473) (New York: AIAA)

Gorenstein, P., Harris, B., Gursky, H., Giacconi, R., Novick, R., & vanden Bout, P. 1971, *Science*, 172, 369

Green, D. A. 1986, *Monthly Notices Roy. Astron. Soc.*, 218, 606

Green, D. A. 1990, *Astron. J.*, 100, 1927

Green, D. A., & Stephenson, E. R. 2003, *in Supernovae and gammaray bursters, ed. K. Weiler, Lect. Notes Phys.*, 598 (Berlin, New York: Springer), 7

Green, D. A. 2009, *Bulletin of the Astronomical Society of India*, 37, 45

Hatsukade, I. & Tsunemi, H. 1990, *Astrophys. J.*, 362, 566

Helder, E. A., Vink, J., Bassa, C. G., Bamba, A., Bleeker, J. A. M., Funk, S., Ghavamian, P., van der Heyden, K. J., Verbunt, F., & Yamazaki, R. 2009, *Science*, 325, 719

den Herder, J. W., et al. 2001, *Astron. Astrophys.*, 365, L7

Hester, J. J., & Cox, D. P. 1986, *Astrophys. J.*, 300, 675

Hester, J. J., Raymond, J. C., & Blair, W. P. 1994, *Astrophys. J.*, 420, 721

Hoyle, F., & Fowler, W. A. 1960, *Astrophys. J.*, 132, 565

Hubble, E. P. 1937, *Carnegie Inst. Washington Yearb.*, 36, 189

Iben, I. Jr. & Tutukov, A. V. 1984, *Astrophys. J. Suppl.*, 54, 335

Inoue, H., Koyama, K., Matsuoka, M., Ohashi, T., Tanaka, Y., & Tsunemi, H. 1980, *Astrophys. J.*, 238, 886

Ishikawa, S., Yamada, S., Kiguchi, M., & Sato, K. 1991, *Astron. Astrophys.*, 258, 415

Ishisaki, Y., et al. 2007, *Publ. Astron. Soc. Japan*, 59, S113

Iwamoto, K., Brachwitz, F., Nomoto, K., Kishimoto, N., Umeda, H., Hix, W. R., & Thielemann, F.-K. 1999, *Astrophys. J. Suppl.*, 125, 439

Jansen, F., et al. 2001, *Astron. Astrophys.*, 365, L1

Jeffery, D. J. 1987, *Nature*, 329, 419

Jun, B.-I., & Norman, M. L. 1996, *Astrophys. J.*, 465, 800

Jun, B.-I., & Norman, M. L. 1996, *Astrophys. J.*, 472, 245

Kahn, S. M., Charles, P. A., Bowyer, S., & Blissett, R. J. 1980, *Astrophys. J. Letters*, 242, L19

Kaplan, D. L., Gaensler, B. M., Kulkarni, S. R., & Slane, P. O. 2006, *Astrophys. J. Suppl.*, 163, 344

Katagiri H., et al. 2005, *Astrophys. J. Letters*, 619, L163

Katsuda, S., Tsunemi, H., Miyata, E., Mori, K., Namiki, M., Nemes, N. & Miller, E. D. 2008a, *Publ. Astron. Soc. Japan*, 60, S107

Katsuda, S., Tsunemi, H., Uchida, H., Miyata, E., Nemes, N., Miller, E. D., Mori, K., & Hughes, J. P. 2008b, *Publ. Astron. Soc. Japan*, 60, S115

Katsuda, S., Tsunemi, H., Kimura, M. & Mori, K. 2008c, *Astrophys. J.*, 680, 1198

Katsuda, S., Mori, K., Tsunemi, H., Park, S., Hwang, U., Burrows, D. N., Hughes, J. P., & Slane, P. O. 2008d, *Astrophys. J.*, 678, 297

Kawabata, K. S., et al. 2002, *Astrophys. J. Letters*, 580, L39

Keen, N. J., Wilson, W. E., Haslam, C. G. T., Graham, D. A., & Thomasson, P. 1973, *Astron. Astrophys.*, 28, 197

Kelley, R. L. 2007, *Publ. Astron. Soc. Japan*, 59, S77

Khokhlov, A. M. 1991, *Astron. Astrophys.*, 245, 114

Kimura, M., Tsunemi, H., Katsuda, S. & Uchida, H. 2009, *Publ. Astron. Soc. Japan*, 61, S137

Kitaura, F. S., Janka, H.-Th., & Hillebrandt, W. 2006, *Astron. Astrophys.*, 450, 345

Kokubun, M., et al. 2007, *Publ. Astron. Soc. Japan*, 59, S53

Koyama, K., Petre, R., Gotthelf, E. V., Hwang, U., Matsuura, M., Ozaki. M., & Holt, S. S. 1995, *Nature*, 378, 255

Koyama, K., Kinugasa, K., Matsuzaki, K., Nishiuchi, M., Sugizaki, M., Torii, K., Yamauchi, S., & Aschenbach, B. 1997, *Publ. Astron. Soc. Japan*, 49, L7

Koyama, K. et al. 2007, *Publ. Astron. Soc. Japan*, 59, S221

Krause, O., Birkmann, S. M., Usuda, T., Hattori, T., Goto, M., Rieke, G. H., & Misselt, K. A. 2008, *Science*, 320, 1195

Larson, H. P., Drapatz, S., Mumma, M. J., Weaver, H. A. 1987, *Proc. ESO Workshop on the SN 1987A*, 147

Lattimer, J. M., & Prakash, M. 2004, *Science*, 304, 536

Leahy, D. A. 2004, *Monthly Notices Roy. Astron. Soc.*, 351, 385

Leonard, D. C., Filippenko, A. V., Chornock, R., & Foley, R. J. 2001, *Publ. Astron. Soc. Pacific*, 114, 1333

Leonard, D. C., et al. 2006, *Nature*, 440, 505

Levenson, N. A., Graham, J. R., & Walters, J. L. 1997, *Astrophys. J.*, 484, 304

Levenson, N. A., Graham, J. R., Keller, L. D., & Richter, M. J. 1998, *Astrophys. J. Suppl.*, 118, 541

Levenson, N. A., Graham, J. R. & Snowden, S. L. 1998, *Astrophys. J.*, 526, 874

Levenson, N. A., Graham, J. R., & Walters, J. L. 2002, *Astrophys. J.*, 576, 798

Levenson, N. A., & Graham, J. R. 2005, *Astrophys. J.*, 622, 366

Liebendörfer, M., Mezzacappa, A., Thielemann, F.-K., Messer, O. E., Hix, W. R., & Bruenn, S. W. 2001, *Phys. Rev. D*, 63, 10

Lundmark, K. 1921, *Publ. Astron. Soc. Pacific*, 33, 225

Lyne, A. G., & Lorimer, D. R. 1994, *Nature*, 369, 127

Maeda, K., Tanaka, M, Nomoto, K, Tominaga, N., Kawabata, K., Mazzali, P. A., Umeda, H., Suzauki, T., & Hattori, T. 2007, *Astrophys. J.*, 666, 1069

Maeda et al. 2008, *Science*, 319, 1220

Mangano, V., Massaro, E., Bocchino, F., Mineo, T., & Cusumano, G. 2005, *Astron. Astrophys.*, 436, 917

Mason, K. O., et al. 2001, *Astron. Astrophys.*, 365, L36

McKee, C. F. 1974, *Astrophys. J.*, 188, 335

McKee, C. F., & Ostriker, J. P. 1977, *Astrophys. J.*, 218, 148

McCray, R., & Snow, T. P., Jr. 1979, *Ann. Rev. Astron. Astrophys.*, 17, 213

Menzies, J. W., et al. 1987, *Monthly Notices Roy. Astron. Soc.*, 227, 39

Michael, E., et al. 2003, *Astrophys. J.*, 593, 809

Minkowski, R. 1941, *Publ. Astron. Soc. Pacific*, 53, 224

Minkowski, R. 1958, *Rev. Modern Phys.*, 30, 1048

Mitsuda, K., et al. 2007, *Publ. Astron. Soc. Japan*, 59, S1

Miyata, E., Tsunemi, H., Pisarki, R., and Kissel, S. E. 1994, *Publ. Astron. Soc. Japan*, 46, L101

Miyata, E., Tsunemi, H., Kohmura, T., Suzuki, S., & Kumagai, S. 1998, *Publ. Astron. Soc. Japan*, 50, 257

Miyata, E., & Tsunemi, H. 1999, *Astrophys. J.*, 525, 305

Miyata, E., Ohta, K., Torii, K., Takeshima, T., Tsunemi, H., Hasegawa, T., & Hashimoto, Yasuhiro. 2001, *Astrophys. J.*, 550, 1023

Miyata, E., Katsuda, S., Tsunemi, H., Hughes, J. P., Kokubun, M., & Poter, F. S. 2007, *Publ. Astron. Soc. Japan*, 59, S163

Miyata, E., Masai, K., & Hughes, J. P. 2008, *Publ. Astron. Soc. Japan*, 60, 521

Morrison, R. & McCammon, D. 1983, *Astrophys. J.*, 270, 119

Nemes, N., Tsunemi, H., & Miyata, E. 2008, *Astrophys. J.*, 675, 1293

Nomoto, K. 1982, *Astrophys. J.*, 257, 780

Nomoto, K., Thielemann, F.-K., & Yokoi, K. 1984, *Astrophys. J.*, 286, 644

Nomoto, K., & Hashimoto, M. 1988, *Phys. Rep.*, 163, 13

Nomoto, K., Tominaga, N., Umeda, H., Kobayashi, C., & Maeda, K. 2006, *Nucl. Phys. A*, 777, 424

Oort, J. H. 1946, *Monthly Notices Roy. Astron. Soc.*, 106, 159

Patnaude, D. J., Fesen, R. A., Raymond, J. C., Levenson, N. A., Graham, J. R., & Wallance, D. J. 2002, *Astron. J.*, 124, 2118

Prigozhin, G., Burke, B., Bautz, M., Kissel, S., LaMarr, B. 2008, *IEEE Transactions on Electron Devices*, 55, 2111

Raymond, J. C., Ghavamian, P., Sankrit, R., Blair, W. P., & Curiel, S., 2003, *Astrophys. J.*, 584, 770

Read, A. M., & Ponman, T. J. 2003, *Astron. Astrophys.*, 409, 395

Reynolds, S. P., Borkowski, K. J., Green, D. A., Hwang, U., Harrus, I., & Petre, R. 2008, *Astrophys. J. Letters*, 680, L41

Rho, J., & Petre, R. 1998, *Astrophys. J.*, 503, L167

Saio, H., & Nomoto, K. 1985, *Astron. Astrophys.*, 150, L21

Savage, B. D., & Sembach, K. R. 1996, *Ann. Rev. Astron. Astrophys.*, 34, 279

Scheck, L., Plewa, T., Janka, H.-Th., Kifonidis, K., & Müller, E. 2004, *Phys. Rev. Letters*, 92, 011103

Scheck, L., Janka, H.-Th., Kifonidis, K., & Müller, E. 2006, *Astron. Astrophys.*, 457, 963

Sedov, L. I. 1959, *Similarity and Dimensional Methods in Mechanics, 10th ed.* (New York: Academic Press)

Serlemitsos, P., et al. 2007, *Publ. Astron. Soc. Japan*, 59, S9

Seward, F. D., & Wang, Z.-R. 1988, *Astrophys. J.*, 332, 199

Shklovskii, I. S. 1962, *Soviet Astronomy*, 6, 162

Shull, P., Jr., & Hippelein, H. 1991, *Astrophys. J.*, 383, 714

Strüder, L., et al. 2001, *Astron. Astrophys.*, 365, L18

Sugizaki, M., Mitsuda, K., Kaneda, H., Matsuzaki, K., Yamaguchi, S., & Koyama K. 2001, *Astrophys. J.*, 134, 77

Sun X. H., Reich, W., Han, J. L., Reich, P., & Wielebinski, R. 2006, *Astron. Astrophys.*, 447, 937

Tammann, G. A., Löffler, W., & Schröder, A. 1994, *Astrophys. J. Suppl.*, 92, 487

Takahashi, T., et al. 2007, *Publ. Astron. Soc. Japan*, 59, S35

Taylor, J. H., Manchester, R. N., & Lyne, A. G. 1993, *Astrophys. J. Suppl.*, 88, 529

Thielemann, F.-K., Nomoto, K., & Hashimoto, M. 1996, *Astrophys. J.*, 460, 408

Tominaga, N., Umeda, H., & Nomoto, K. 2007, *Astrophys. J.*, 660, 516

Tsunemi, H., Manabe, M., Yamashita, K., & Koyama, K. 1988, *Publ. Astron. Soc. Japan*, 40, 449

Tsunemi, H., Katsuda, S., Norbert, N., & Miller, E. D. 2007, *Astrophys. J.*, 671, 1717

Tsunemi, H., Kimura, M., Uchida, H., Mori, K., & Katsuda, S. 2009, *Publ. Astron. Soc. Japan*, 61, S147

Turner, M. J. L., et al. 2001, *Astron. Astrophys.*, 365, L27

Uchida, H., Tsunemi, H., Katsuda, S. & Kimura, M. 2008, *Astrophys. J.*, 688, 1102

Uchida, H., Tsunemi, H., Katsuda, S. Kimura, M., Kosugi, H., & Takahashi, H. 2009a, *Publ. Astron. Soc. Japan*, 61, 503

Uchida, H., Tsunemi, H., Katsuda, S. Kimura, M., Kosugi, H., & Takahashi, H. 2009b, *Astrophys. J.*, 705, 1152

Uchida, H., Tsunemi, H., Katsuda, S., Kimura, M., & Kosugi, H. 2009c, *Publ. Astron. Soc. Japan*, 61, 301

Uchida, H., Tsunemi, H., Tominaga, N., Katsuda, S., Kimura, M., Kosugi, H. & Takahashi, H. 2009d, *Publ. Astron. Soc. Japan*, in prep

Umeda, H., & Nomoto, K. 2005, *Astrophys. J.*, 619, 427

Uomoto, A., & Kirshner, R. P. 1985, *Astron. Astrophys.*, 149, L7

Uyaniker, B., Reich, W., Yar, A., Kothes, R., & Furst, E. 2002, *Astron. Astrophys.*, 389, L61

Uyaniker, B., Reich, W., Yar, A., & Furst, E. 2004, *Astron. Astrophys.*, 426, 909

Vancura, O., Raymond, J. C., Dwek, E., Blair, W. B., Long, K. S., & Foster, S. 1994, *Astrophys. J.*, 431, 188

Wang, L., Howell, D. Andrew, Höflich, P., & Wheeler, J. C. 2001, *Astrophys. J.*, 550, 1030

Wang, L., Baade, D., Höflich, P., & Wheeler, J. C. 2003, *Astrophys. J.*, 592, 457

Wang, C.-Y. & Chevalier, R. A. 2002, *Astrophys. J.*, 574, 155

Webbink, R. F. 1984, *Astrophys. J.*, 277, 355

Weiler, K. W., & Pangia, N. 1978, *Astron. Astrophys.*, 70, 419

Wheeler, J. C., & Levreault, R. 1985, *Astrophys. J. Letters*, 294, L17

Wilms, J., Allen, A., & McCray, R. 2000, *Astrophys. J.*, 542, 914

Wilson, J. R., & Mayle, R. W. 1993, *Phys. Rep.*, 227, 1

Winkler, P. F., & Petre, R. 2007, *Astrophys. J.*, 670, 635

Woosley, S. E., & Weaver, T. A. 1995, *Astrophys. J. Suppl.*, 101, 181

Woosley, S. E., Heger, A., & Weaver, T. A. 2002, *Rev. Modern Phys.*, 74, 1015

Yamashita, A., et al. 1997, *IEEE Trans. Nucl. Sci.*, 44, 847

Yamazaki, R., Kohri, K., Bamba, A., Yoshida, T., Tsuribe, T., & Takahara, F. 2006, *Monthly Notices Roy. Astron. Soc.*, 371, 1975

Zhang, L., & Fang, J. 2008, *Astrophys. J. Letters*, 675, L21

Zirakashvili, V. N. & Aharonian, F. 2007, *Astron. Astrophys.*, 465, 695